Revealing the Molecular Structure and the Transport Mechanism at the Base of Primary Cilia Using Superresolution STED Microscopy

Tung-Lin Yang

A dissertation submitted in partial fulfillment of
the requirements for the degree of
Doctor of Philosophy
in the Graduate School of Arts and Sciences

COLUMBIA UNIVERSITY

2014

Abstract

Revealing the Molecular Structure and the Transport Mechanism at the Base of Primary Cilia Using Superresolution STED Microscopy

Tung-Lin Yang

The primary cilium is an organelle that serves as a signaling center of the cell and is involved in the hedgehog signaling, cAMP pathway, Wnt pathways, etc. Ciliary function relies on the transportation of molecules between the primary cilium and the cell, which is facilitated by intraflagellar transport (IFT). IFT88, one of the important IFT proteins in complex B, is known to play a role in the formation and maintenance of cilia in various types of organisms. The ciliary transition zone (TZ), which is part of the gating apparatus at the ciliary base, is home to a large number of ciliopathy molecules. Recent studies have identified important regulating elements for TZ gating in cilia. However, the architecture of the TZ region and its arrangement relative to intraflagellar transport (IFT) proteins remain largely unknown, hindering the mechanistic understanding of the regulation processes. One of the major challenges comes from the tiny volume at the ciliary base packed with numerous proteins, with the diameter of the TZ close to the diffraction limit of conventional microscopes.

Using a series of stimulated emission depletion (STED) superresolution images mapped to electron microscopy images, we analyzed the structural organization of the ciliary base. Subdiffraction imaging of TZ components defines novel geometric distributions of RPGRIP1L, MKS1, CEP290, TCTN2 and TMEM67, shedding light on their roles in TZ structure, assembly, and function. We found TCTN2 at the outmost periphery of the TZ close to the ciliary membrane, with a 227±18 nm diameter. TMEM67 was adjacent to TCTN2, with a 205±20 nm diameter. RPGRIP1L was localized toward the

axoneme at the same axial level as TCTN2 and TMEM67, with a 165±8 nm diameter. MKS1 was situated between TMEM67 and RPGRIP1L, with an 186±21 nm diameter. Surprisingly, CEP290 was localized at the proximal side of the TZ close to the distal end of the centrin-labeled basal body. The lateral width was unexpectedly close to the width of the basal body, distant from the potential Y-links region of the TZ. Moreover, IFT88 was intriguingly distributed in two distinct patterns, forming three puncta or a Y shape at the ciliary base found in human retinal pigment epithelial cells (RPE), human fibroblasts (HFF), mouse inner medullary collecting duct (IMCD) cells and mouse embryonic fibroblasts (MEFs).

We hypothesize that the two distribution states of IFT88 correspond to the open and closed gating states of the TZ, where IFT particles aggregate to form three puncta when the gate is closed, and move to form the branches of the Y-shape pattern when the gate is open. Two reservoirs of IFT particles, correlating with phases of ciliary growth, were localized relative to the internal structure of the TZ. These subdiffraction images reveal unprecedented architectural details of the TZ, providing a basic structural framework for future functional studies. To visualize the dynamic movement of IFT particles within primary cilia, we further conducted superresolution live-cell imaging of IFT88 fused to EYFP in IMCD cells. Our findings, in particular, show IFT88 particles pass through the TZ at a reduced speed by approximately 50%, implying the gating mechanism is involved at this region to slow down IFT trafficking. Finally, we report the distinct transport pathways of IFT88 and Smo (Smoothened), an essential player to hedgehog signaling, to support our hypothesis that two proteins are transported in different mechanisms at the ciliary base, based on dual-color superresolution imaging.

Table of Contents

List of Figures

List of Tables

Acknowledgement

I would like to express my gratitude to all people who helped me in the completion of my dissertation. My especially deepest gratitude first goes to my research advisor, Dr. Jung-Chi Liao, for all his guidance and support throughout my PhD studies. I joined his group four years ago with limited knowledge of biophysics and optics, but the ideal research environment in his group allows me to gradually develop the knowledge and skills needed to tackle challenging questions in biophysical research.

I would like to also thank my dissertation committee, Dr. James Hone, Dr. Christopher Jacobs, Dr. Qiao Lin, and Dr. Meng-Fu Bryan Tsou, for their comments and suggestions and for providing a lot of invaluable insights into my research works. This dissertation has been improved because of their feedback. I would like to also thank Dr. Rudolf Leibel for introducing me to the field of primary cilia research.

The members of my research group have provided a great deal of help during my doctoral studies. I would like to particularly thank the collaboration and friendship I have had with Bhavik Nathwani and Yuan Zhang. Without their help in optical and biological experiments for STED imaging, many research works in this thesis would have been much more difficult. I also like to thank Perry Hampilos and Christine Miller for their excellent assistance with all kinds of biological experiments and instructions. Edward Bossange and Nupur Sutaria had also helped me a lot with the programming for STED microscopy. I would like to thank Dr. Won-Jing Wang and Dr. Chii-shyang Fong for the collaboration in my research studies and for many science and non-science discussions. I would like to also thank Hans Lu, Jimmy Su, Eileen Jiang, Arthi Suresh, Jay Shim, Jamie Solimano, and

Estee Hong for their great efforts on my research progress, and I have been very fortunate to work with them. The research projects presented in this dissertation were supported by a National Science Foundation Grant, startup funds for the lab provided by Columbia University, and a Taiwanese Ministry of Education Scholarship.

Finally, and most importantly, I am deeply grateful to my Parents, my Family, and Chien-Peng Wu who made my studies possible and for their endless support and encouragement throughout my doctoral studies.

List of Abbreviations

ACIII	Adenylyl Cyclases Type Iii
Actub	Acetylated Tubulin
BB	Basal Body
BBS	Bardet-Biedl Syndrome
CW STED	Continuous-Wave Stimulated Emission Depletion
dSTORM	Direct Stochastic Optical Reconstruction Microscopy
EGFP	Enhanced Green Fluorescent Protein
EM	Electron Microscopy
EYFP	Enhanced Yellow Fluorescent Protein
FBS	Fetal Bovine Serum
FPALM	Fluorescence Photoactivation Localization Microscopy
FWHM	Full-Width Half-Maximum
HFF	Human Foreskin Fibroblast
Hh	Hedgehog
IFT	Intraflagellar Transport
IMCD	Inner Medullary Collecting Duct
JBTS	Joubert Syndrome
MEF	Mouse Embryonic Fibroblast
MKS	Meckel-Gruber Syndrome
NPHP	Nephronophthisis
PAINT	Points-Accumulation-For-Imaging-In- Nanoscale-Topography
PALM	Photoactivation Localization Microscopy
PBS	Phosphate Buffered Saline
PBST	Phosphate Buffered Saline + Triton-X 100
PFA	Paraformaldehyde
PSF	Point Spread Function
Ptc	Patched
RPE	Retinal Pigment Epithelium
SAG	Smoothened Agonist
Shh	Sonic Hedgehog
SLS	Senior-Løken Syndrome

Smo	Smoothened
SPDM	Spectral Precision Distance Microscopy
SSIM	Saturated Structured Illumination Microscopy
STED	Stimulated Emission Depletion
STORM	Stochastic Optical Reconstruction Microscopy
TCTN	Tectonic
TF	Transitional Fiber
TZ	Transition Zone
YFP	Yellow Fluorescent Protein

1 Background and Motivation

1.1 Primary cilia

The primary cilium, a typically solitary microtubule-assembled organelle that projects from the cell membrane, serves as an antenna that senses extracellular signals and conducts intraflagellar transport in nearly all mammalian cell types [1-8]. The axoneme, or the microtubule-based backbone of the primary cilium, consists of a ring of nine microtubule doublets that originates from the mother centriole-converted basal body (BB) (Figure 1-1)[9-15]. The diameter of the ciliary membrane is approximately 250–300 nm and the axonemal diameter of the microtubule doublets is approximately 150–180 nm based on electron microscopy (EM) images. A contiguous structure connecting the basal body to the axoneme is known as the transition zone, where the transitional fibers (TFs), 120-150 nm in length, project from the basal body to the membrane, and Y-links, 50-60 nm long, are seen via electron microscopy (EM) as emanating from the peripheral doublets and attaching to the ciliary membrane[16] (Figure 1-1). The TZ potentially anchors the axoneme to the ciliary membrane and serves as a diffusion barrier to screen molecules entry and exit from the cilium and thus creates the ciliary compartment with its unique composition[16-20].

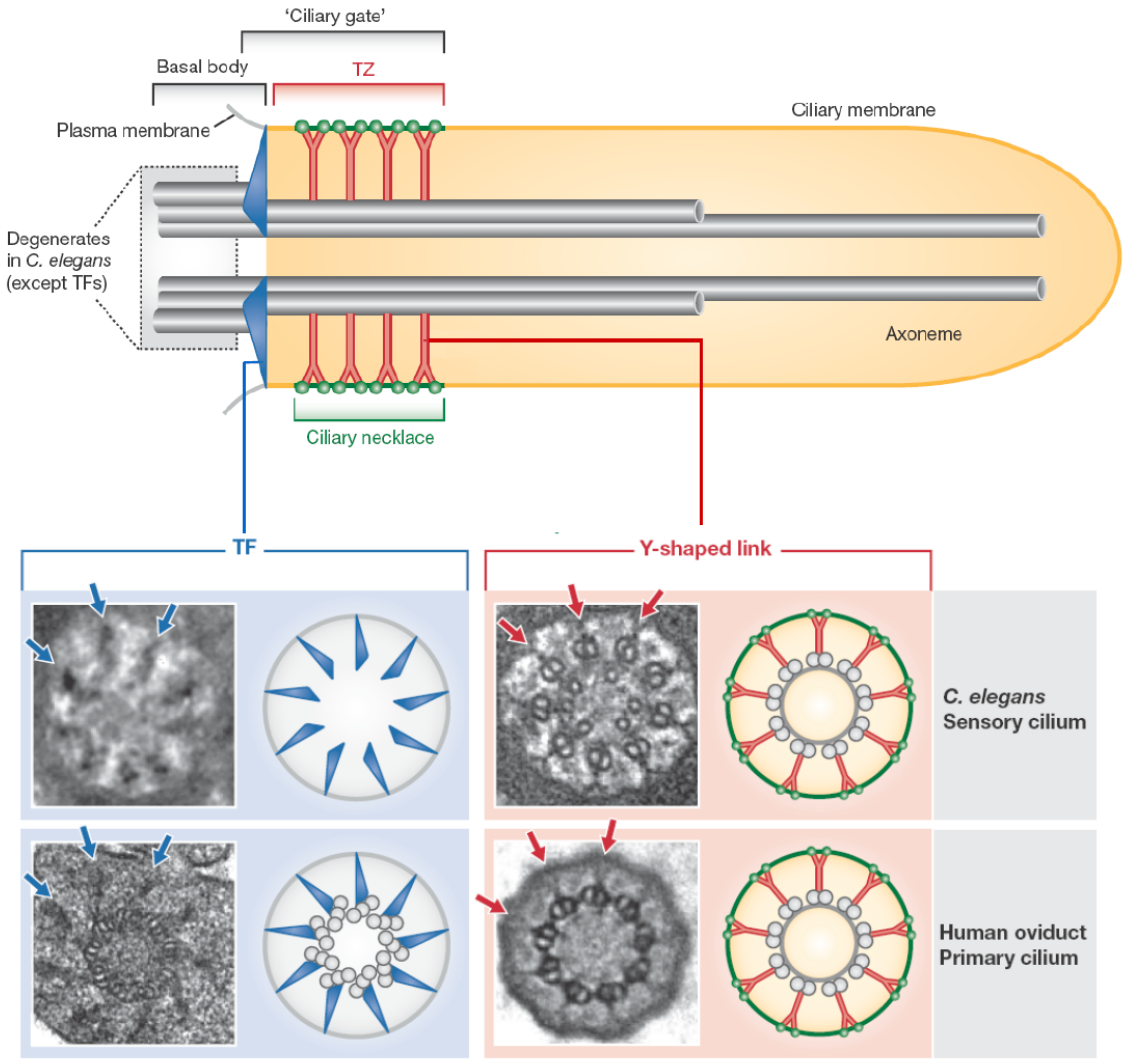

Figure 1-1 Structure of primary cilia[15]. All cilia have a microtubule-based axoneme that extended from a centriolar structure termed the basal body. The TFs (transitional fibers) and TZ (transition zone) are shown schematically together with representative EM images from a C. elegans sensory cilium and human primary cilium. Y-link structures and the ciliary necklace are shown on the ciliary surface.

1.1.1 Ciliopathy and transition zone

Although the TZ is composed of more than 20 species of proteins, the structural arrangement of the TZ proteins remains largely unknown [17,21-22]. A recent review has

summarized the possible functions of those TZ proteins, and some of them are listed in Table 1-1[15]. Aberrations of TZ proteins are associated with a series of ciliopathies, including Nephronophthisis (NPHP), Joubert syndrome (JBTS), and Meckel-Gruber syndrome (MKS), Bardet-Biedl syndrome (BBS), and Senior-Løken syndrome (SLS), with various brain, kidney, and limb defects [23-25]. The relationship of human ciliopathies and the associated TZ proteins are depicted in Figure 1-2 [26]. For example, mutations of TZ proteins, CEP290, RPGRIP1L, or TMEM67, result in at least three of these ciliopathies, whereas TCTN2 and TMEM216 are involved in JBTS and MKS [17-18,21,27]. A recent review proposed a model of TZ protein localization based on available biochemical and immuno-EM studies [16], where CEP290 and RPGRIP1L were speculated to be localized to the coiled coils of the Y-link while TMEM proteins and TCTN proteins were speculated to be at the transmembrane[22]. Structural understanding of these TZ proteins would facilitate the mechanistic study of TZ functions in molecular screening and anchoring. Ciliogenesis upon the TZ is facilitated by an intraflagellar transport (IFT) system with molecular motors and IFT proteins that deliver axoneme elements [28-29]. These proteins have to pass through the TZ to reach the ciliary compartment. Transition fibers (TFs) at the distal end of the BB have been found to recruit IFT proteins to the ciliary base [30].

Table 1-1 Functions and associated disorders of TZ proteins[15]

TZ proteins	Functions
MKS1	Formation and function of ciliary gate; Hedgehog signaling
B9D1	Formation and function of ciliary gate; Hedgehog signaling
B9D2	Formation and function of ciliary gate
TMEM216	Formation and function of ciliary gate
TMEM67	Formation and function of ciliary gate

TMEM231	Function of ciliary gate; Hedgehog signaling
TMEM237	Formation and function of ciliary gate; regulation of Wnt signaling
RPGRIP1L	Formation and function of ciliary gate; scaffold for many transition zone proteins; Hedgehog signaling
CC2D2A	Formation and function of ciliary gate; Hedgehog signaling
CEP290	Formation and function of ciliary gate; possible component of Y-links
TCTN1	Function of ciliary gate; regulates Hedgehog signaling
TCTN2	Neural tube patterning, Hedgehog signaling
TCTN3	Forms complex with TCTN1,TCTN2, MKS1, B9D1, CC2D2A, and TMEM67
NPHP1	Formation and function of ciliary gate
NPHP4	Formation and function of ciliary gate

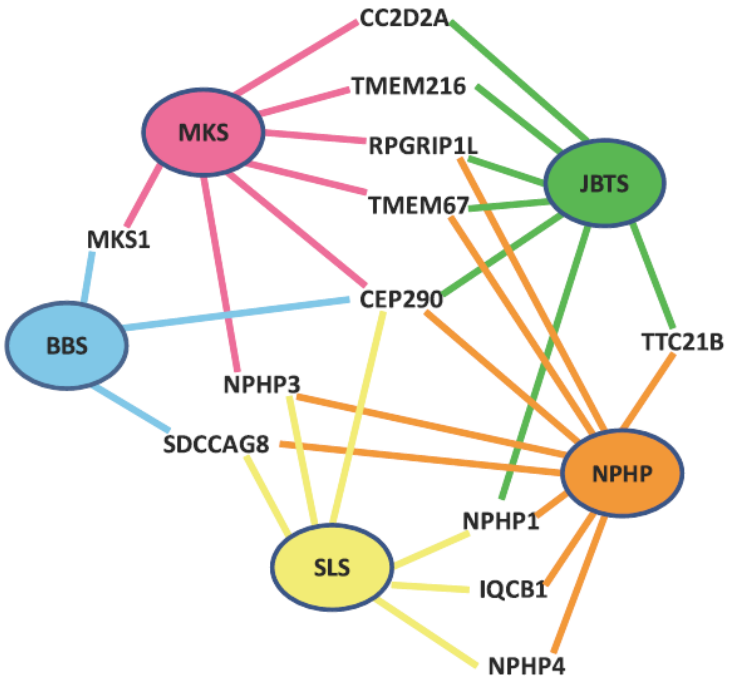

Figure 1-2 Five ciliopathies with extensive genetic heterogeneity and pleiotropy (BBS, Bardet-Biedl syndrome; JBTS, Joubert syndrome; MKS, Meckel-Gruber syndrome; NPHP, nephronophthisis; SLS, Senior-Løken syndrome) [26].

1.1.2 Intraflagellar transport

The assembly and maintenance of the ciliary structure, as well as the movement of receptors and channels responsible for various signaling pathways, rely on specialized transport machinery, termed intraflagellar transport (IFT). IFT, which was first observed in the flagella of the green alga *Chlamydomonas reinhardtii* [28,31], is a bidirectional transport system that moves membrane- and/or non-membrane-bound ciliary proteins (IFT particles) from the cytoplasm out to the ciliary tip and then back to cell body along the axoneme [12,29,32]. IFT particles are found to be comprised of two distinct complexes, complex A and complex B as listed in Table 1-2 [12,33]. Numerous studies have indicated that complex B is required for anterograde transport of axonemal precursors, most notably by demonstrating the inhibition of cilia assembly after the loss of complex B [32,34-36]. IFT88/polaris, one of the most important IFT proteins in complex B, is known to play a role in the formation and maintenance of cilia in various types of organisms [37]. For example, a mutation in IFT88 is associated with polycystic kidney disease due to its disruption of the ciliogenic pathway that is required for assembly of the renal cilium [37-39]. In addition, it was found that mice with aberrant IFT88 exhibited retinal degeneration and abnormalities in the development of the photoreceptor outer segment [40]. IFT88, also known to be a centrosomal protein, is closely associated with the cell cycle in mammalian cells, in which IFT88 regulates the G1-S transition and promotes cell-cycle progression when depleted by RNA interference [41]. Although a great number of studies have shown the importance of IFT88, its specific role in the transport system and how it localizes at the cilia remain elusive. Specifically, the entrance of IFT proteins into the ciliary compartment remains largely unclear.

Table 1-2 Components of the intraflagellar transport system[12]

IFT system component	General protein name	Chlamydomonas reinhardtii	Caenorhabditis elegans	Other
IFT complex A	IFT144	IFT144	DYF-2	
	IFT140	IFT140	CHE-11	
	IFT139	IFT139	ZK328.7	
	IFT122, IFT122A	IFT122, FAP80	DAF-10	
	IFT121, IFT122B	IFT121	IFTA-1	
	IFT43	IFT43	-	
IFT complex B	IFT172	IFT172	OSM-1	
	IFT88	IFT88	OSM-5	Tg737, Polaris
	IFT81	IFT81	IFT-81	
	IFT80	IFT80	CHE-2	
	IFT74, IFT72	IFT74, IFT72	IFT-74	
	IFT70	IFT70, FAP259	DYF-1	Fleer
	IFT57	IFT57	CHE-13	Hippi
	IFT54	IFT54, FAP116	DYF-11	Elipsa
	IFT52	IFT52, BLD1	OSM-6	
	IFT46	IFT46	DYF-6	
	IFT27	IFT27	-	
	IFT25	IFT25, FAP232	-	
	IFT22	IFT22, FAP9	IFTA-2	
	IFT20	IFT20	Y110A7A.20	

1.1.3 Cilia-dependent signaling

Based on studies of structure recognition and developmental genetic analyses, primary cilia have been known to be a signaling center of sonic hedgehog (Shh) pathway, the cAMP pathway, Wnt pathway, planar cell polarity pathway, intracellular Ca2+ signaling and organogenesis [42-48]. For example, primary cilia regulate the mammalian hedgehog signal-transduction machinery. As illustrated in Figure 1-3, the involved action of Hh signaling is the conversion of Gli proteins from being repressors to activators.

Smoothened (Smo) and the Hh receptor Patched (Ptc) proteins are the essential players in this signaling conversion. When Hh signals are absent, Ptc inhibits Smo activation. Gli transcription factors are then maintained in their repressor state (Figure 1-3A). Upon the binding of Hh to primary cilia, Ptc proteins are no longer to suppress Smo, thus triggering generation of Gli transcriptional activators (Figure 1-3B)[10]. Interestingly, a previous study had shown that the disruption of IFT led to a loss-of-function Shh phenotype in the neural tube, and a gain-of-function Shh phenotype in the limb [3,43]. Further studies have reported that IFT is required for the downstream of Ptch1 and Smo proteins. Also, IFT proteins are essential to enable Gli activation and the proteolytic processing of Gli3 into Gli3R [3,47-50]. Smo plays an important role in the Shh signaling pathway, and are therefore likely affected by IFT mutants. The earlier reports revealed that Smo accumulates in the cytoplasm as well as on the primary cilia. However, it is unclear whether IFT function is directly required in Shh signaling to translocate Smo to the ciliary membrane [50-51].

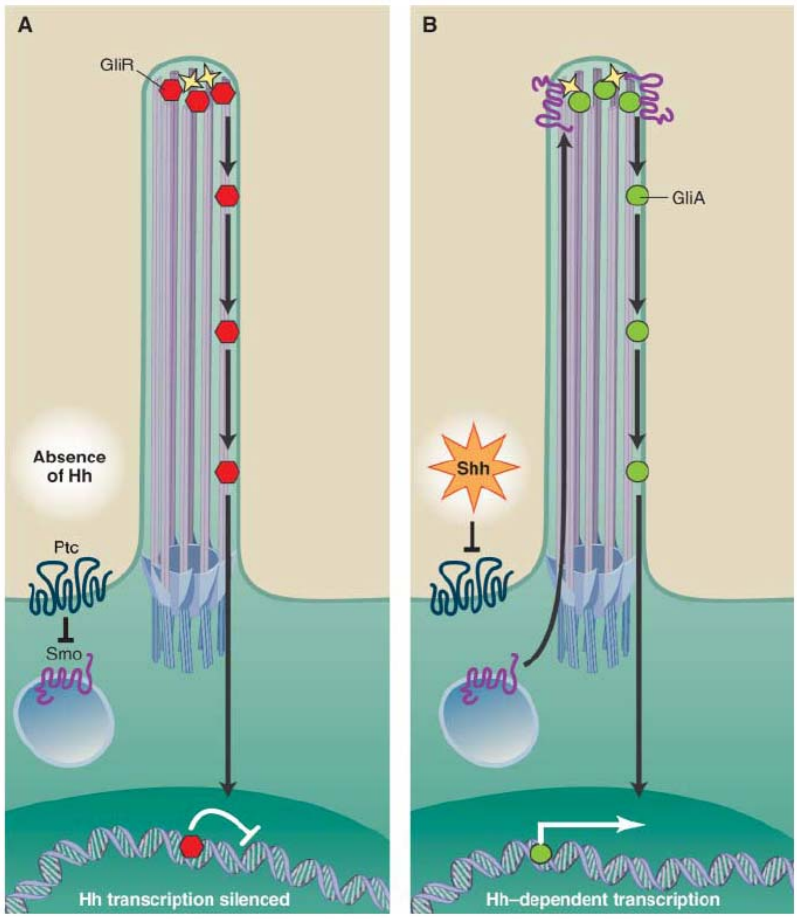

Figure 1-3 A model of Hh signal transduction[10]. (A) In the absence of Hh, Ptc represses the function of Smo and Gli proteins are maintained in their transcriptional repressor state. (B) Upon the binding of Hh to primary a cilium, Smo inhibitor is released and Smo translocates to the cilium. Gli activators then move to the nucleus to activate Hh-dependent transcription.

The cAMP pathway, known as the adenylyl cyclase pathway, is a G protein-coupled receptor-triggered signaling cascade used in cell communication [52]. Adenylyl cyclases type III (ACIII), a membrane-bound protein, has been shown to localize to primary cilia in a variety of cell types. For example, studies have demonstrated that ACIII is expressed in the primary cilia of hippocampus neurons and cerebral cortex of adult mouse brain and can be used as a marker of cilia [53-54]. ACIII is one of several isoforms of adenylyl cyclase that is

involved in the cAMP signaling pathway and it catalyzes the conversion of ATP to cAMP to activate a variety of downstream physiological processes and signal transductions [55]. Early studies revealed that ACIII resides in the sensory neuronal cilia, where a significant difference in the enzymatic activities of ACIII proteins may modulate the G protein-cAMP signaling cascade that mediates the olfactory system [56-57]. Further studies in mice showed that ACIII and the cAMP signaling cascade in primary cilia are required for memory of novel object recognition, contextual fear extinction, and temporally dissociative passive avoidance (TDPA) [58]. Recent studies have found that ACIII is also important for the regulation of primary cilia length [59]. For example, elongation of primary cilia in the mouse brain, cultured cells (such as FLS, HFF, NIH3T3), and human astrocytes was observed when exposed to the lithium treatment, which inhibits ACIII activity and consequently lowers the cAMP level. The role of ACIII was confirmed to be a mediator for the effect of lithium, excluding other potential mediators such as GSK-3β and inositol-PKC [59-61]. Despite its importance in the cAMP pathway and ciliogenesis, the details of ACIII localization and its interactions with other proteins in primary cilia remain unclear.

1.2 Need for superresolution microscopy

Characterization of the detailed spatial distribution of molecules has been hindered by the resolution limit of conventional far-field optical microscopy, which cannot identify adjacent features smaller than 200-250 nm, governed by Abbe's law [62]. Investigating the molecular architecture of the ciliary base, specifically for the TZ, as well as the variations of distributions of IFT proteins and the involved signaling proteins like Smo close to the

TZ, is essential in establishing a structural foundation for revealing the regulating mechanism at the base of primary cilia, providing a reference frame for further mechanism studies of various ciliopathies. The major challenge of observing these molecules, however, lies in the tiny volume of the region close to the TZ, spanning only 250 nm in diameter and 300-1000 nm in length, packed with a large number of protein species. Conventional microscopes, limited by the diffraction limit, are thus unable to resolve the localization of those ciliary proteins in this region. Electron microscopy (EM) can afford a much better resolution, but it cannot be used for live cell imaging and it is relatively challenging to correlate observations with functional perturbations. Although immunogold EM technique is capable of labeling a specific target with eminent resolution, its sample preparation is still challenging and the results usually provide only a small fraction of molecules [16,63]. To gain enough resolution, one can look into probing method utilizing near-field optics. Near-field scanning optical microscopy (NSOM/SNOM) avoids light diffraction in the far field and therefore offers sub-100 nm resolutions [64]. However, its requirement to conduct imaging as close to contact as atomic force microscopy (AFM) largely limits its application for biological studies.

Emerging advances in superresolution imaging based on far-field approaches have revolutionized biological studies and many other disciplines, opening opportunities to observe samples previously impossible by means of a conventional microscope [65-80]. Most of these superresolution imaging methods achieve subdiffraction resolution by employing the photophysics of fluorescent makers. They are classified into two major groups of superresolution imaging methods: (1) Deterministic superresolution including STED[68-69], GSD[74], RESOLFT[75] and SSIM[67]. The first three approaches exploit the nonlinear

behavior of fluorophores by excitation and de-excitation; (2) Stochastical superresolution based on single-molecule localization methods such as PALM[71], FPALM[76], STORM[66,70], dSTORM[77], SPDM[65,78], SPDMphymod[79], and PAINT[80].

The major advantages and challenges among the three types of superresolution approaches i.e. STED, PALM/STORM, and SSIM are listed in Table 1-3. In terms of the lateral resolution, STED is next only to the single molecule-based approach, reaching 50-nm resolution. In terms of the acquisition speed and sample preparation, STED (stimulated emission depletion) microscopy is one of the most promising superresolution techniques because of its capability in live-cell recording [81-82]. Based on a reversibly photoswitchable mechanism, STED microscopy, a confocal-based setup, narrows down the point spread function (PSF) through transiently switching off fluorophores at the outer rim of a focal spot by employing a doughnut-shaped, red-shifted depletion laser. With this deterministic imaging method, STED microscopy does not need to sacrifice acquisition speed by separating its fluorescent emission in time intervals. With the primary advantage of sufficient spatial and superior temporal resolution, STED has been demonstrated to achieve video-rate imaging studies of neurons [83] and up to 200-fps observation of colloidal-crystal nanostructures [84].

Table 1-3 The comparison among different superresolution techniques[85].

	Epifluorescent/ Cconfocl	STED	PALM/STORM	SIM
Major advantages		Good resolution High speed (small area) Live cell imaging	Very good resolution 3D Multicolor High sensitivity	Image quality 3D Live cell imaging Multicolor Fluorophore flexibility

Current challenges		Three or more colors Axial resolution Number of frames	Speed Sample optimization Number of frames	Resolution Number of frames
Resolution xy (nm)	250/250	50/70	20/50	120/120
Resolution z (nm)	500/500	500/500	50/70	300/300
Sampling speed for a small area (2μm × 2μm)	0.01s	0.03s	1min	1s
Sampling speed for a large area (20μm × 20μm)	0.01s	3s	1min	1s

1.3 Overview

This dissertation is organized as follows. Chapter 2 describes the principle of STED microscopy and then details the implementation of the single-color continuous wave (CW) STED microscopy setup. The dual-color common-depletion STED is then illustrated to be implemented by expanding the single-color setup, enabling the spectrum-separable excitation of a fluorophore pair. The last part of this chapter shows resolution validation of this dual-color superresolution system for both physical and biological samples. In chapter 3, we report the distinct localization of two important ciliary proteins, IFT88 and ACIII using the CW STED microscope. The quantitative analyses of molecular distribution along the cilia or at the base of the cilia to characterize these proteins are presented. Chapter 4 focuses on the study of molecular architecture at the ciliary base using the dual-color superresolution method. We first optimize imaging techniques and sample preparations, as well as optical alignment, acquisition rate, laser power, staining protocol, and cell culture for this study. The next section creates a molecular map of important proteins in the TZ, the TFs, and the BB by overlapping multiple dual-color

superresolution images to generate the molecular architecture at the ciliary base. Chapter 5 extensively explores the IFT mechanism at the ciliary base. Along with mapping the TZ, we conduct a superresolution analysis of the distributions of IFT proteins through the region and examine the mechanisms of IFT transport. Further investigation of this mechanism is directly presented by the superresolution live-cell imaging of the dynamics of IFT protein. The last part describes the observation of the localization of Smo protein near the TZ and the differentiatiation between transport mechanism of IFT protein and signaling protein. Chapter 6 summarizes the major findings of all the studies described in this dissertation.

2 Development of a Dual-Color STED Microscopy System

2.1 Principles of STED microscopy

The idea of superresolution STED microscopy was first proposed in 1994 by Stefan Hell and Jan Wichmann[68] and implemented by Thomas Klar and Stefan Hell[86]. Conceptually, STED microscopy achieves superresolution by transiently switching off fluorophores located at the outer rim of a focal spot of excitation light by de-excitation through stimulated emission[87]. A STED microscope basically contains an excitation laser beam as a conventional confocal microscope to pump fluorophores from the electronic ground state S0 to the first excited state S1. In addition, a second laser beam in red-shifted doughnut-shaped profile, usually called STED beam or depletion beam is incorporated with the first beam to tailor the effective excitation volume.

2.1.1 Stimulated Emission and fluorophores

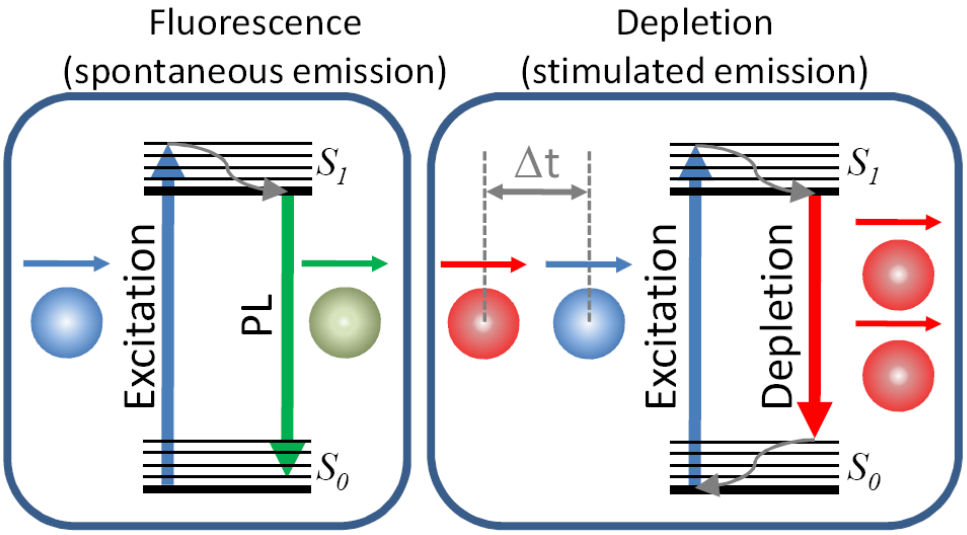

Figure 2-1 Jablonski diagram showing the molecular states and transitions in STED[88]. (left) The fluorophore is excited from the electronic ground state S0 to a higher first excited electronic state S1 through absorption of the excitation light. Then, the

fluorophore emits spontaneously a fluorescence photon and is transferred back to S0 state. (right) Stimulated emission occurs when a photon of a different wavelength from that of fluorescence emission is involved to stimulate the excited molecule to emit two identical two photons with non-fluorescence pathway.

Figure 2-1 the Jablonski diagram[89] demonstrates the energy levels and transitions involved in STED microscopy. For fluorescence emission, the fluorophore is pumped from the ground state S0 to the first excited state S1. After relaxation to the lowest vibrational state of S1, this molecule spontaneously emits a photon in the transition of fluorescence, or photo-luminescence (PL) (Figure 2-1, left). However, this molecule can be enforced to give off stimulated emission immediately instead of spontaneous transition by introducing a photon with a wavelength different from that of fluorescence emission. This mechanism in which a forced emission occurs to weaken the spontaneously fluorescence emission is called depletion (Figure 2-1, right). Therefore, a fluorophore can selectively return to the lowest vibrational level of S0 via either spontaneous or stimulated emission.

For the desired stimulation-emission-depletion, a wavelength at the tail of the emission spectrum is usually preferably chosen in STED microscopy for the following reasons. First, the excitation cross section must be small enough at the depletion wavelength; otherwise the STED beam would excite the fluorophore as well as cause stimulated emission transition. For most fluorophores, the excitation spectrum overlaps with the emission spectrum; therefore, the excitation can be prevented only when we choose a wavelength towards the red end of the spectra. Second, this red-shifted stimulated emission wavelength from S1 to S0 transition allows us to spectrally separate

spontaneous and stimulated emission[90].

2.1.2 STED microscopy

STED works using two laser beams which arrive at the focal plane of samples with a shrunk detective spot. The first one (excitation beam) excites and the second one (depletion or STED beam) de-excites the fluorescent markers. To achieve this, a diffraction-limited spot of excitation beam is typically overlapped with a doughnut-shaped red-shifted pattern of a STED beam to transiently switch off fluorophores in the outer rim of diffraction-limited fluorescence spot via stimulated emission, schematically shown in Figure 2-2. Thus, only the fluorophores near the center zero of STED beam are excited, decreasing the effective point spread function (PSF) and achieving the undiffracted resolution.

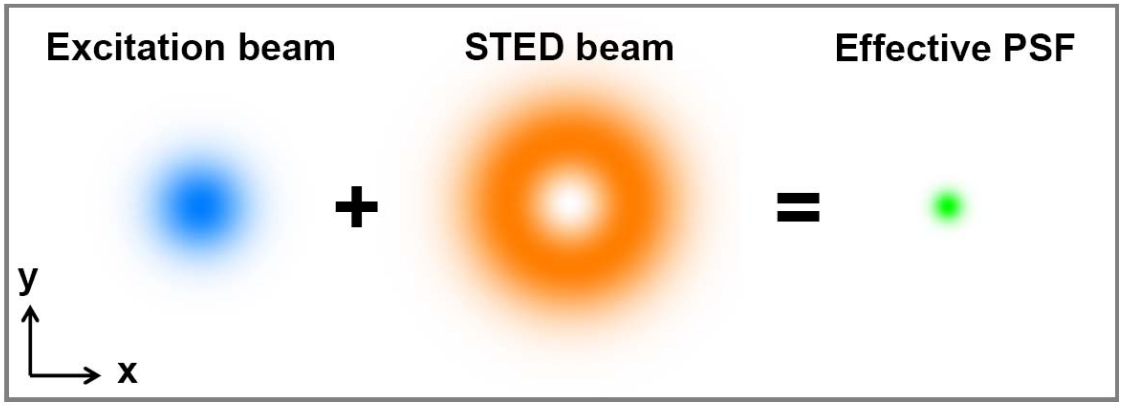

Figure 2-2 Principle of a typical STED optical configuration. The excitation spot (blue) is superimposed with the STED depletion laser profile (orange) at x-y focal plane to narrow down the size of the effective point-spread function (PSF) as the green spot of a STED microscope. The simulated emission transiently switches off fluorescence transition at the outer part of excited spot, thereby leaving the only very central region fluorescing. The stimulated emission is spectrally separated from the fluorescence.

Using a high intensity STED beam, the fluorophores residing in the excited S1 state is mostly depleted in those areas close to the intensity peak of a doughnut. Only in the very center, where the STED light has zero intensity, the fluorophores unaffectedly emit in the fluorescence pathway [90-91]. The key concept involved in the STED imaging is the non-linear dependence between the depletion emission of excited electrons and STED beam intensity. When the STED beam intensity is higher than a certain threshold or saturation intensity, all the spontaneous emission is suppressed by the stimulated emission. Thus, there are two factors determining the resolution of STED microscopy: they are STED laser intensity and saturation intensity of fluorophores. The second one is a function of the STED laser wavelength and intrinsic characteristics of the fluorophore such as lifetime and kinetics of the population of ground and excited states [88]. Figure 2-3 typically shows the depletion of the fluorescence as a function of the STED beam power for crimson fluorescent beads [73]. The fluorescence level follows a form of $(1+\gamma P)^{-1}$, where γ is the fluorophore-characteristic constant.

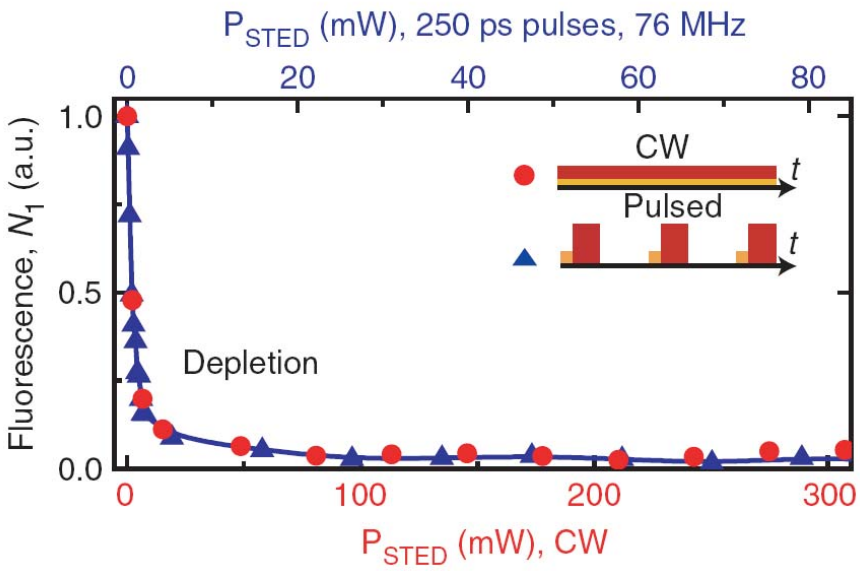

Figure 2-3 Fluorescence level is measured as a function of STED laser power[73].

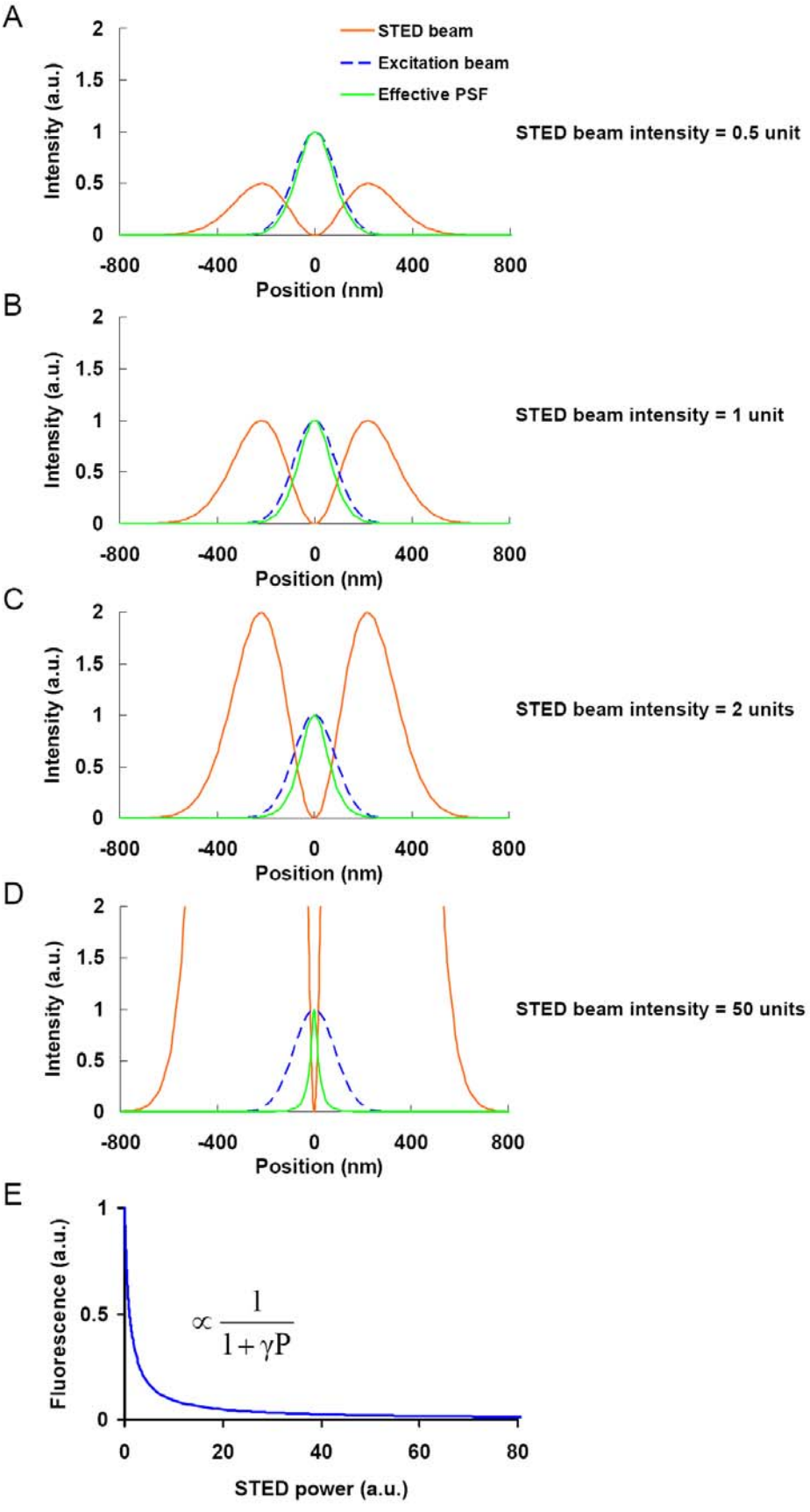
A
STED beam
Excitation beam
Effective PSF
STED beam intensity = 0.5 unit
Intensity (a.u.)
Position (nm)
B
STED beam intensity = 1 unit
C
STED beam intensity = 2 units
D
STED beam intensity = 50 units
E
Fluorescence (a.u.)
$\propto \frac{1}{1+\gamma P}$
STED power (a.u.)

Figure 2-4 Illustration of overlapping the excitation and depletion beam to yield a shrunk fluorescing spot. (A to D) Different intensities of STED doughnut-shaped beam are superimposed with a Gaussian beam at one-unit intensity. From A to C, the effective PSFs are gradually narrowed with the STED intensity. (D) The PSF is significantly smaller using high STED intensity up to 50 units. Most areas of the STED beam reach saturation intensity to turn off fluorescence (E) Fluorescence curve as function of STED power.

As previously discussed, STED imaging is a non-linear process of the fluorescence depletion and STED beam power, hence allowing fluorophores to switch their states between "on" and "off" via stimulated emission depletion. In terms of the manipulated beam size, both excitation and STED beam still present diffracted patterns, generally beyond 200 nm, regardless of laser power. Therefore, achieving an undiffracted PSF is not only based on a geometrically unchanged size of the doughnut-shaped depletion beam, but also an adjustable fluorescing area. Figure 2-4 demonstrates this mechanism how two spatially overlapped laser beams accomplish a smaller effective PSF. We generated a wave that is a superposition of two Hermite-Gaussian beams of orders (1, 0) and (0, 1) [92] to simulate the STED beam as shown in Figure 2-2. The excitation beam profile is created with a Hermite-Gaussian beam of order (0, 0). The profiles of these beams through the central peak or zero are displayed in Figure 2-4A to D. In order to illustrate the interaction of the excitation and the STED beam profile, we used the fluorescence depletion curve generated in the form of $(1+\gamma P)^{-1}$, where γ was set to one (Figure 2-4E).

Figure 2-4A to D report the results of the effective PSF under the 0.5, 1, 2, and 50 units of STED intensity, respectively. In Figure 2-4A, the effective PSF is nearly unchanged at a half-unit STED intensity, all below one unit that depletes fluorescence by

50%. When STED intensity is increased to one unit, only the fluorescence at the peak intensity of STED beam, or the outer rim of excitation beam, is depleted up to half (Figure 2-4B). When STED intensity doubles, the area with intensity higher than one unit moves inwardly to cause more stimulation emission depletion, hence the effective PSF is slightly narrowed (Figure 2-4C). To fulfill a substantial effect of STED microscopy, an intense STED beam is typically used to make the most regions at the outer part of excitation non-fluorescent (Figure 2-4D). Although the size of the depletion beam is unchanged, the depletion intensity above the threshold is moving to the center. Therefore, the effective PSF is strongly narrowed because all fluorophores in the periphery are kept in dark. Note that the depletion intensity is usually much higher than the excitation intensity. The size of an effective PSF, or optical resolution, of STED microscopy was mathematically described in the extended form of Abbe's law [62], which follows the relationship [93]

$$d \sim \frac{\lambda}{2n\sin\alpha\sqrt{1+\frac{I}{I_s}}} \tag{2-1}$$

Where d is the full-width-at-half-maxima (FWHM) of fluorescing area, λ is the wavelength of the excitation beam and $n\sin\alpha$ denotes the numerical aperture of the objective lens with n as the refractive index and α as half the focal angle. I_s is the saturation intensity of fluorescent dyes and I is the intensity of STED beam. Therefore, increasing the STED intensity decreases the effective PSF, meaning that as the ratio I/I_s goes to infinity, the resolution becomes diffraction "unlimited".

2.2 Implementation of a single-color STED microscopy system

2.2.1 Layout of the CW microscopy system

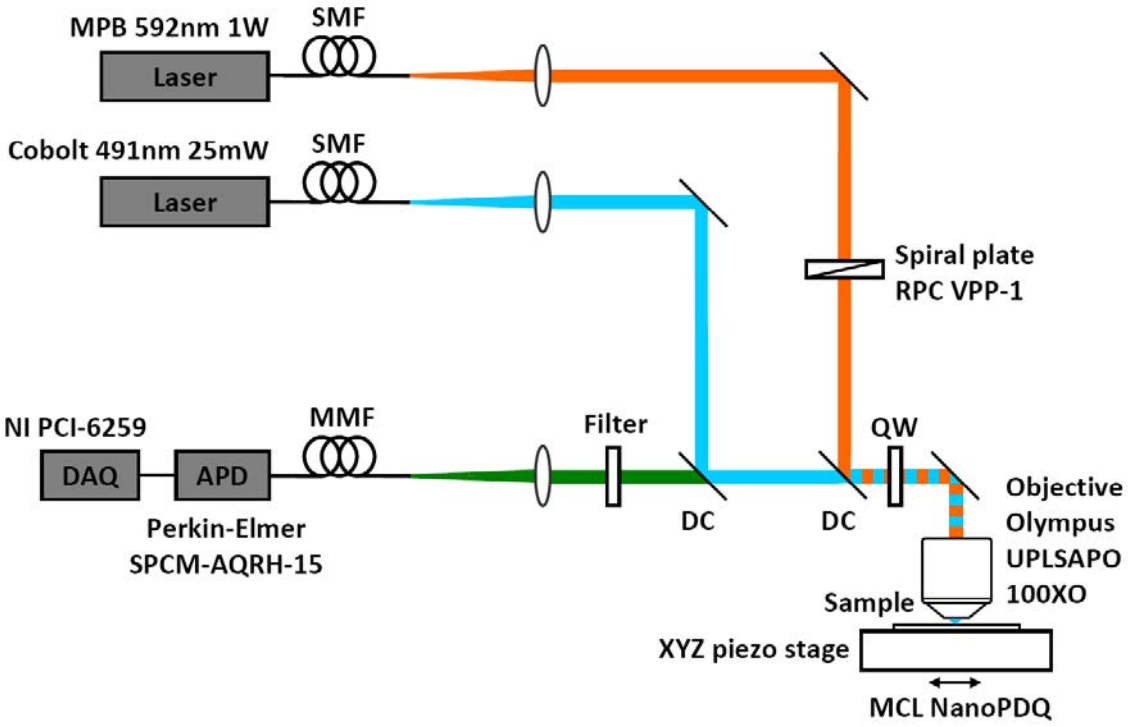

Figure 2-5 Schematic of our single-color CW STED setup in which a 491-nm laser and a 592-nm laser were spatially aligned and overlapped to achieve superresolution imaging. The 592-nm depletion laser line is transformed into a toroid-shaped beam via a spiral phase mask. Two laser beams focused by a 100X oil-immersion objective present on the sample position detects fluorescence following a scanning protocol. The signals are filtered before reaching the APD single-photon detector.

We developed a CW STED microscopy system on the basis of a previously reported setup by Hell's laboratory [73]. In our setup of CW STED, schematically shown in Figure 2-5, the excitation beam at 491-nm wavelength is delivered by a diode-pumped solid state (DPSS) laser (Calypso 25, Cobolt AB) and for the depletion beam by a 592-nm 1W CW fiber laser line (VFL-P-1000-592, MPB Communications Inc) was used. Two laser lights

were carried through single-mode polarization-maintaining fibers (SM/PMF) (P3-488PM-FC-2, Thorlabs) individually, then merged at a dichroic mirror (DC) and focused onto the sample plane by an oil immersion objective (Olympus UPLSAPO100x-1.4 NA). The fluorescence was collected through the same lens and separated from laser lights by dichroic mirrors (FF541-SDi01-25x36 and Di01-R488-25x36, Semrock). The signals then were cleaned via a 535/22 band-pass filter (FF01-535/22-25, Semrock) and coupled into a multimode optical fiber (M31L05, Thorlabs) with an opening diameter at 80% of the back-projected Airy disk to confocalize the image. A photomultiplier tube (PMT, MP963, PerkinElmer Optoelectronics) or an avalanche photodiode (APD) single photon counting module (SPCM-AQR-15, PerkinElmer Optoelectronics) was used to detect the photons from fluorescent samples, which was held on a three-axis piezostage scanner (Nano-PDQ375HS, Mad City Labs Inc). A vortex phase plate (VPP-1, RPC Photonics Inc) introducing helical phase ramp of $\exp(i\varphi)$ with $0 < \varphi < 2\pi$ was employed to create a central-zero doughnut depletion beam in overlapping with the excitation beam to achieve stimulated emission-depletion of fluorophores in the region covered by the depletion beam.

The laser line at 491-nm wavelength was designed to excite a series of fluorescent markers such as Oregon Green 488, Alexa Flour 488, green fluorescent protein (GFP), or yellow fluorescent protein (YFP). Most of them are illuminated around the peaks of excitation spectra (Figure 2-6A) except for the YFP which is still more than 40 % high. Their emission spectra are illustrated in Figure 2-6B where a detection window between 524nm-546nm (or 520nm-550nm) was chosen to collect fluorescence from those markers. The 592-nm laser line was used to deplete them at the red-shifted tail of the emission

spectra to avoid the significant background caused by the excitation of this laser.

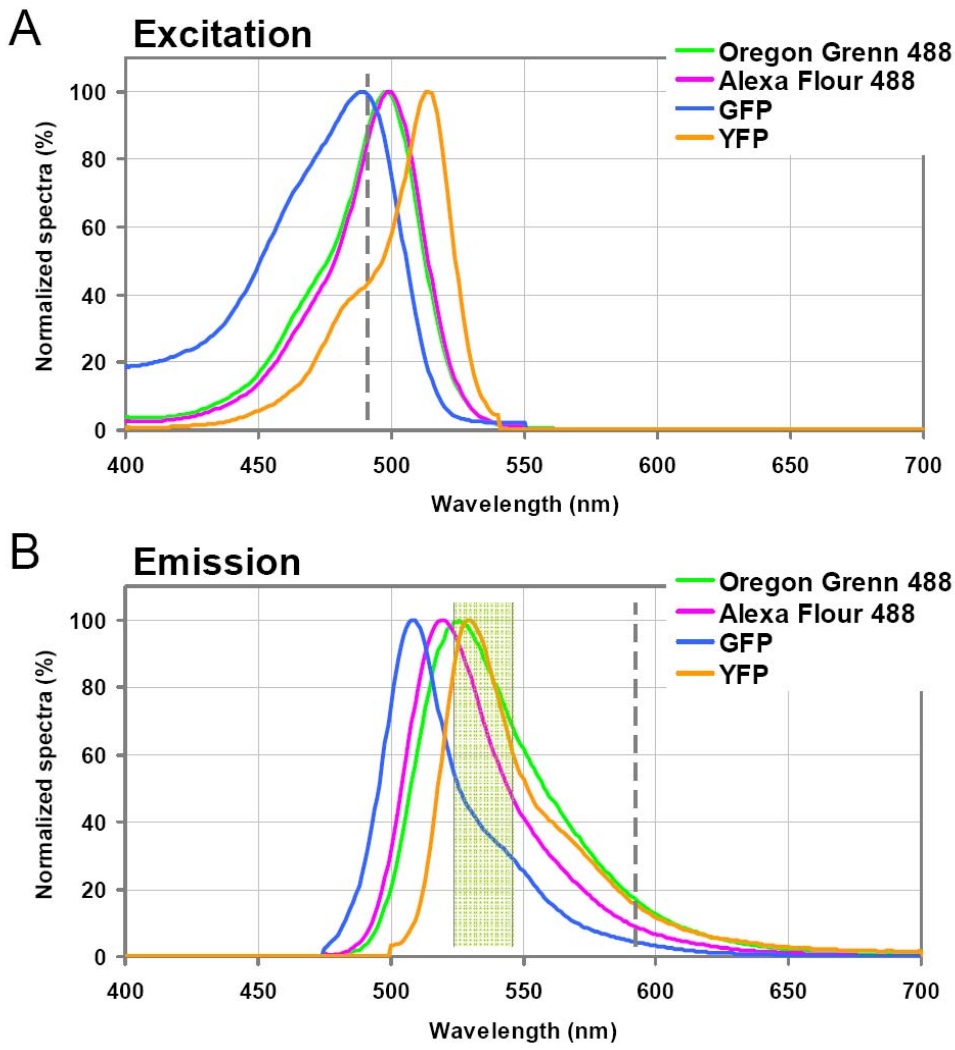

Figure 2-6 Excitation and emission spectra of different fluorescent markers used in our CW STED microscope. (A) Excitation spectra of the four fluorophores excited at 491-nm close to the peaks of Oregon Green 488, Alexa Flour 488, and GFP. For YFP illumination, the relative efficiency is sufficiently above 40%. The dash line denotes the excitation wavelength at 491 nm. (B) The corresponding emission spectra of the listed fluorophores. A detection window at 524 nm-546 nm is commonly used to select signals. The dash line is the wavelength of depletion beam at 592 nm.

2.2.2 Implementation of individual system configurations

Our CW STED microscopy system (Figure 2-7) contains laser sources, fiber launch systems, STED optical path, scanning stage and control modules, detection path, and scanning protocols. We first implemented the setups in light source system, and then two laser lines were brought in the main optical configuration with the fiber launches. Two laser beams were aligned individually to be merged with each other throughout the STED main optical path. The detection system was established as an extended main optical path which was directed into an optical fiber and a light detector. The sample scanners were commanded by a set of imaging protocols that also communicated with a detection module to register optical signals at every given position of a sample.

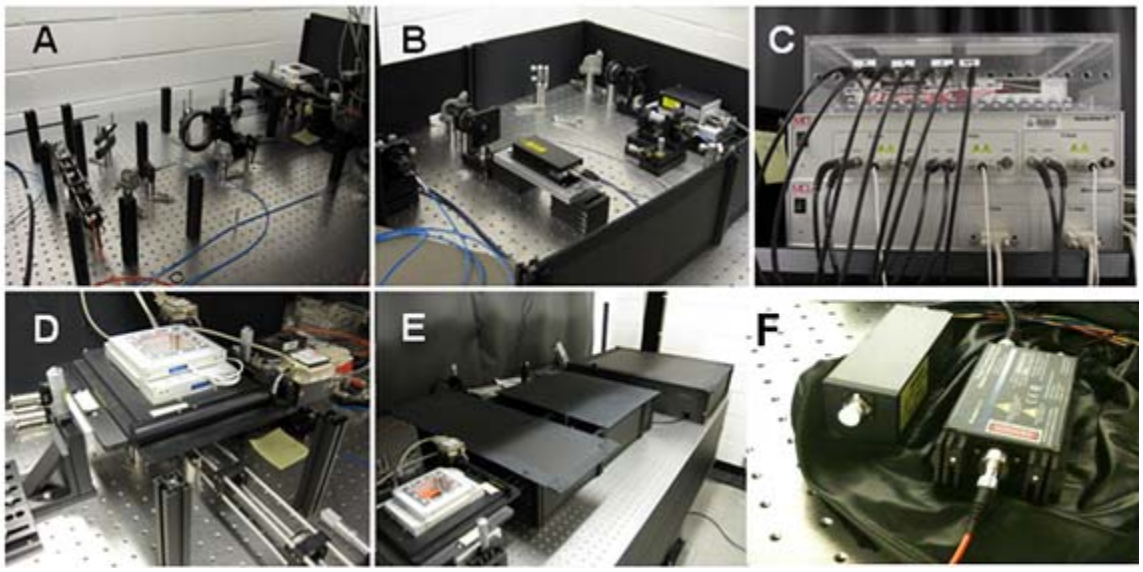

Figure 2-7 Experimental setups of the CW STED system (A) Layout of STED microscopy system; (B) The excitation and STED lasers; (C) Scanning stage controller module; (D) Point scanning stage; (E) Well-blocked system for higher signal-to-noise ratio; (F) Detection devices including APD and PMT.

2.2.2.1 Lasers and fiber in-couplers

To ensure an optimized coupling efficiency, lasers for excitation and depletion need to be precisely directed into single-mode fibers. In Figure 2-8, the 491-nm excitation laser (Calypso 25, Cobolt Ab) (A1) is first attenuated with a half-wave plate (A2) (AHWP05M-630, Thorlab) and a linear polarizer (A3) (10LP-VIS-B, Newport Corporation) combination. We then use two mirrors (A4 and A5) (10D20BD.1, Newport Corporation) to adjust the orientation of the laser beam with full degrees of freedom, thus enabling the high in-coupling of the laser to the single-mode fiber (A7) via the collimator (F280APC-A, Thorlabs) (A6).

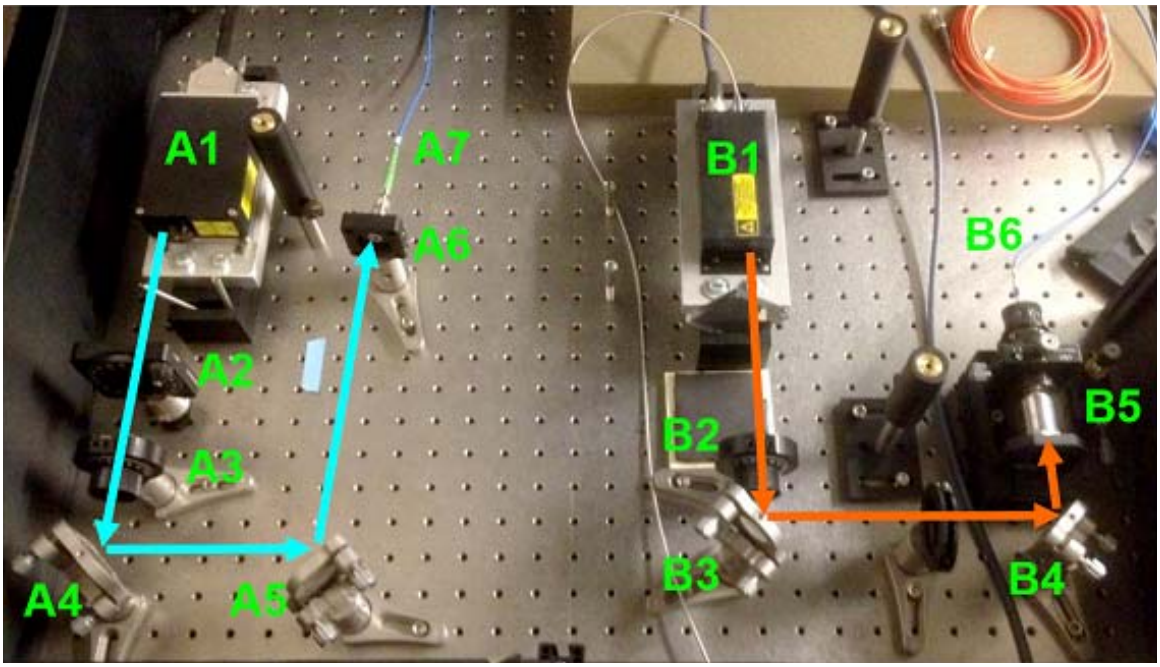

Figure 2-8 Lasers and coupling configurations that enable good in-coupling efficiencies from lasers to single-mode fibers. Excitation laser (A1) beam is directed into the fixed collimator (A6). To achieve an optimized efficiency for the depletion laser (B1) beam, a 5-axis stage (B5) is used. For each laser line, two mirrors (A4 and A5; B3 and B4) afford the full degrees of freedom to adjust orientation of laser beams. A2, half-wave plate; A3

and B2, polarizers; A7 and B6, single-mode fibers.

Similarly, the 1-W 592-nm depletion laser (VFL-P-1000-592, MPB Communications Inc) (B1) passes a linear polarizer (B2) and then two mirrors (B3 and B4) for the tuning of incident orientation of the laser to be coupled into the single-mode fiber (B6). The fiber coupler mounted at a 5-axis stage (F91-C1, Newport Corporation) (B5) allows us to reach the maximal coupling efficiency required to deliver a sufficient high of STED power. To facilitate the coupling alignment of single-mode fibers, we first connect a multimode fiber to an in-coupler for coarse adjustment; then, replace it with a single-mode fiber for further alignment.

2.2.2.2 Fiber launch systems

The fiber launch systems of the excitation and depletion beam are shown in Figure 2-9. Two laser beams are brought into the main STED system via single-mode fibers from the light source system. The depletion beam is launched with a beam collimator (F280APC-A, Thorlabs) (C1) at the other end of the fiber (B6). After a 45° reflection by the mirror (10D20BD.1, Newport Corporation) (C2), this beam is shaped with the vortex phase plate (VPP-1, RPC Photonics Inc) (C3) that results in a 2π phase retardation to generate a center-zero beam pattern. This phase mask is mounted on a two-axis translation stage (C4) to allow the marker on the plate to coincide with the center of the laser beam. This beam of 592-nm wavelength then is reflected by the dichroic filter (FF541-SDi01-25x36, Semrock) (C5) and merged into the main path with the excitation beam. The two reflective components (C2 and C5) provide sufficient degrees of freedom for the alignment along the main optical path.

As compared with the fixed collimator using for depletion beam (C1), the excitation beam is launched with a 5-axis stage (F91-C1, Newport Corporation) (D1) where the optical z-axis position can be adjusted to match the collimation level of the depletion beam at the back aperture of the objective. Therefore, the two laser beams are aligned on the focal plane in three dimensions. Similarly, this beam of 491 nm is reflected twice by the mirror (D2) and the dichroic filter (Di01-R488-25x36, Semrock) (D3) to enable optical alignment when merged into the main path.

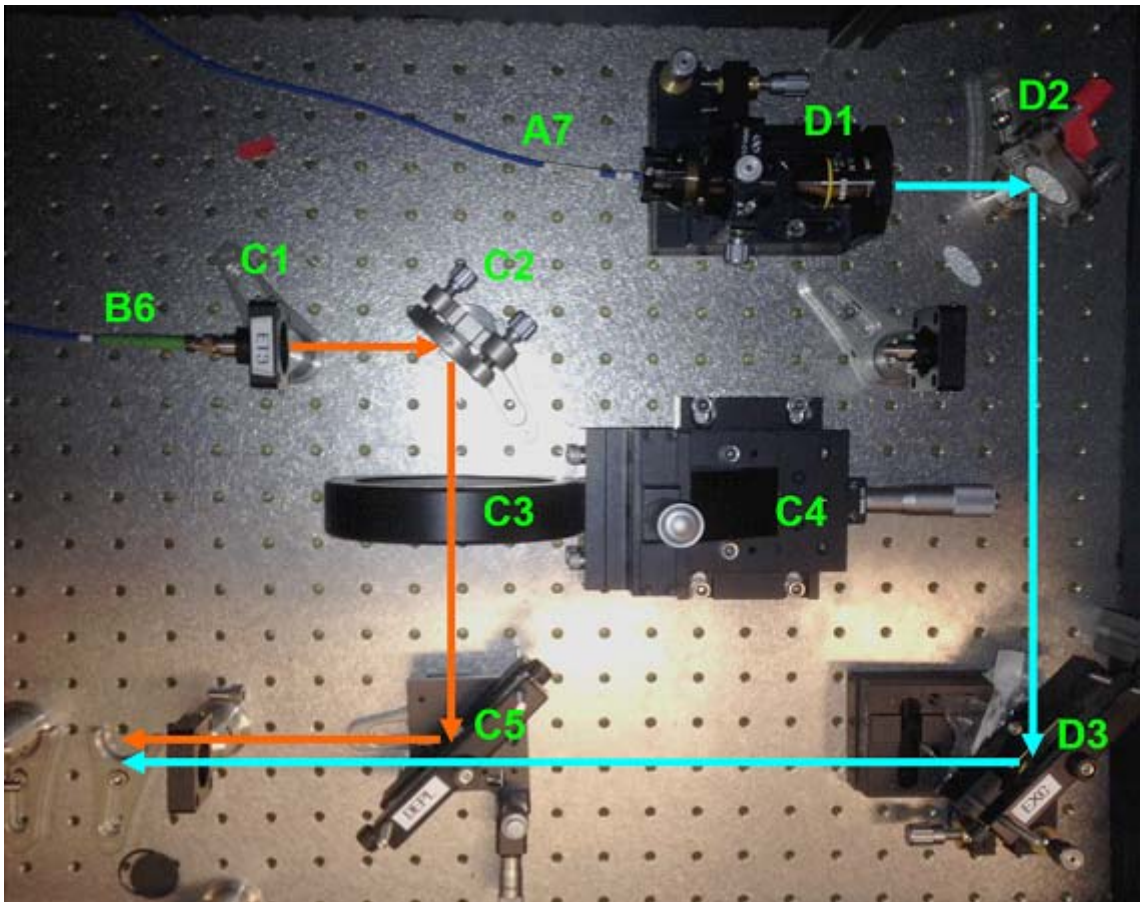

Figure 2-9 Fiber lunch systems for the excitation and the depletion beams. C1, beam collimator; C2, mirror; C3, vortex phase plate; C4, two-axis translational stage; C5, dichroic filter for the 592-nm beam; D1, 5-axis out-coupler; D2, mirror; D3, dichroic filter for the 491-nm beam; B6, single-mode fiber carrying 592-nm beam; A7,

single-mode fiber carrying 491-nm beam.

2.2.2.3 Main STED optical path

The optical components sited along the main path consist of two dichroic filters, a telescope lens pair, a 45°mirror, a quarter-wave plate, and a 100X 1.4NA objective lens and its holder. As discussed above, the two dichroic filters (C5 and D3) as shown in Figure 2-10 guide the two laser beams into the main path. These lights then pass through the telescope lens pair (Thorlabs) (E1 and E2) to achieve the best collimation in free space by fine tuning the distance of the lens pair. Figure 2-11 shows that the 45° mirror (E3) bends the excitation and depletion beams upward and then the quarter-wave plate (E4) transforms the beams in circularly polarized fashion at the back aperture of the 100X objective lens (E5), enabling the homogenous illumination. Therefore, two overlapped laser beams present on the focal plane with one Gaussian shape and one Gauss-Laguerre profile.

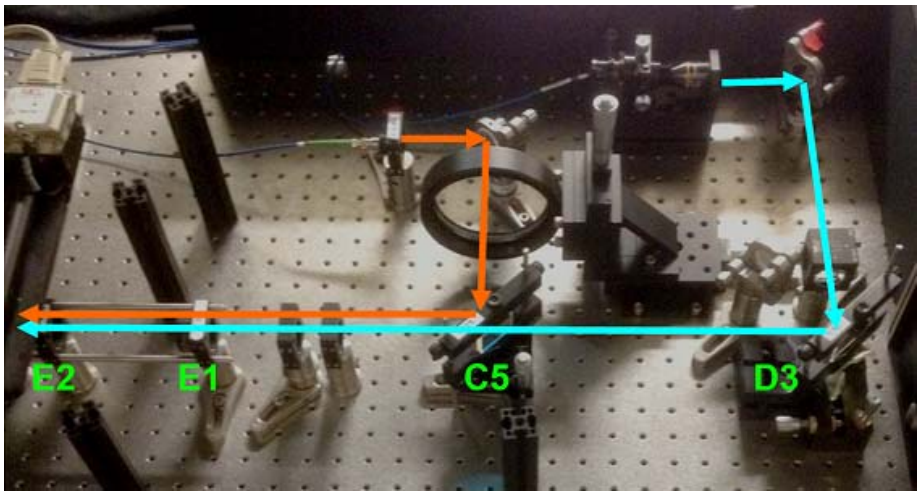

Figure 2-10 Main optical path of the CW STED microscopy system. Two dichroic filters (C5 and D3) allow laser beams to be merged along the main path. The telescope lens pair (E1 and E2) is used to maintain the optical collimation in free space.

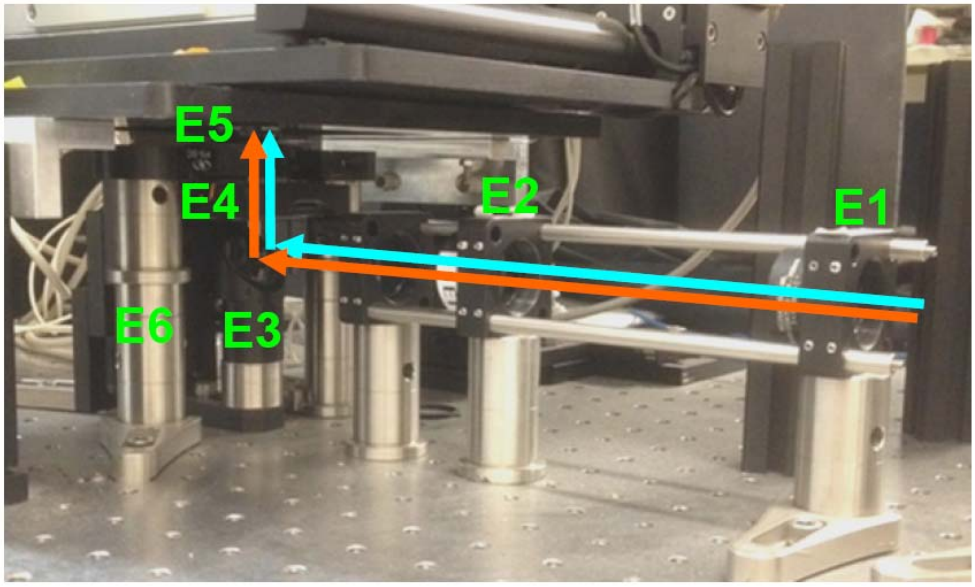

Figure 2-11 The 45° mirror lifting up the merged collimated beams toward the quarter-wave plate and the 100X objective lens. E3, 45° mirror; E4, quarter-wave plate; E5, 100X 1.4NA objective lens; E6, lens holder.

2.2.2.4 Sample scanners

Figure 2-12 shows the configuration of the sample scanner consisting of a nanometer- and a micrometer-positioning stage to reach high precision and large dynamic range scanning. The 3-axis nano-positioning piezo-driven scanner (NanoPDQ 375HS, Mad City labs) (F1) is used to perform a high speed and linear scanning over a 75 μm range in XY and a 50 μm range in Z. It includes position sensors for absolute position measurement and sub-nanometer resolution. It is mounted on a stepper motor driven microstage (Microstage-20E, Mad City Labs) (F2). The microstage affords a maximum range of 1 inch movement on the objective lens placement. This subsystem is connected to the control modules as shown in Figure 2-7C. The overall scanning stage is lifted by two translation stages (F3 and F4) for coarse focusing.

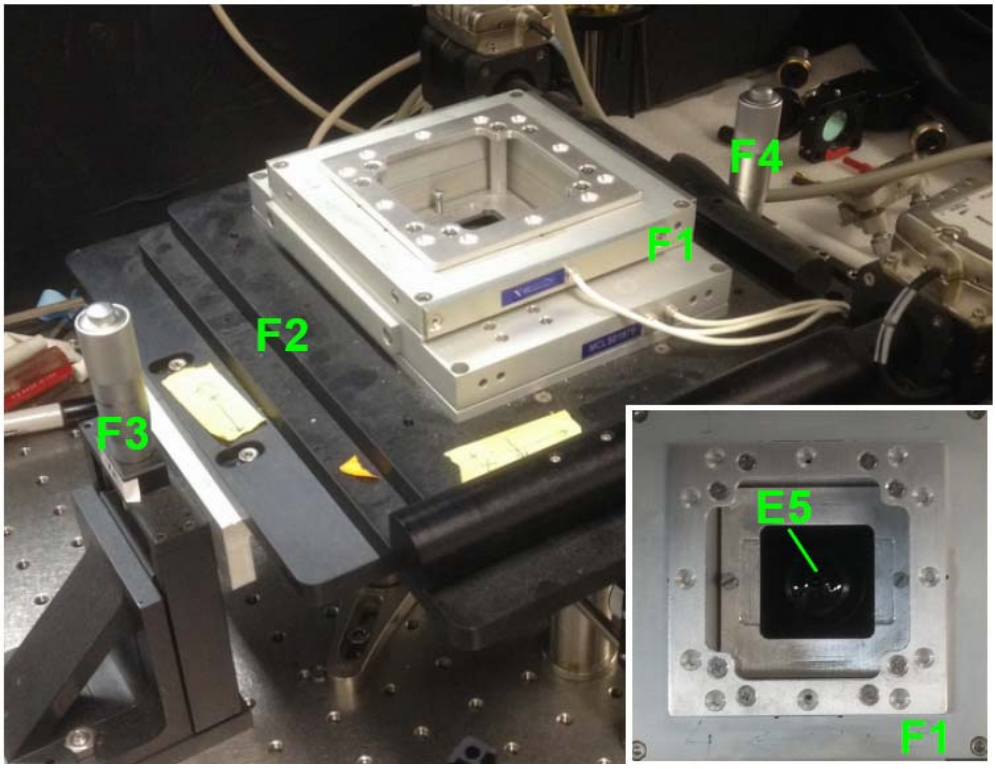

Figure 2-12 The configuration of the sample scanner consisting of a nanometer- and a micrometer-positioning stage to reach high precision scanning. F1, 3-axis nano-positioning piezo-driven scanner; F2, stepper motor-driven microstage. The inset shows the top view of the nano-scanner and the imaging objective lens (E5) at the center of sample holder.

2.2.2.5 Detection path

Fluorescence emitted from samples is collected with the same 100X objective lens. As a result, signals propagate backward as the forward pathway. The red-shifted fluorescence passes through two dichroic filters and then is selected by a band-pass color filter (FF01-535/22-25, Semrock) (G1) to increase signal-to-noise ratio of images shown in Figure 2-13. After reflected by the mirror (G2), the cleaned signals are carried in free space again through a telescope consisting of two achromatic doublets lenses (G3 and G4). The collimated light then is coupled into a multimode optical fiber

(AC254-150-A-ML, Thorlabs) (G5) by a collimator (G6). The other end of this fiber is connected to either a PMT or APD single-photon detector (Figure 2-7F).

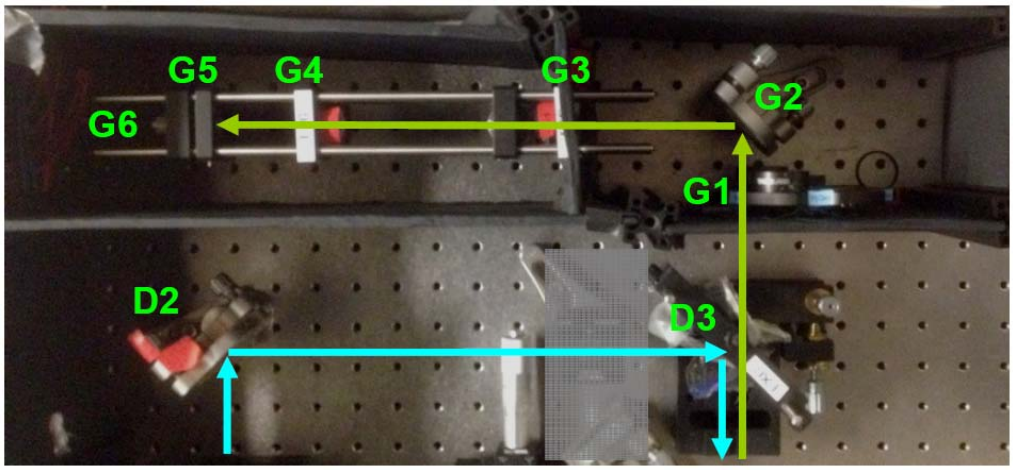

Figure 2-13 Detection pathway consisting of a band-pass filter (G1) that rejects the intense scattering light from depletion beam, followed by a 45° mirror (G2) that directs the signal to a collimator (G5) and into a multimode optical fiber (G6) via a telescope lens pair (G3 and G4) that propagates the signal at free space.

2.3 Development of a dual-color STED microscope through a common-depletion laser line

Although a single-color system is sufficient to demonstrate the improved resolving power from a STED microscopy, most of biological and physical studies indeed rely on a dual-color system for the understanding of molecular or structural co-/de-localization. Consequently, in this section, we implemented a CW two-color STED microscopy system using a common-depletion laser line in order to study those questions detailed in the later chapters.

2.3.1 Separation of two colors for STED imaging

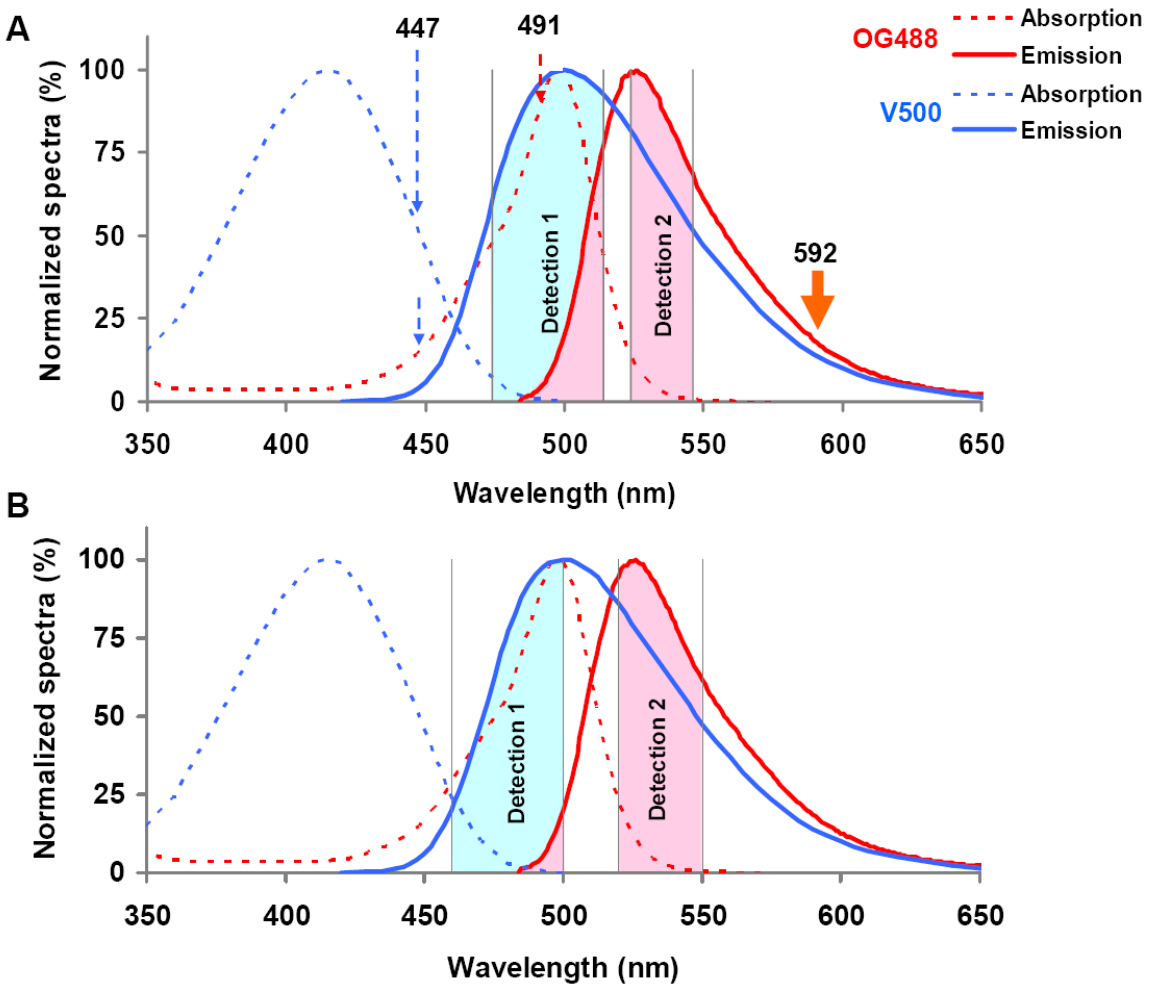

Figure 2-14 Absorption and emission spectra of the dye pair: Oregon Green 488 and V500. The color separation is fulfilled by either selective excitation or detection. Both dyes are depleted with a common laser line at 592 nm. (A) Detection window 1 (484-514) and window 2 (524-546). (B) Detection window 1 (460-500) and window 2 (520-550) for better signal-to-noise ratio.

We expanded our single-color setup by adding the second excitation laser line at 447 nm to the existing layout. Different from conventional multicolor imaging systems which only deal with the color separation by choosing different illumination wavelengths and the corresponding detection windows, a multicolor STED microscope, however, needs to

take depletion lights into consideration. A strong STED beam could cause significant background when it is close to absorption spectra of other dyes. To simplify a two-color CW STED system, we choose a common-depletion setup where a doughnut-shaped depletion beam at 592-nm is used to achieve STED imaging for both fluorescent dyes. The working principle for our common-depletion dual-color STED microscopy is illustrated in Figure 2-14 where the dash lines are the excitation spectra for those dyes, Oregon Green 488 and V500, and solid lines for their corresponding emission spectra. The 491-nm laser is still designed to excite Oregon Green 488 as single-color operation. A 447-nm light illuminates the dye V500, which has a great Stokes shift, and therefore the 592-nm light can deplete this dye at the red-shifted tail of the spectrum with sufficient stimulated emission efficiency.

To enable physical color separation, appropriate detection windows should be chosen for each fluorescent dye. Physically, the 447-nm light excites V500 as well as Oregon Green 488. This thus could cause severe signal crosstalk between both dyes. To overcome this issue, we selected a detection window (detection 1, 474-514nm) which can collect major emission from V500 but only small amount from Oregon Green 488 (Figure 2-14A). An alternative window to effectively suppress crosstalk is shown in Figure 2-14B where detection window 1 between 460 and 500 nm can reject most emission signals of Oregon Green 488. For the second imaging channel, the 491-nm laser excites Oregon Green 488 at a high efficiency but does nearly zero for the dye V500. Therefore, the second detection window only read fluorescence from Oregon Green 488, even though their spectra are largely overlapped in detection window 2. An optional filter of wider detection width is shown in Figure 2-14B. This combination of fluorescence dyes will

enable intrinsically color-separable STED imaging without the need of color-unmixing post-processing.

2.3.2 Implementation of extended system for two-color STED imaging

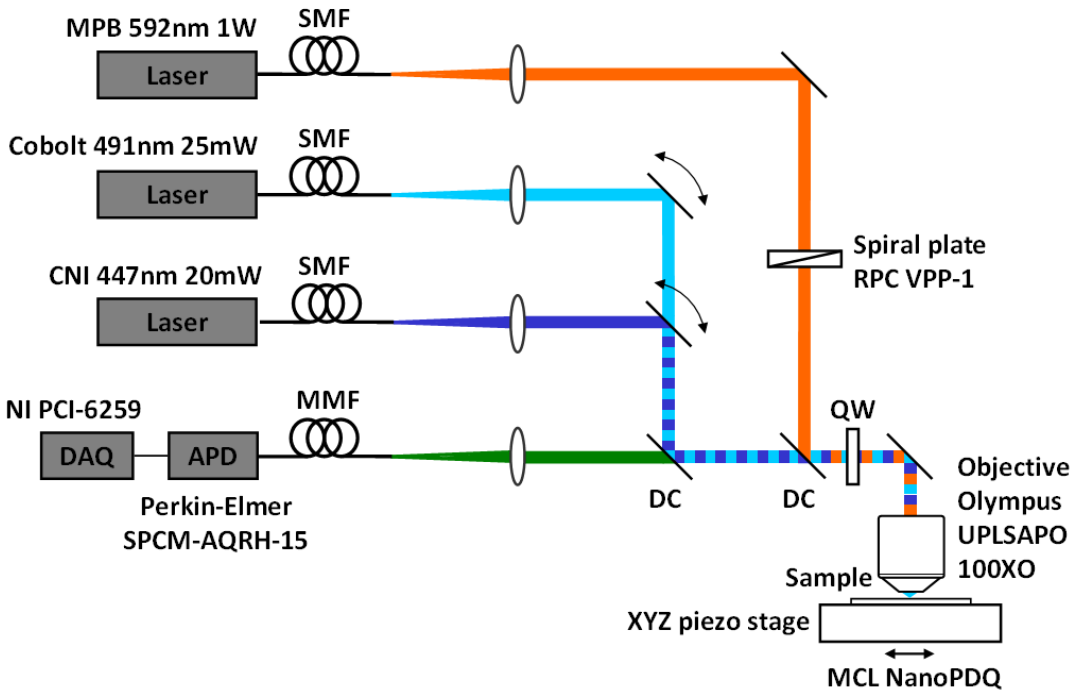

Figure 2-15 Dual-color CW STED microscopy system employing two excitation beams and one common-depletion light to image two fluorescent dyes which can be spectrally separated with different laser lines or different detection spectra. The 447-nm laser beam is overlapped with the first excitation light and the STED beam at the focal plane.

The established dual-color STED layout is shown in Figure 2-15. Based on the single-color layout, we expanded our STED setup by incorporating the second excitation laser line at 447 nm into the CW system in which we used the 592-nm laser as a common depletion source to fulfill STED phenomenon for the second dye. A diode laser at 447 nm is installed to deliver a laser line for the excitation of V500. This laser needs to achieve a quality of imaging the PSF as good as the first excitation laser. The extended

configurations are designed to allow this light to spatially coincide with the first excitation beam and the depletion beam at the focal plane.

2.3.2.1 447-nm laser in-coupler and fiber launch

To efficiently implement this two-color CW STED system, we employed a low-cost diode laser for the illumination of the second dye, V500. The beam shape of a diode laser is usually long or close rectangular as shown in the inset of Figure 2-16. This 20-mW diode laser (PGL-V-H-447, CNI) (H1) thus is first cleaned with a single-mode polarization-maintaining fiber to form a Gaussian beam. Similarly, the laser beam is guided by two mirrors (H2 and H4) and then coupled through the collimator (H5) into the fiber (H6). At the other end of this fiber is the fiber launch which is placed at the side of the main STED system. This fiber launch (H7) also requires full degrees of freedom of adjustment. So an infinite-corrected 10X objective is used as a collimator here. The in-coupler allows for the fine-tuning of beam collimation in order to match its focal position with the other two lights. Although the power usage for excitation is not as high as 20 mW, a sufficient coupling efficiency is desired for a better beam shape. This laser line is essentially launched outside the main STED system but we place it as close as possible to the main optical path to avoid the long-distance propagation in free space and space-dependant vibration issue.

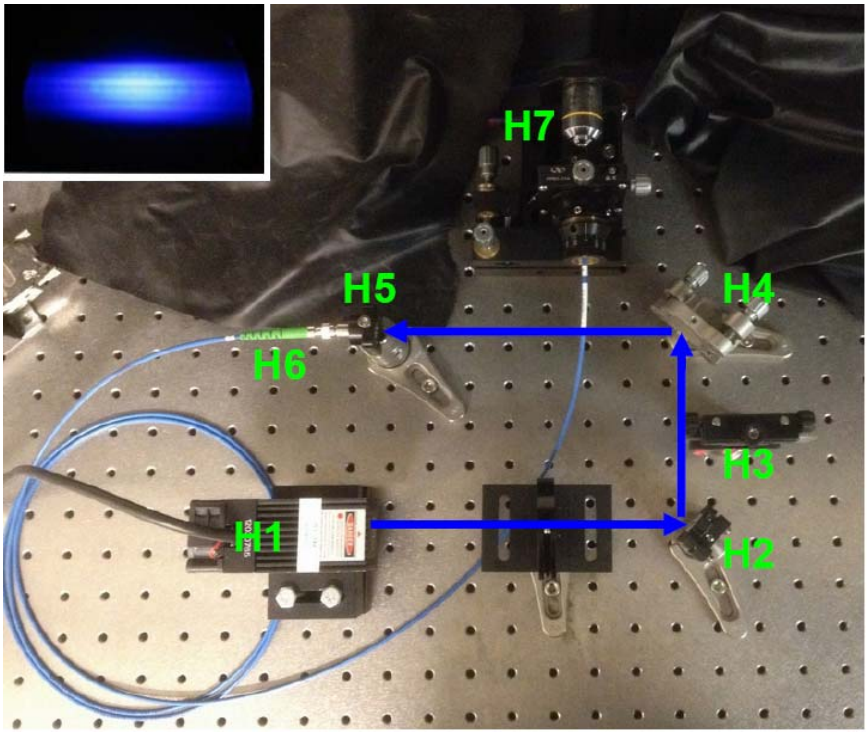

Figure 2-16 447-nm diode laser line and its fiber launch. H1, 477 nm diode laser; H2 and H4, mirrors; H3, adjustable attenuator; H5, beam collimator; H6, single-mode fiber; H7, fiber launch and 5-axis stage.

2.3.2.2 Merge 447-nm laser line into main STED path

The 447-nm laser line is placed close to the launch of the 491-nm laser because the two laser lines share the same dichroic fiber which reflects most lights (~100%) at 491 nm and approximately 50% at 447 nm. The loss of power for 447-nm laser here is acceptable since the needed amount is fairly low compared to the output power. To enable individual alignment of these two lasers, two optical components are added to the 491-nm laser line. First, a 50-50% beam splitter (J1) is placed in the path of 491-nm laser to merge 447-nm line before reaching the first excitation dichroic mirror. One more dielectric mirror (J2) is added to the second excitation laser alone so that both excitations can be aligned independently. Figure 2-17A is the overall setup of our dual-color STED

microscopy system. The components to align three laser beams are shown in Figure 2-17B by fine-tuning the four adjustors.

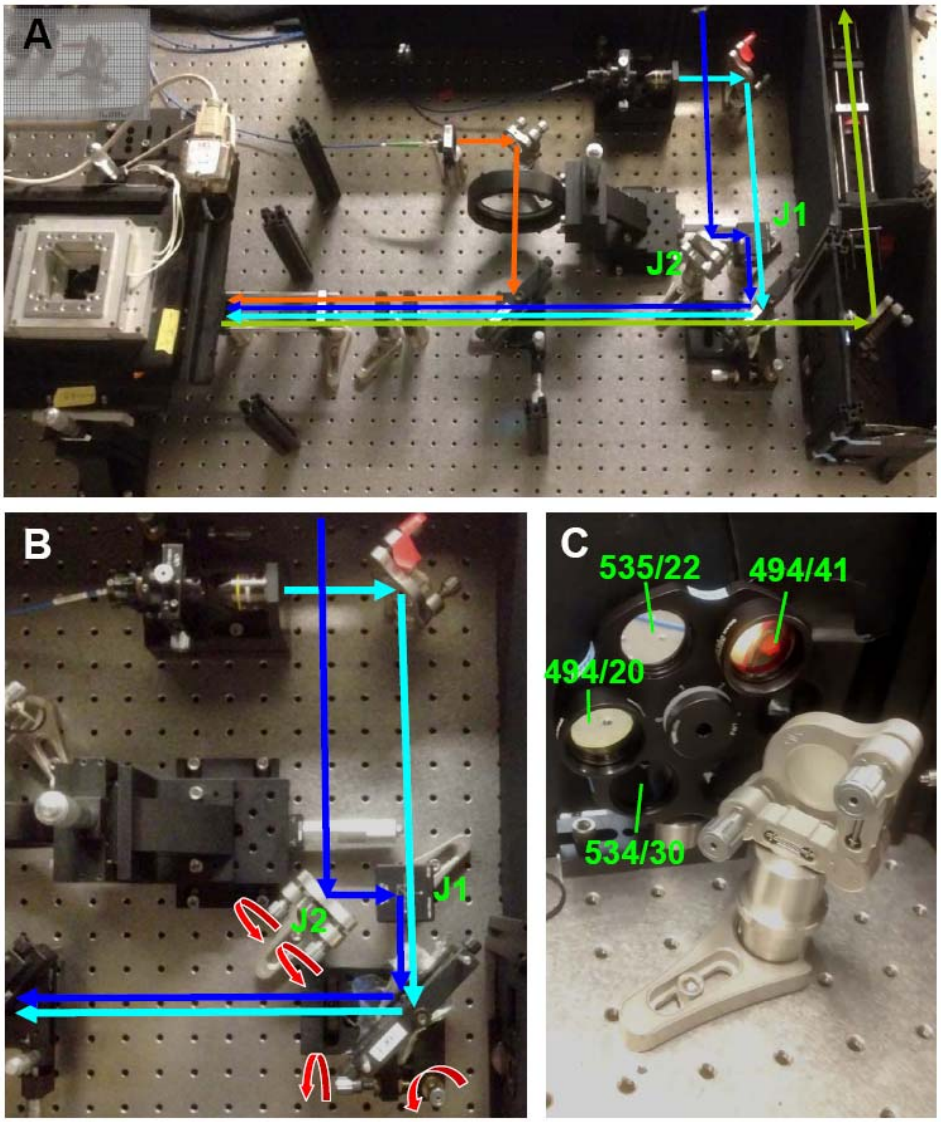

Figure 2-17 Experimental setup of our dual-color STED system. (A) 447 laser line is merged into the main optical path through a mirror (J2) and a 50%-50% beam splitter (J1). (B) Three laser lines are aligned by fine-tuning the four screws at the stage of dichroic filter and at the mirror stage (J2). (C) A filter wheel device is used to smoothly switch the corresponding color filters while conducting two-color STED imaging. Two filters (535/22 and 534/30) are designed for Oregon Green 488; Two filters (494/41 and 494/20) for V500 detection.

The added optical components should be positioned as close to the dichroic fiber as possible to decrease the sensitivity to mechanical drift caused by temperature fluctuations. The two screws at the dichroic filter are first adjusted to bring the 491-nm laser beam toward the center zero of the doughnut-shaped light. Then we adjust the two screws at J2 in Figure 2-17B to make the 447-nm beam either match the aligned 491 beam or the depletion beam. In practice, the former method offers better accuracy of alignment due to small beam size. In addition, a filter wheel device is used to replace the flip stage for the ease of switching filters (Figure 2-17C). Each dye has two different band-pass filters that have different band width and central wavelength depending on the samples.

2.4 Validation of imaging performance

2.4.1 PSFs of three laser beams

To ensure optimal alignment and beam quality, the shape of these three laser lights was characterized by scanning a ~80-nm gold bead at its focal plane. With gold beads, this dual-color system offered a confocal resolution of ~210-230 nm for the 447-nm light and of ~215-235 nm for the 488-nm light (Figure 2-18, lower panels). This difference was caused by different probing wavelengths. The central FWHM of the depletion beam was approximately 200 nm. Hence, the three beams are manipulated at a well-confined condition, close to the theoretical diffraction limit. Experimentally, three laser beams are aligned with a gold bead to obtain the errors among them. The misaligned distances are corrected by the real time tracking of their positions. Although these three beams may not be perfectly aligned in reality, the subtle deviations can be corrected with a

common-depletion STED beam. Experimentally, the central zero of doughnut-shaped light uniquely determines the center of effective point spread function for both excitation lights. But the deviation may lead to the loss of signals because major depletion occurs at the peak intensity of excitation beams.

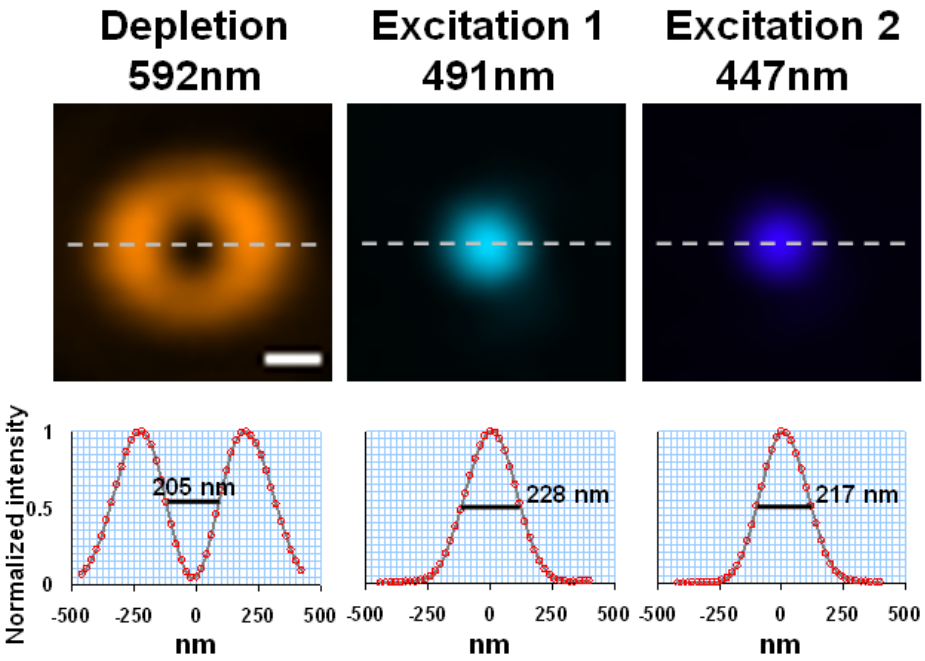

Figure 2-18 Point spread functions of two excitation beams and the common depletion light. The measured FWHMs show the dimension of the laser beams are close to the diffraction limit ~200 nm, implying this system is well optimized. The beam shape of the 447-nm laser light is circularly symmetrical after it is launched via a single-mode fiber.

To validate the performance of this dual-color system, we next observed a biological sample where we co-labeled Ac-tub and ACIII protein in a primary cilium of HFF cells with Oregon Green 488 and BD V500 fluorophore, respectively. As a result, we can diagnose any crosstalk between these two channels according to the known patterns of molecular structures such as Ac-tub. The results are shown in Figure 2-19 where Ac-tub

revealed a differential localization pattern from ACIII that was discrete over a cilium. Also, the ACIII labeled with V500 was found at the base of the cilia from a 494/41-nm band-pass filter but not seen from 535/22 filter. There is no significant crosstalk between the two channels. Therefore, this dual-color system inherently does not require unmixing post-processing.

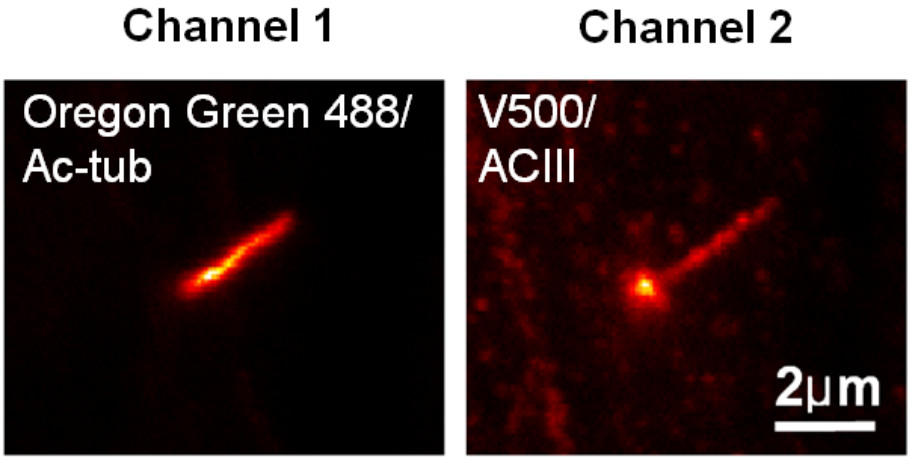

Figure 2-19 Validation of this two-color imaging system showing the ideal color separation of Oregon Green 488 and V500 dyes with the corresponding filters. The pattern of Ac-tub labeled with Oregon Green 488 was observed from the first channel and ACIII of discrete distribution is only seen from the second channel.

2.4.2 STED resolution characterization

For the validation of the attainable resolution of our STED superresolution microscope, we imaged Oregon Green 488 and V500 dyes immobilized on cover glass. Oregon Green 488 fluorophores (Oregon Green 488 goat anti-rabbit, Invitrogen) and V500 (Horizon™ V500 Streptavidin, BD Biosciences) were injected into a flow channel above a #1.5 cover glass embedded in PBS medium and allowed to settle on the glass surface. The laser powers used for STED imaging were ~2-5 µW for excitation beams

and ~100 mW for 592-nm depletion beam, measured in the back aperture of the objective lens. All images were recorded point-wise with a pixel size of 25 nm and dwell time of 20 μs by a stage scanner. Quantitative measurement of the resolution and line profiles of the confocal and STED images were based on untreated images which were analyzed using ImageJ.

Typical side-by-side comparisons of confocal and STED images for Oregon Green 488 and V500 fluorophores are shown in Figure 2-20A and Figure 2-20B. The magnified insets demonstrate the resolution enhancement using STED microscopy, compared to the clusters which are indistinguishable in a diffraction-limited confocal image. The comparison of the FWHM of intensity profiles of a single particle demonstrated the significant resolution improvement of our STED system (Figure 2-20, C and D). The optical resolution estimated in the focal plane was ~200-230 nm for confocal and between 50 and 60 nm for STED from both fluorescent markers, showing a ~4-fold resolution improvement. Hence, using the Oregon Green 488 and V500 dye pair, our common-depletion dual-color STED system allows us to study biological structures in superresolution scale without substantial signal crosstalks. Also, the inherent capability of resistance to the inevitable subtle misalignment in this system is suitable for the investigation of molecular localization.

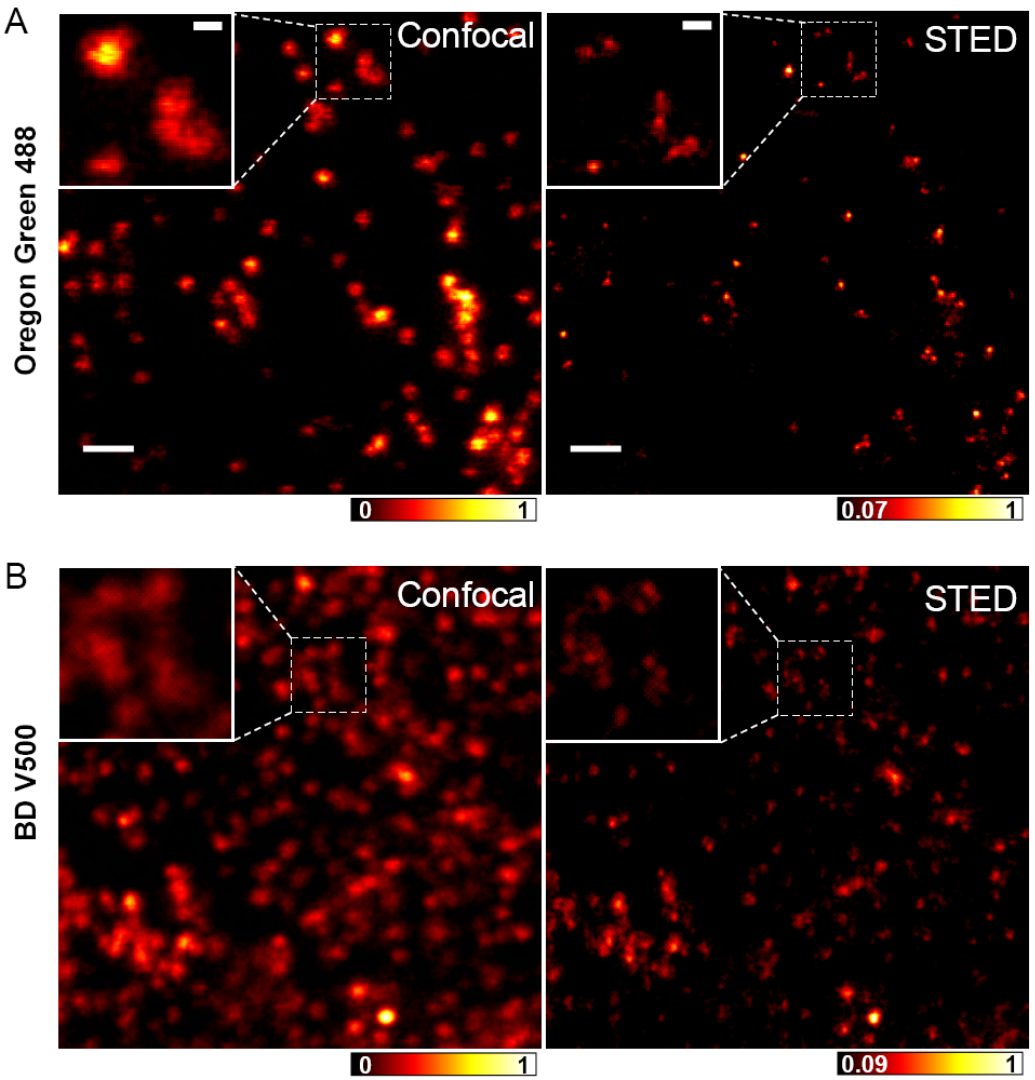
A
Oregon Green 488
Confocal
STED
0
1
0.07
1
B
BD V500
Confocal
STED
0
1
0.09
1
Oregon Green 488
C
a.u.
1
0.5
0
225nm
50nm
-300
-150
0
150
300
nm
BD V500
D
220nm
55nm

Figure 2-20 Resolution improvement of STED superresolution microscopy. (A and B) Comparison of confocal and STED images of Oregon Green 488 and V500 fluorophores, respectively. The STED images demonstrate distinguishable particles that cannot be resolved by the confocal microscopy (insets). The intensity scales represented the photon counts of pixels normalized by the maximal photon count of an image. Scale bars, 1 μm for the main images and 250 nm for the insets. (C and D) Normalized intensity profiles of one of the particles in the raw STED images and their confocal counterparts. FWHMs shown in the profile of confocal image were estimated based on a fitted Gaussian curve.

Moreover, we tested this STED system with biological samples which are usually more challenging and different due to the three-dimensional structure or high staining background. Therefore, the cells were stained with Oregon Green 488 phalloidin to visualize the actin filaments of filopodia under the STED microscope. Our STED images (Figure 2-21) showed promising visualization of the density of actin bundles, a component of the cytoskeleton of the cells. However, confocal results usually display blurred information of bundled filaments. In Figure 2-21, two adjacent filaments (marked as arrows) are recognized with STED imaging compared to confocal data which only visualizes one. The STED images allow us to obtain details of the arrangement, the correct size of the filopodia, and the distances between filopodia. In addition, the different types of possible filaments bundles can be resolved in the STED images, which were scanned with the power of ~130 mW of the STED laser. This result shows that our STED microscope enables better dimension characterization of cellular structure as well as differentiation of features within undiffracted scale.

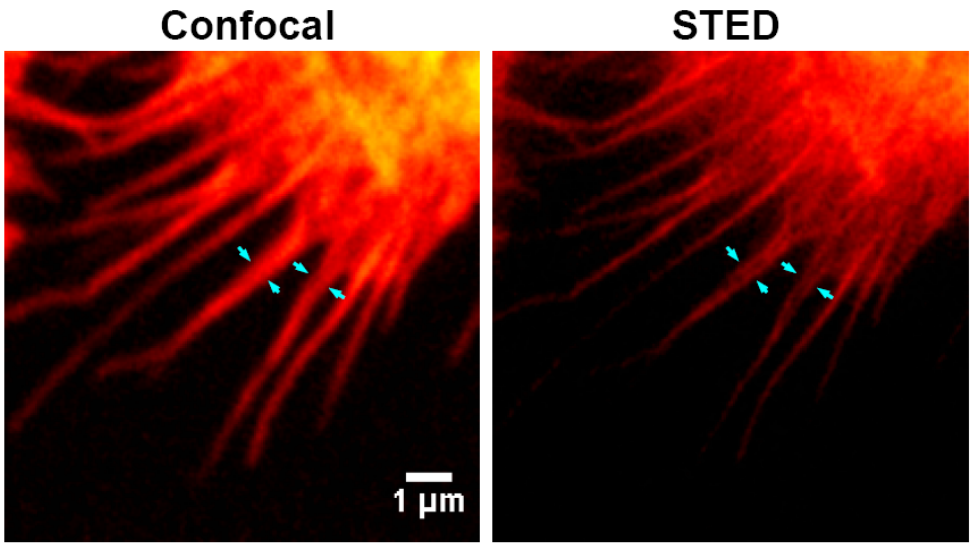

Figure 2-21 STED imaging of actin filaments in MKN28 cells demonstrates the resolution improvement for biological samples using STED microscopy. The STED result distinguishes adjacent actin filaments (arrows) but the confocal does not resolve bundled filaments.

3 STED Microscopy Reveals Differential Localization of IFT88 and ACIII in Primary Cilia

3.1 Localization of IFT88 and ACIII to Primary Cilia of Human Fibroblasts

We first examined the localization of ACIII and IFT88 to primary cilia of human foreskin fibroblasts (HFF-1). Cells were cultured to ~80% confluence and then serum starved for 48 hours to promote primary cilia growth. Primary cilia were identified by staining with antibodies against acetylated α-tubulin (ac-tub) (Figure 3-1). The percentage of ciliated cells and the ciliary length increased with cell confluence. Immunostaining of ACIII and IFT88 showed dissimilar localization in primary cilia when compared with ac-tub as a reference. In general, ACIII localized to cilia and centrioles (Figure 3-1A-C), while IFT88 was concentrated at the tip and the base of the primary cilium (Figure 3-2D-F). Comparison of the colocalization of ac-tub/IFT88 and ac-tub/ACIII further demonstrated that ACIII localized at both centrioles (green in the inset of Figure 3-1C), while IFT88 did not appear at these centrioles (inset, Figure 3-2F).

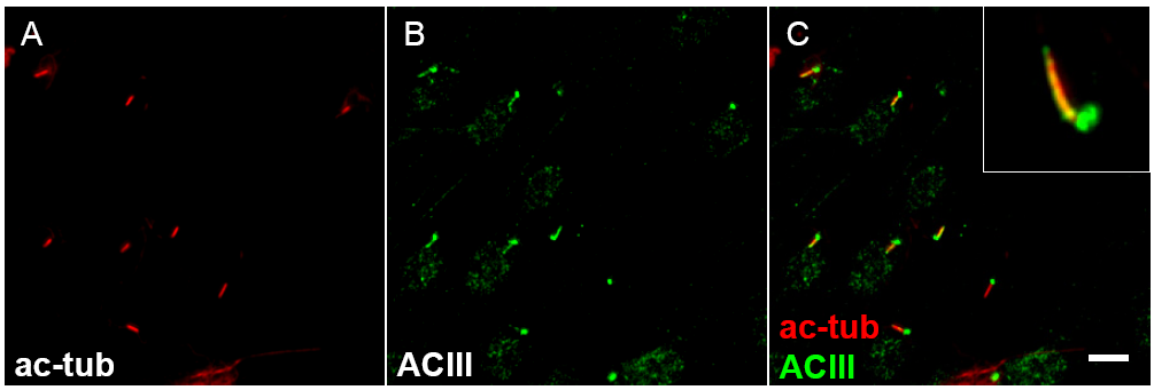

Figure 3-1 ACIII localization to primary cilia of human fibroblasts imaged from a wide-field epi-fluorescent microscope. (A) Immunofluorescent images of human fibroblasts stained with antibody against ac-tub (red) indicated solitary primary cilia in

individual cells. (B) ACIII-labeled fluorescence (green) showed ACIII localization to primary cilia in the vicinity of the nucleus with one bright end. (C) A merged epifluorescent image revealed that ACIII (green) in the ciliary compartment was partially overlapped with the axoneme of the cilium (red). ACIII also localized to the basal bodies where bright and large clusters were observed (inset). Scale bar, 10 μm.

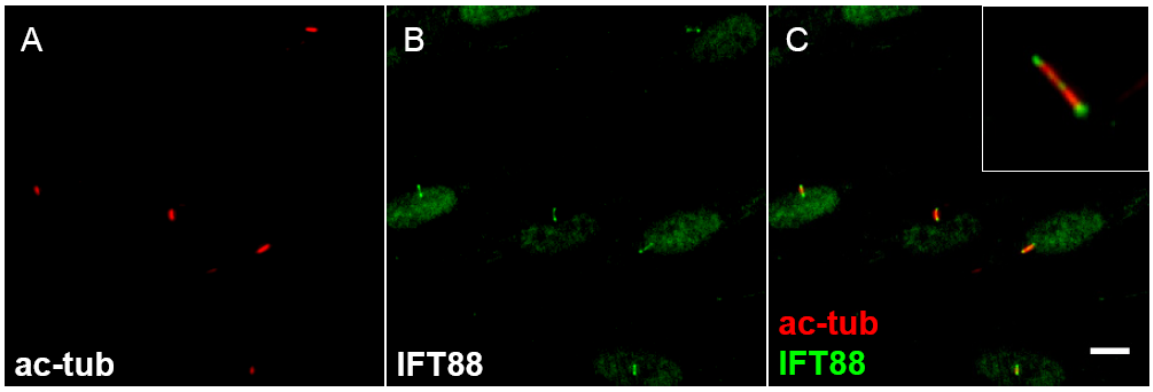

Figure 3-2 IFT88 localization to primary cilia of human fibroblasts (A) Immunofluorescent images of human fibroblasts stained with antibody against ac-tub (red) (B) Human fibroblasts were immunostained with IFT88 antibody showing dumbbell-shaped localization, indicating a different distribution from the homogenous ACIII distribution along a cilium. (C) A merged image from ac-tub (red) and IFT88 (green) showed IFT88 accumulated at the tip and the base of a cilium and did not extend toward the mother centriole at the basal end. Scale bar, 10 μm.

3.2 STED Imaging Reveals a Periodic Punctate Pattern of ACIII in Fibroblasts

3.2.1 STED imaging of ACIII distribution along ciliary compartment

In order to better visualize ACIII, and potentially understand the correlation between its localization and functions, we conducted superresolution imaging of immunostained ACIII (Alexa Fluor 488) in HFF-1 cells. In contrast to previous understanding that ACIII distributes homogenously along a primary cilium (when imaged with conventional

diffraction-limited microscopy), some STED images indicated that ACIII of at least 50% of primary cilia formed a punctated pattern with a roughly equal spacing between adjacent puncta. The STED images in Figure 3-3A and 3B demonstrate the visualization of individual puncta (marked with white arrows) that were not clearly distinguishable in confocal imaging. In Figure 3-3C, line profiles of the normalized intensity extracted from the confocal and STED images (Figure 3-3A) showed that the STED image enabled visualization of distinguishable punctated pattern of ACIII. For instance, STED revealed five groups of ACIII puncta in line 1-1', emphasized with arrows, while the corresponding confocal image could not resolve those features near the tip of the primary cilium.

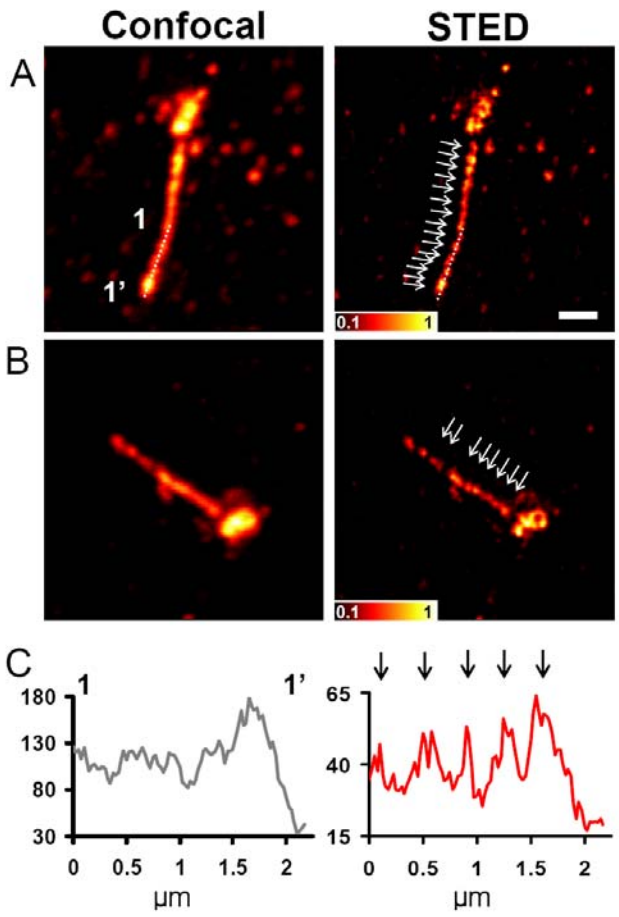

Figure 3-3 STED superresolution microscopy revealing a periodic punctate distribution of ACIII in human fibroblasts. (A, B) Superresolution images normalized by the maximal photon count revealed a discrete localization of ACIII clusters with approximately equal spacing between adjacent puncta (A and B, right). The white arrows marked in the STED images indicate individual ACIII puncta along primary cilia, compared to the corresponding diffraction-limited confocal images, which display a nearly continuous distribution of ACIII, particularly in (B, left) for confocal. (C) Intensity profiles along the white dotted lines 1-1' in (A). The STED images (C, right) showed five separable ACIII puncta marked with black arrows, not resolved in the confocal profile (C, left). The number in y-axis represents the photons counted with APD per pixel within the acquisition time.

3.2.2 Resolving centriole orientation using STED microscopy

In addition to the localization along the cilia, ACIII staining also showed a high intensity of signals at the basal end of the primary cilia (Figure 3-4, A and B). STED imaging of the basal end of cilia revealed two isolated clusters of ACIII labeling, each possessing a ring-shaped or a two-puncta structure (right panels of Figure 3-4, A and B). Comparison with the staining of pericentrin (Figure 3-4C) suggested these clusters localized at the region occupied by the centrioles. Therefore, STED images of ACIII staining provided the structural information of the peripheral edges of centrioles, enabling the identification of the orientations of both centrioles as shown in Figure 3-4A and B. The STED images indicated that some centriole pairs were aligned longitudinally with the axonemes, such that their orientations were identical (Figure 3-4A), while the centrioles in most other cells were anchored in parallel to the axonemal direction but oriented almost 90 degrees to each other (Figure 3-4B). In addition, most mother centrioles were aligned to the axis of the cilium (shown in Figure 3-4A, right and Figure 3-4B, right). Nevertheless, in a few cells, the mother centrioles were positioned with their axis at an angle to the direction of the cilium, implying that the cilium in the base may be bent by an extracellular force or that the cilium had an inclined growing direction after the centriole was anchored to the cell membrane. Through STED microscopy, we were able to identify the location and orientation of centriole pairs which were arranged either longitudinally along the cilia direction or side-by-side with an angle between each other. Hence, STED superresolution microscopy serves as an unprecedented means to collect statistics of molecular structures of primary cilia and to gain new insight into the underlying functional significance of molecules.

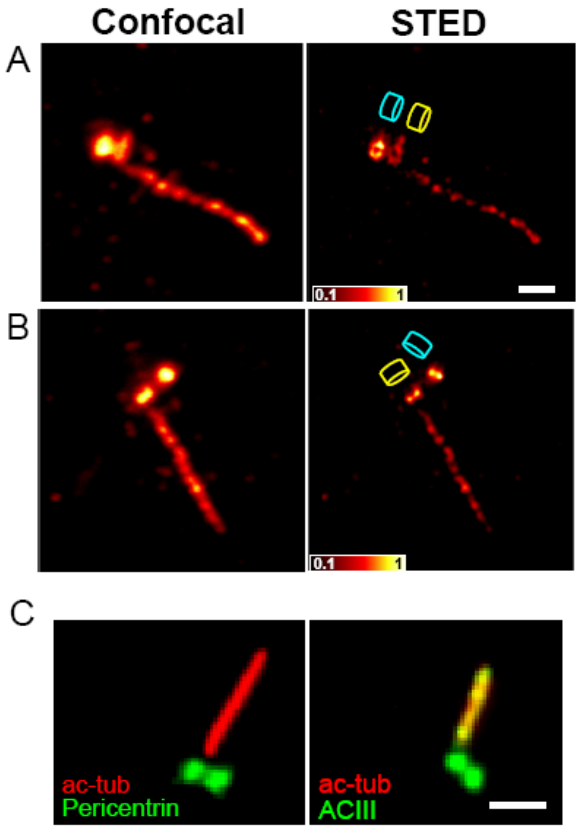

Figure 3-4 STED imaging revealing the orientation and location of the mother centriole (yellow cylinder) and the daughter centriole (blue cylinder), showing as two pairs of puncta. A longitudinal arrangement of the centriole pair is illustrated in (A, right) with identical orientation, and a nearly orthogonal arrangement of the centriole pair is illustrated in (B, right). The confocal observation, however, merely revealed an approximate location of the centriole pairs. Scale bar, 1 μm. (C) Staining of pericentrin (green) and ACIII (green) around ac-tub (red) showed a similar pattern at the base of primary cilia. The color overlapping (yellow) was caused by the localization of both ACIII and ac-tub along the cilium. Scale bar, 2 μm.

3.2.3 Quantitative analysis of the ACIII puncta

Next, we analyzed the average size of the ACIII puncta in the primary cilia. The size of each structure was determined by measuring the width of ACIII fluorescence in the

direction orthogonal to the axis of the cilia, as defined in Figure 3-5A. A sample of five clusters were measured in confocal and STED images and the comparison of normalized intensity of line profiles (labeled with 1 to 5 in Figure 3-5A) are shown in Figure 3-5B. The size and width of these ACIII clusters, which were overestimated by conventional microscopy due to the diffraction limit, were better estimated with STED microscopy. Specifically, the width of ACIII at position 5 was measured to be smaller than the diffraction limit, or 112 nm, an impossible measurement for a conventional confocal microscope.

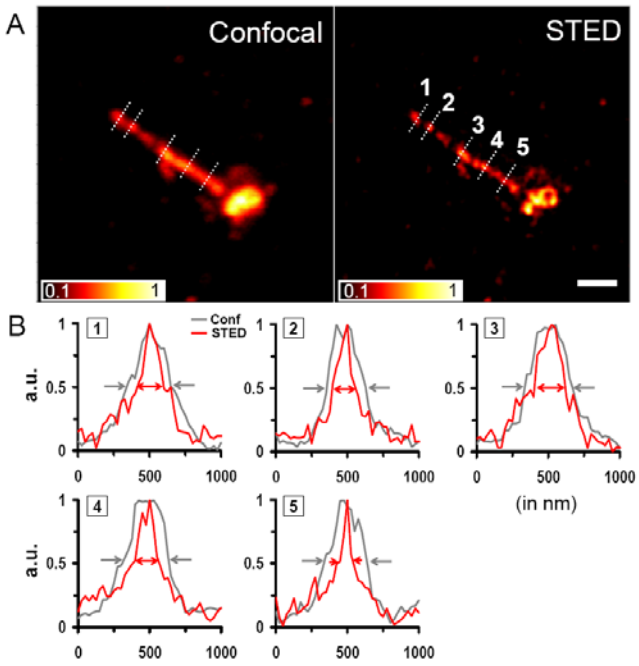

Figure 3-5 Measurement of ACIII puncta in human fibroblasts. The widths of clusters in the direction orthogonal to the axis of the cilia were measured. (A) The five locations of ACIII clusters to be analyzed. Scale bar, 1 μm. (B) Normalized intensity profiles extracted from the raw data of the clusters labeled with 1 to 5. The intensity profiles of the STED image (red line) are clearly narrower than the ones of the confocal image (grey), implying that diffraction-limited imaging poorly characterized the size of ACIII puncta.

Moreover, the Figure 3-6A indicates the ACIII widths based on the FWHM of raw data for clusters 1 to 5, ranging from 112 to 207 nm. The width of ACIII punctum was as small as 153 ± 27 nm using STED microscopy and 308 ± 38 nm using confocal microscopy averaged over 30 clusters each (Figure 3-6B).

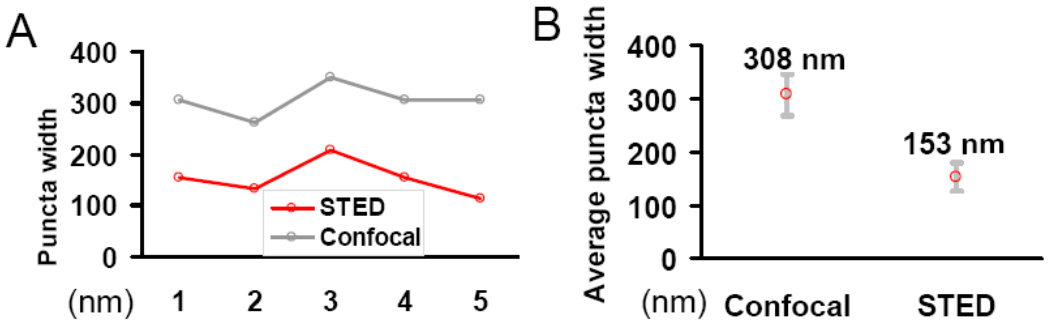

Figure 3-6 Measurement of ACIII puncta. (A) The FWHMs of ACIII clusters 1 to 5. The cluster width estimated from the STED image was as small as 112 nm, far below the diffraction limit. (B) The average FWHMs of ACIII puncta estimated based on STED and confocal microscopy (n = 30). The confocal image overestimated the width for about twofold.

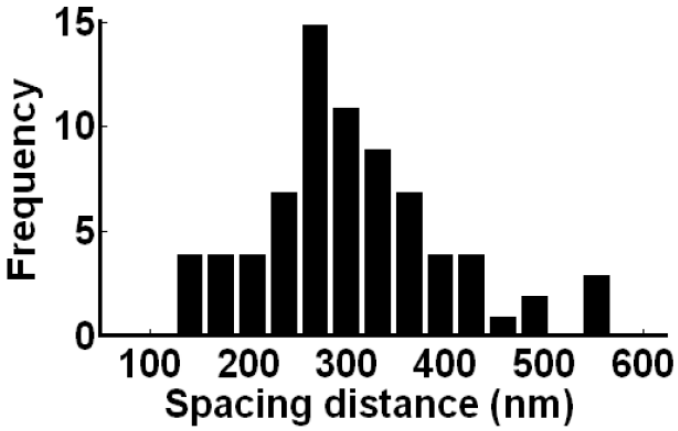

Figure 3-7 The histogram of measured spacing distances between ACIII puncta using STED microscopy (n = 75) revealing a ~300-nm average spacing of ACIII puncta along primary cilia.

We also measured the spacing distances between ACIII puncta. The average spacing of these puncta presented in a histogram in Figure 3-7 was around 300 nm (averaged over 70 pairs of puncta), where some spacing distances below the diffraction limit. Using STED superresolution microscopy, we have found that ACIII formed a particular pattern along the primary cilium with non-random ACIII clusters of an average ~150 nm width. In contrast with the diffraction-limited images showing a continuous ACIII distribution along the cilia, STED images showed that each ACIII cluster localized discretely at a nearly equal distance, or a periodic punctate pattern, in the majority of primary cilia. It remains to be explored what causes this periodic pattern and what functional roles this pattern plays such as in cAMP or other related signaling pathways. One possible mechanism for this distribution pattern is that ACIII could be regulated by other ciliary membrane-bound proteins. For example, the immunostained images in the previous studies displayed a punctum-like localization of Smoothened [94], and Polycystin-1/-2 along a cilium that schematically or experimentally showed a morphological distribution similar to that of ACIII over the ciliary membrane [95-96]. It has also been suggested that monocional antibody CC-248 elicited against a crude suspension of quail oviduct basal bodies forms a periodically helical structure surrounding the cilium axoneme [97-98]. These are possible candidates for correlation with the observed periodic pattern of ACIII. Furthermore, ACIII-enriched primary cilia were mostly found in higher seeding-density cells, for example, up to ~90 % confluence, where ACIII presented both at the basal body and the ciliary compartment, implicating that cell-cell interactions and signaling can be a factor of ACIII expression and distribution in a cilium. It was noted that in some primary cilia (<20% of all primary cilia), ACIII only localized to the basal body, and thus the punctate

pattern along the cilia was absent.

3.3 STED Microscopy Revealed Multiple Distribution Patterns of IFT88 in Primary Cilia of Fibroblasts

3.3.1 Y-shaped and Three-puncta pattern of IFT88 at ciliary base

IFT88 has been known as a core protein of the intraflagellar transport machinery and is required for the formation of all cilia [37]. In order to better localize IFT88 and gain insight into its functional process in primary cilia, we conducted superresolution imaging of immunostained IFT88 (Alexa Fluor 488) in human fibroblasts. Confocal images in Figure 3-8 were similar to Figure 3-2C, indicating relatively bright fluorescence at the basal and distal ends of cilia. STED images showed a much more detailed view of the distribution of IFT88 (Figure 3-8). Clusters of IFT88 along a cilium observed in confocal images could be better distinguished in STED images, which better revealed the localization of a bright punctum of IFT88 to the tip of a cilium. More strikingly, IFT88 formed special and distinct geometric patterns at the base of the cilia in the STED images (Figure 3-8, B, D, F, and H).

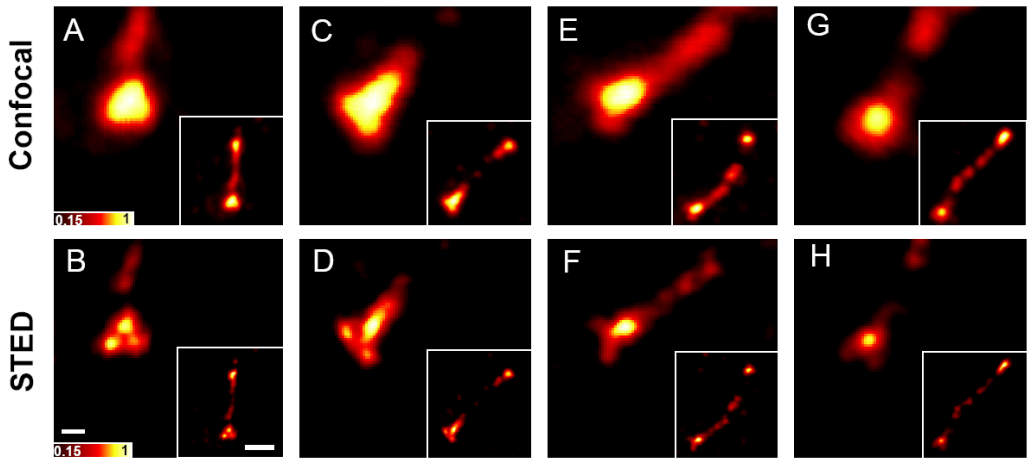

Figure 3-8 STED imaging revealing multiple distribution patterns of IFT88 in primary cilia of human fibroblasts. (A,C,E,G) Confocal images with normalized intensity showing high intensity clusters of immunolabeled IFT88 at the basal end of primary cilia. These images lacked the resolution to properly characterize the structural differences among these clusters. (B,D,F,H) Corresponding STED images with normalized intensity illustrating distinguishable distribution patterns of IFT88. Three puncta were observed in (B) and (D) forming a triangle at the basal end of the primary cilia. These three-puncta patterns could not be resolved by confocal microscopy. A different IFT88 distribution pattern from (B) and (D) was found in (F) and (H), where IFT88 demonstrated a "Y-shaped" pattern where a bright punctum was connected to two branches toward the basal end with an angle to the axoneme direction. Scale bar, 250 nm for main images; 1 um for insets.

For instance, Figure 3-8B and D demonstrate a three-puncta configuration of IFT88 at the base of cilia that was found in ~25% of cells under 48-hour serum deprivation (Figure 3-9). The remaining ~75% of cells possessed primary cilia with a "Y-shaped" pattern of IFT88 at the base of cilia, in which a bright punctum was connected to two branches pointing toward the basal end at an angle relative to the axoneme axis (Figure 3-8F and H). These statistics were obtained by STED imaging of 12 primary cilia on HFFs.

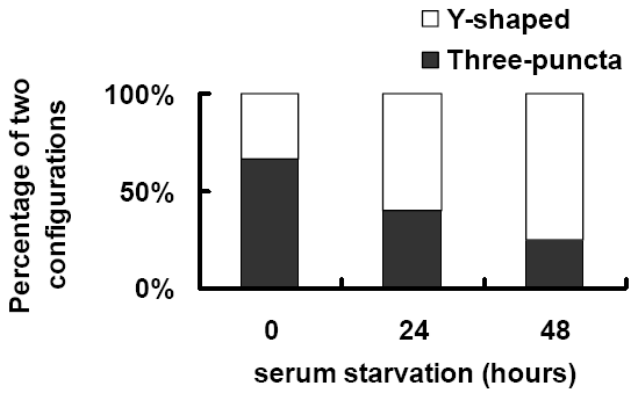

Figure 3-9 STED images of cells under 0, 24, and 48 hours serum deprivation showing the tendency toward Y-shaped configuration with longer serum starvation. The numbers

of cilia evaluated in 0, 24, and 48 hours were 6, 5, and 12, respectively.

3.3.2 Similar patterns of IFT88 localization found in different cell types

To verify the patterns we saw in HFFs, we have further performed the STED imaging for IFT88 in two additional cell types, i.e. mouse inner medullary collecting duct (IMCD) cells (Figure 3-10, A and B) and mouse embryonic fibroblasts (MEFs) (Figure 3-10, D and E), and found the similar three-puncta and Y-shape patterns as in HFFs. These patterns were observed by STED imaging of 20 primary cilia on IMCD cells and 13 primary cilia on MEFs. The findings of similar patterns in different cell types confirmed that these phenomena are not specific for HFFs, but potentially common for primary cilia in general. These patterns were observed from a side-view with a thin Z imaging section, so it was likely that the puncta and Y-shaped patterns were cross-section images of the 3D structure, where the two basal puncta of the three-puncta pattern might reflect the side-view projection of the known ring-shaped distribution of IFT particles. Indeed, in IMCD cells, some primary cilia grew vertically from the glass surface, and we did see a ring-shaped pattern (Figure 3-10C).

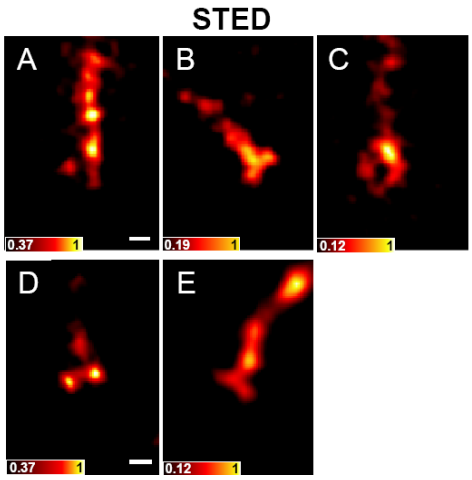

Figure 3-10 IFT88 patterns in mouse cell lines. (A) and (B) 20 images were collected and showed similar three puncta (A) and Y-shaped (B) pattern in IMCD cells using STED microscopy. (C) A primary cilium that grew vertically showed a ring-shaped pattern. (D) and (E) Similar three puncta (D) and Y-shaped (E) pattern were found in MEFs with STED microscopy. 13 primary cilia were imaged, revealing the two types of distribution. Scale bar, 250 nm.

3.3.3 Dimension analysis of two distinct IFT88 configurations

To our knowledge, these distinct distribution patterns of IFT88 have never been reported due to the diffraction limit of conventional microscopy. To investigate the population of three-puncta and Y-shpaed case under serum starvation, STED images over the cells under 0, 24, and 48 hours serum deprivation were captured. We then counted the numbers of two configurations and measured the length of each cilium to obtain the average characteristic length. The population percentages of the two cases at each starvation condition were then obtained. Our results revealed that the percentage of cells with the three-puncta pattern increased with a shorter serum starvation time when comparing the results of 0-hr, 24-hr, and 48-hr serum deprivations (Figure 3-9). The

population percentages shown in Figure 3-9 were evaluated in 0, 24, and 48 hours based on 6, 5, and 12 primary cilia, respectively. We further analyzed the geometry of the "three-puncta" and "Y-shaped" patterns, with the characteristic lengths defined in the coordinate corresponding to the orientation of the axoneme. We measured the characteristic lengths of the configuration, including d, the distance between two puncta at the basal end of the three-puncta pattern or two branch ends of the Y-shaped pattern; h, the height between the junction point in the Y-shaped pattern and the virtual plane of the ends of two branches; and H, the height of triangles formed by three-puncta or Y-shaped configurations (Figure 3-11A). Figure 3-11B shows the models of the two patterns and their characteristic lengths.

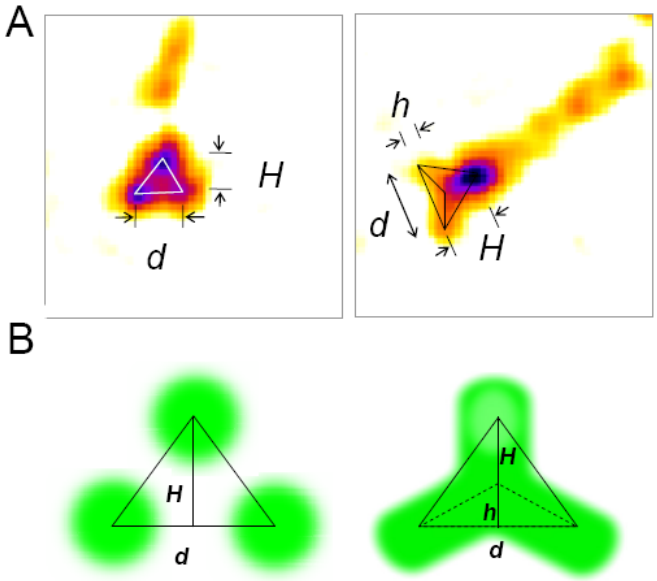

Figure 3-11 Illustration of characteristic lengths in both patterns. (A) The characteristic length d was defined as the distance between two basal puncta of the three-puncta (left) or between two branching ends of the Y-shaped pattern (right); h, the height of inner triangle marked in Y-shaped cases; and H, the height of triangles formed by three-puncta or Y-shaped configurations. (B) Schematic diagrams of the definition of lengths for

three-puncta and Y-shaped patterns.

Our statistical analyses showed that the height of triangles in the three-puncta pattern was around 200 nm on average under different serum starvation conditions (Figure 3-12A). For the Y-shaped pattern, the average height of the triangle was slightly greater than the average height of the three-puncta pattern. The average height h from the junction point was about 100 nm less than H (Figure 3-12B). The average distance d was 298 nm between two basal puncta of the three puncta pattern and was 304 nm between two branch ends of the Y-shaped pattern. The difference between H and h in the Y-shaped model implied that IFT88 accumulated at the site 100 nm above the connection point. 23 images were analyzed to determine the average dimension of the two patterns at the base of primary cilia shown in Figure 3-12A and B. In addition, the difference between the three-puncta and the Y-shaped patterns potentially imply possible transport behaviors of IFT88, although the detailed mechanism remains to be explored.

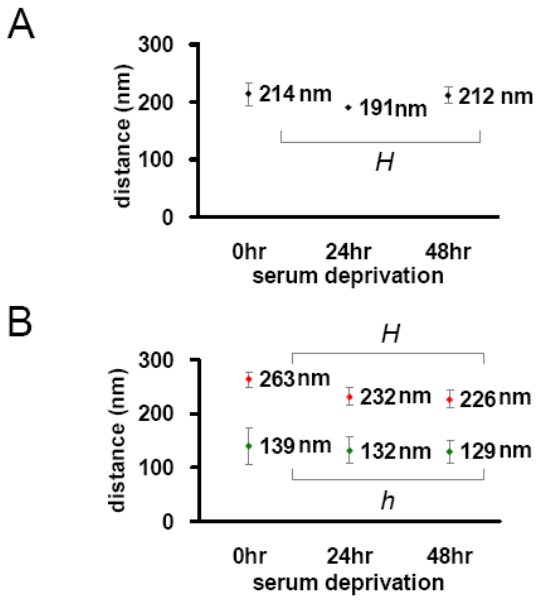

Figure 3-12 (A) Statistical analysis showing the average height of triangles was ~200

nm in the three-puncta pattern under different serum-deprived conditions. (B) In the Y-shaped pattern, the average height H was slightly greater than three-puncta pattern while the average height h was ~130 nm, approximately 100 nm shorter than H. 9 images were analyzed for Figure A and 14 images were analyzed for Figure B.

3.4 Discussion

In contrast to the periodic distribution pattern of ACIII, the superresolution images of IFT88 in primary cilia of human fibroblasts revealed a distinct localization in the vicinity of the base of cilia. The detailed patterns revealed by STED microscopy extended the previous observation of triangular distribution of IFT88 at the basal end [99-101]. These two situations implied that IFT88 resides at the base with special patterns of non-uniform localization, which could not be previously resolved by a conventional microscope.

IFT88 was mostly found to aggregate at the top punctum of the Y-shaped pattern under a 48-hour serum-deprived condition. In addition, the characteristic lengths of the triangle defined in accordance with the three puncta or the branches of the Y-shaped pattern were nearly conserved under different serum conditions. This observation suggested that the basal structure foundation of primary cilia did not change dramatically under different serum starvation conditions. The two different configurations of IFT88 may be caused by different environments near the cells, different states during the cell cycle, or merely an imaging angle difference, although we have conducted z-stack imaging to rule out imaging issues as the main reason for this observation. The similar triangular settings of the three-puncta pattern and the Y-shaped pattern of IFT88 implied that these patterns were related, potentially correlating with different transport activities in primary cilia.

The numerous studies on primary cilia and their physiological and pathological roles have mainly been performed using far-field optical microscopes due to its accessibility and its ease of operation. Before the emergence of superresolution imaging, the features of ciliary activity were only observed at a diffraction-limited resolution, limiting the understanding and characterization of ciliary structure and dynamics. While electron microscopy provides a high resolution for these analyses, its restricted operation conditions and shortage of labeling flexibility considerably hinders its applications such as structural characterization in different states or dynamic studies in live cells. Recent advances in superresolution techniques have provided important tools to address questions involving dimensions on the scale of subdiffraction and enabled new scientific discoveries. In the application of primary cilia, the localization of centrosomal proteins was reported using PALM/STORM microscopy [102]. STED microscopy is one of the most promising superresolution techniques, because in addition to its physics-based >4-fold resolution improvement, STED microscopy provides a promising acquisition speed for studying the dynamics of ciliary proteins or other biological problems. Unlike electron microscopes, STED does not require a vacuum in which to operate, enabling superresolution live-cell imaging in an unperturbed environment. Our work demonstrates that STED microscopy could facilitate new findings in primary cilia research, such as our identification of two distinct molecular distributions of IFT88 and special localization patterns of ACIII.

3.5 Materials and Methods

3.5.1 Cell Culture

Human newborn foreskin fibroblasts (HFF-1, ATCC, SCRC-1041) were cultured on #1.5 cover glasses in dishes in DMEM supplemented with 15% FBS, 1.5% HEPES, 1.2% Pen-Strep and 1.2% 2mM L-glutamine at 37°C and 5% CO_2, and incubated in serum-enriched media or serum-deprived media for 24 or 48 hours after reaching ~80% confluence. Mouse inner medullary collecting duct (IMCD) cells and mouse embryonic fibroblasts (MEFs) were cultured in DMEM with 10% FBS, 1.5% HEPES, 1.2% Pen-strep at 37°C and 5% CO_2. To induce the ciliogenesis, IMCD cells and MEFs were cultured in DMEM with 0.1% FBS for 48-72 hours.

3.5.2 Immunostaining

The cells were perfusion-fixed with 4% paraformaldehyde for 12 minutes and then washed twice with PBS. After permeabilized with 0.2% PBST (PBS + Triton-X) and blocking with 10% normal donkey serum for one hour at room temperature, cells were incubated with primary antibodies for ACIII (anti-ACIII rabbit IgG, sc-588, lot #E1311, Santa Cruz, used at 1:200), IFT88 (anti-IFT88 rabbit IgG, 13967-1-AP, Proteintech, used at 1:200), and/or ac-tub (anti-acetylated α-tubulin mouse IgG, ab24610, lot #GR14296-11, clone # 6-11B-1, Abcam, used at 1:1500), Pericentrin (anti-Pericentrin rabbit IgG, ab4448, Abcam, used at 1:2000) diluted in 10% normal serum at 4°C overnight. Cover glasses were then washed in PBST three times, incubated with secondary antibodies (donkey anti-rabbit Alexa Fluor 488 or donkey anti-mouse Alexa Fluor 568, Invitrogen, at 1:2000) for one hour at room temperature, and washed again in PBST.

3.5.3 STED Microscopy

In this study, single-color CW STED setup was used to image Oregon Green 488 or Alexa Fluor 488-labeled ACIII or IFT88 protein. The fluorescence emission window was detected via a 535/22 band-pass filter and then an APD single photon counting module The laser powers used for STED imaging were ~2-5 μW for 491-nm excitation beam and ~100 mW for 592-nm depletion beam, measured in the back aperture of the objective lens. All images were recorded point-wise with a pixel size of 25 nm and dwell time of 20 μs by a stage scanner. Quantitative measurement of the resolution and line profiles of the confocal and STED images was based on untreated images which were analyzed with the use of ImageJ. Confocal Images illustrated in Figures were processed by a mean filter of 1 pixel and contrast stretching; images for STED were contrast-enhanced with generalized Tikhonov regularization [103] and contrast stretching.

4 Architectural Mapping of the Ciliary Transition Zone Using STED Microscopy

4.1 Optimization of STED imaging for ciliary proteins

Different from conventional fluorescent microscopy, serious care has to be taken to address multiple sample-specific issues of superresolution STED imaging. For imaging proteins in or close to the TZ, the primary issues were: (1) fluorescent signals were markedly dim from some TZ proteins because of limited copies at the site; (2) the depletion phenomenon of STED further reduced the light being detected from the readily dim signals (Figure 4-1A); (3) the high power of the depletion laser accelerated photobleaching/photodamage of our fluorophores; (4) the specific patterns of interest depended highly on the precision of the focal plane (Figure 4-1B and C); and (5) the combination of fluorophores for two-color STED imaging had crosstalks or signal leakages between two channels.

Several tasks of image acquisition and postprocessing were performed to address issues of dim signals caused by inherent properties of fluorophores, the depletion effect, photobleaching, or photodamage. Because the weak signal of TZ proteins, the excitation laser had to be optimized, as a result, we used a power at 0.3-1.5 μW. The power of the CW depletion laser was adjusted accordingly, with the additional consideration of signal loss when depleting strongly. We used a moderate power of the depletion laser at 60-100 mW at the back aperture with compromised resolution but detectable signal levels. The pixel dwell time was set to ~20 μs, fast enough to minimize photobleaching/photodamage and the sampling step size was set to 25 nm to maximize the signal-to-noise ratio. After subdiffraction images were acquired, we performed different tasks for data analysis and

image display. For data analysis to obtain quantitative measures, raw data was processed with mean filtering (see Methods). For image display in figures, we performed deconvolution to enhance the dim signals and thresholding to contrast the signals of interest from the background signals. To find the focus at a high precision, samples were scanned consecutively in the z direction every 100 nm to assure the proteins could be imaged with meaningful quantitative measures.

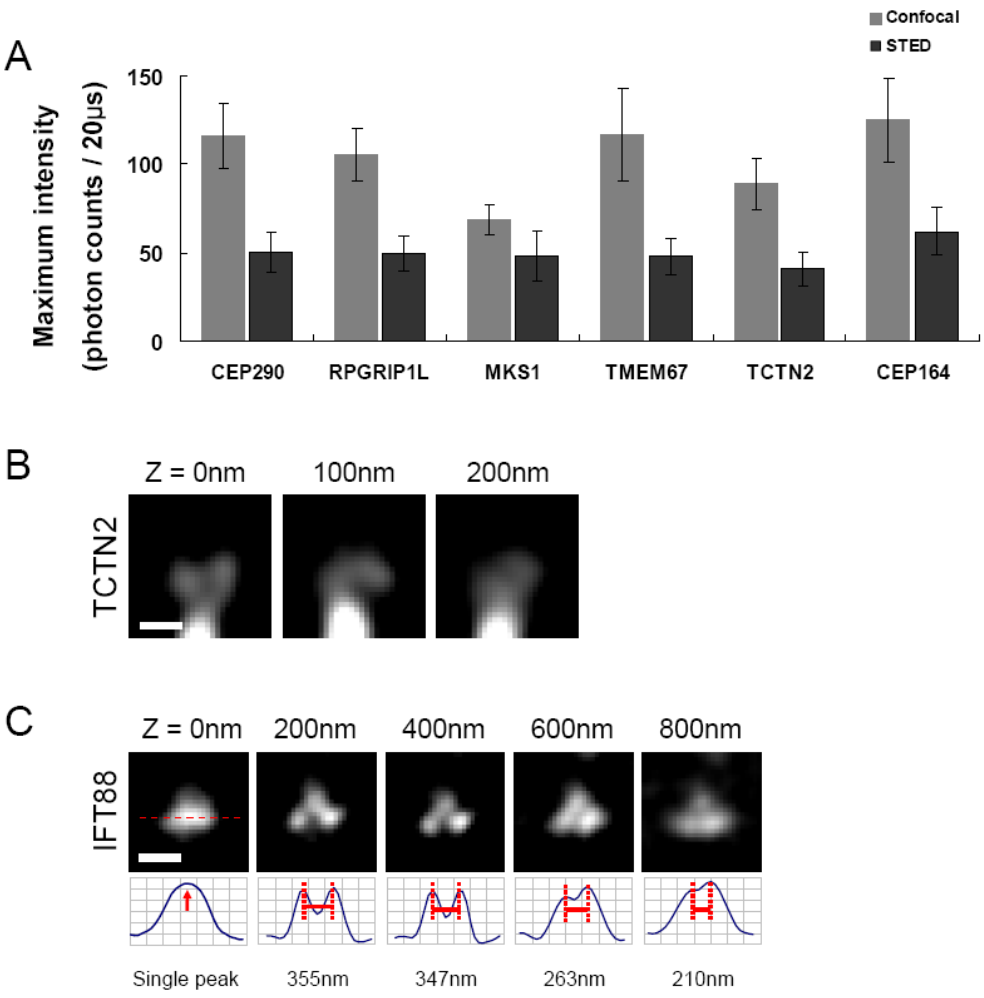

Figure 4-1 Challenges of STED imaging. (A) Intensity comparison of confocal and STED microscopy for TZ/TF proteins revealed that the STED imaging signal drops by ~30-60% due to depletion. The Y-axis reports the photon counts collected every 20 μs.

Different excitation and depletion laser powers were used for different TZ/TF proteins to reach a comparable and detectable level of photon counts in the STED images. (B) A change of 100 nm in the focal plane affected the observed distribution pattern of TCTN2. (C) The lateral distance of the proximal puncta of IFT88 strongly depended on the focal plane. At z = 0 nm, no separate puncta were observed; at z = 200~400 nm, the distance between the two intensity peaks reached a maximum, better representing the real size of a ring. Scale bar: 200 nm for (B) and 400 nm for (C).

Dual-color STED imaging of our system was achieved by two excitation lasers at 447 nm and 491 nm and one depletion laser at 592 nm, with two excitation-separable fluorescent dyes BD V500 and Oregon Green 488, or with one organic dye BD V500 and one fluorescent protein eGFP. We noted that the signal crosstalks leaking from the Oregon Green 488/eGFP channel to the BD V500 channel were more serious and designed the experiments accordingly (see below). In most cases, a combination fixation protocol, for example, paraformaldehyde (PFA) and methanol was used for two antibodies in the two channels to optimize the signal-to-noise ratio independently. Concentrations of primary antibodies, critical for STED imaging, were experimentally optimized for each protein of interest [104]. Relative concentrations of secondary antibodies were adjusted to avoid excessive crosstalk between the two channels in dual-color images.

Human retinal pigment epithelial cells (RPE-1) were chosen for these studies as they frequently have primary cilia aligned in parallel to the imaging plane (Figure 4-2), allowing simultaneous mapping of proteins at the ciliary base in both radial and axial directions. Selected components known to associate with the three major multiprotein complexes of the TZ were imaged, including CEP290, RPGRIP1L, MKS1, and TMEM67. In addition, CEP164, a component of the transition fiber (TF) known to mediate the

anchorage of basal bodies to the plasma membrane, was examined to establish the proximal end of the TZ.

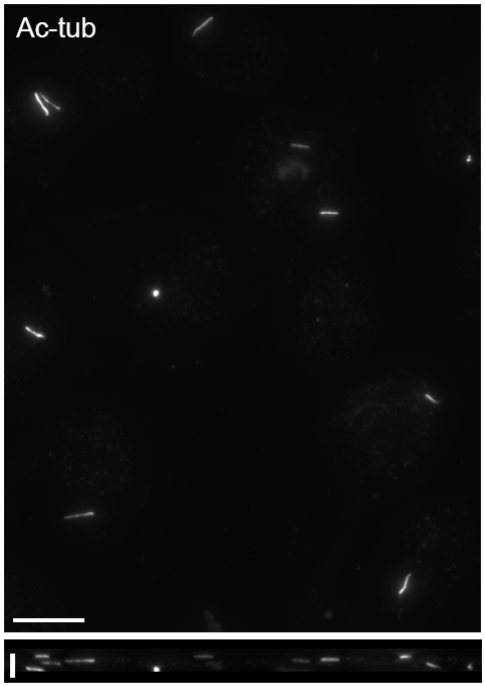

Figure 4-2 Horizontal primary cilia found in RPE-1 cells. (Upper) A stacked image of snapshots at different focal planes. (Lower) A side-view of the 3D stacked image revealed that most of the cilia were oriented horizontally to the culture surface. Z step: 200 nm. Scale bars: 10 μm.

4.2 STED images reveal distinct lateral localization patterns of TZ/TF proteins at the ciliary base

4.2.1 TZ/TF proteins under subdiffraction imaging

Due to the presumably cylindrical-like symmetry of TZ and TF proteins, one could use two parameters alone, i.e. radial and axial locations, to describe the positions of these

proteins. Thus, we chose to use human retinal pigment epithelial (RPE) cells whose primary cilia orient their axoneme in the direction parallel to the imaging plane, such that a side-view showing the radial and axial positions of proteins in primary cilia could be seen (Figure 4-3A). Epifluorescent imaging of RPE cells showed that TZ proteins are localized between the axoneme (acetylated α-tubulin labeled) and the BB (Centrin labeled) seen merely as a single dot (Figure 4-3B). We thus performed superresolution STED imaging from a side view and showed resolution improvement when comparing confocal and STED images of TZ proteins such as TCTN2 Figure 4-3C) and TMEM67 (Figure 4-3D). Confocal images showed an intensity cluster as in the epifluorescent images, while the significant resolution enhancement by STED microscopy illustrated two separate intensity peaks of TMEM67 and TCTN2, presumably signals from the projection of a ring-shaped protein distribution at a shallow focal plane. Since the off-focus fluorescence from other part of a ring was also excited and detectable, the faint signals between these two intensity peaks were seen in the STED images.

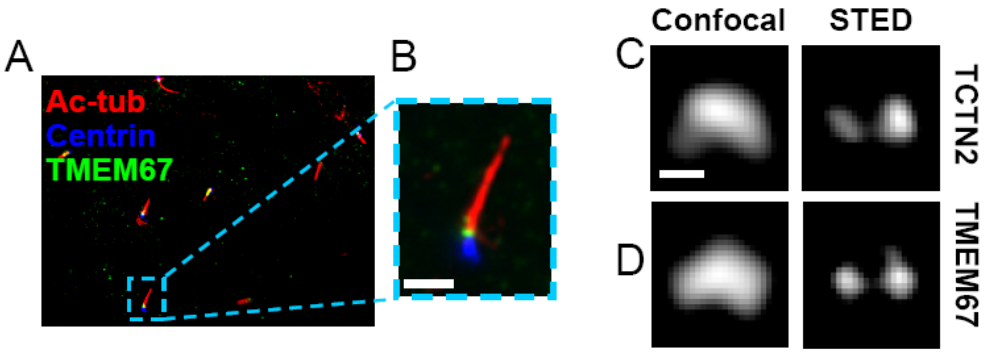

Figure 4-3 Subdiffraction STED images revealing distinct lateral localization patterns of TZ/TF proteins at the base of primary cilia in RPE-1 cells. (A, B) An epifluorescence image of RPE-1 cells showing the TZ protein TMEM67 (green) sandwiched between centrin-eGFP (blue) and acetylated tubulin (red). Scale bar: 2 μm. (C, D) Comparison of

confocal and STED images of TCTN2 and TMEM67 illustrating the ability of STED to resolve two separate intensity peaks, potentially from the projected signals of a ring-shaped protein distribution recorded from a narrow focal plane.

A series of TZ proteins including CEP290, RPGRIP1L, MKS1, TMEM67, and TCTN2, as well as a TF protein CEP164, were imaged with STED (Figure 4-4, A-F). Note that both CEP290 and RPGRIP1L formed an elliptical-like or square-like shape (Figure 4-4, A and B), although some RPGRIP1L images showed two intensity peaks (the middle panel of Figure 4-4B), possibly representing two edges of a ring cross section. The relative intensity between the middle and the left/right ends was less significant than the ones in TMEM67 and TCTN2, potentially due to a higher effect of the off-focus excitation of a small-sized ring. With the resolution of our system, we have not been able to see any separate intensity peaks for CEP290 (Figure 4-4A), so we were not certain whether CEP290 formed a disk-shaped accumulation or a ring-shaped pattern with a small diameter.

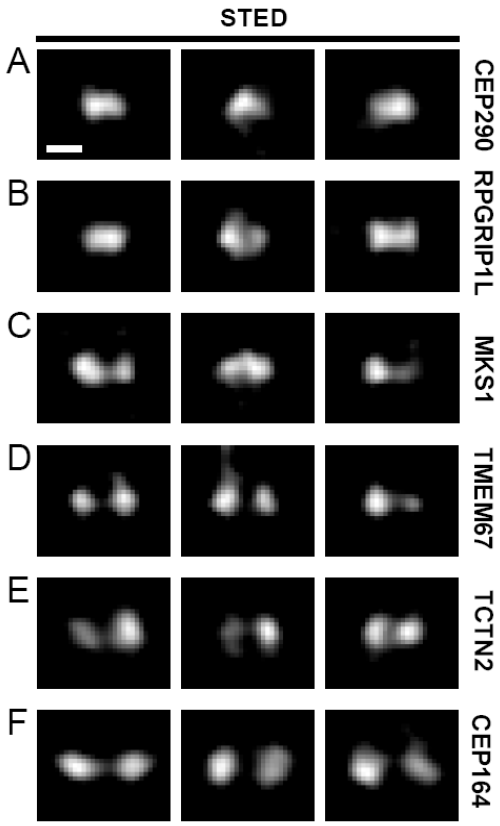

Figure 4-4 STED imaging revealed distinct lateral localization patterns of TZ/TF proteins (A-F) A set of STED images showing distinct lateral dimensions of TZ and TF proteins. CEP290 and RPGRIP1L had narrow widths, while MKS1, TMEM67, TCTN2, and CEP164 had separable intensity peaks in the order of increasing width. Scale bar, 200 nm.

Subdiffraction images of MKS1 (Figure 4-4C), TMEM67 (Figure 4-4D) and TCTN2 (Figure 4-4E) showed that they occupied a wider area than CEP290 and RPGRIP1L with two clearly separate intensity peaks, indicating that they were localized toward the outer periphery of the TZ. Notice that in some of the TMEM67 images (left and middle panels of Figure 4-4D), branches pointing toward the ciliary compartment from one or both of the intensity peaks were present, implying TMEM67 could be localized toward the distal end of the TZ. CEP164 is known to be localized to the TFs, which formed a ring outside of the

distal end of the BB presumably with a diameter larger than that of the ciliary membrane. The subdiffraction images of CEP164 (Figure 4-4F) indeed showed a wider lateral occupation than any TZ protein examined in this study, marking the junction of the plasma membrane and ciliary membrane [14].

4.2.2 Quantitative analysis of TZ/TF protein distribution

To know the size of the region each of these TZ/TF proteins occupied, raw data was analyzed to obtain the full widths at half maximum (FWHMs) in both the lateral and axial directions (Figure 4-5, A-L). For CEP290 and RPGRIP1L, images were fitted with a two-dimensional Gaussian function (Figure 4-5, M and N) to identify the principal axes and to find the FWHMs (Figure 4-5A, B, G, and H). The fitting curves agreed well with the data, except some RPGRIP1L images had a slight intensity dip in the middle as stated above. For MKS1, TMEM67, TCTN2, and CEP164, STED images clearly displayed two distinct peaks in the lateral direction, so the lateral FWHMs were determined based on the maximum between both peaks (Figure 4-5, C-F and I-L). Although the value of the lateral FWHM, or the lateral width, might not directly correspond to physical dimensions of these TZ/TF proteins, it served as a measure for comparing their locations. The average axial widths, representing the axial ranges occupied by these TZ/TF proteins, were compared in Figure 4-6A. All axial widths of these TZ/TF proteins were about 200 nm with small differences among them. On the other hand, the differences of widths in the lateral direction were significant, revealing that TZ components occupy different regions of the TZ, with CEP290 and RPGRIP1L being the narrowest, TMEM67 and TCTN2 being the widest, and MKS1 being intermediate in width (Figure 4-6B, Table 4-1).

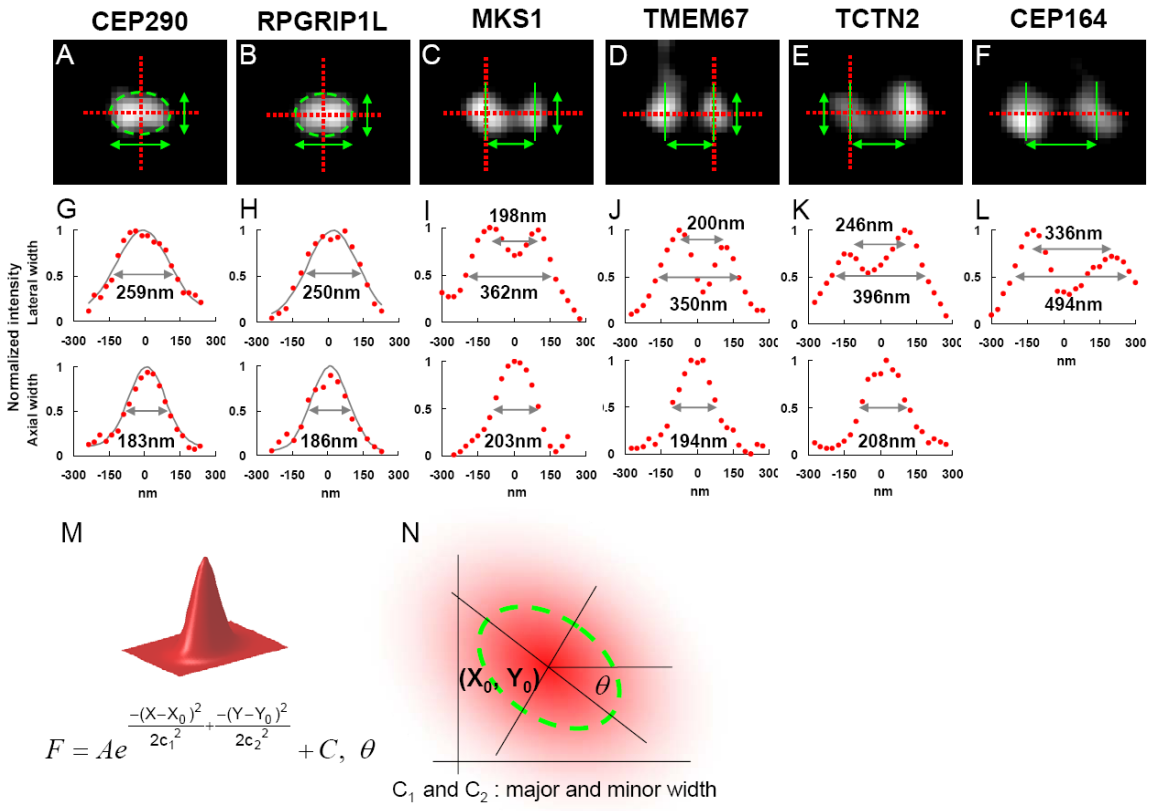

Figure 4-5 Measurement of lateral and axial widths for CEP290, RPGRIP1L, MKS1, TMEM67, TCTN2, and CEP164. (A-F) STED images were measured in lateral (red horizontal line) and axial (red vertical line) directions of the TZ. For CEP290 (A) and RPGRIP1L (B), the data was fitted with a 2D Gaussian function. The green dashed lines show the fitted shape. (C-F) STED images were directly measured along the principal directions. (G-L) Normalized lateral and axial intensity profiles extracted from images (A-F) along red lines. The peak-to-peak distance was obtained to illustrate the lateral diameter of a ring. (M, N) A rotational 2D Gaussian function was used to determine the width. The FWHMs were obtained by multiplying the coefficients c1 and c2 by the factor $2\sqrt{2\ln 2}$.

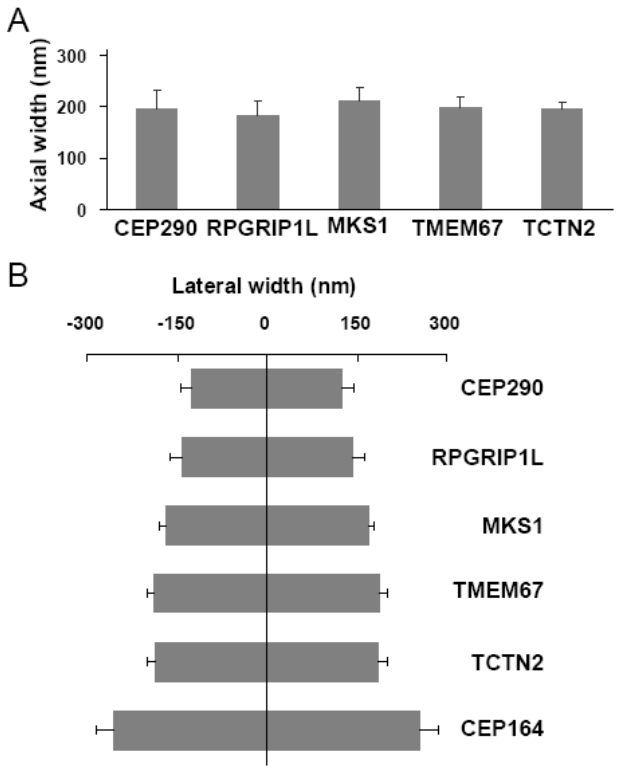

Figure 4-6 Statistical analyses of axial and lateral widths (mean ± standard deviation). (A, B) These TZ proteins all had their axial widths of about 200 nm, while their lateral widths were significantly different.

Table 4-1 Quantitative analysis of protein localization

protein \ nm (N)	Lateral width	Axial width	Lateral diameter	Axial distance to Centrin	Axial distance to TCTN2
CEP290	265±19 (7)	213±36 (7)	-	42±16 (7)	-
RPGRIP1L	284±40 (7)	183±30 (7)	165±8 (5)	143±27 (13)	-
MKS1	335±24 (8)	213±26 (8)	186±21 (7)	150±12 (5)	-
TMEM67	374±30 (10)	199±20 (10)	205±20 (21)	143±15 (8)	-
TCTN2	371±29 (8)	197±11 (8)	227±18 (17)	153±13 (7)	-
CEP164	507±61 (15)	-	373±35 (14)	-38±21 (9)	-
IFT88 (proximal)	-	-	356±24 (26)	-	188±25 (10)
IFT88 (distal)	-	-	162±11 (3)	-	126±30 (7)

4.3 Dual-color STED imaging reveals novel axial localization of TZ/TF/IFT proteins

4.3.1 Axial localization of TZ/TF proteins

To determine the relative axial positions of TZ/TF proteins, we conducted dual-color STED imaging together with a reference ciliary marker adjacent to the TZ. Comparing ciliary markers including ac-tub, adenylyl cyclase III, and centrin of the BB, we found that centrin was the most suitable as a reference coordinate because of its consistent localization at the distal end of the BB and its position distant from the TZ, avoiding the confusion from crosstalks. The orientation of centrin in the BB also served to set the axial orientation of the TZ.

An RPE cell line with stably expressed eGFP-Centrin [105] was stained with one TZ/TF protein at a time. eGFP was excited with a 491 nm beam, while CEP290,

RPGRIP1L, MKS1, TMEM67, TCTN2, or CEP164 was labeled with BD V500 fluorophore excited with a 447-nm light. Since eGFP was also partially excitable at 447 nm, Centrin could be detected in both channels. One advantage of this dye combination was the easy alignment of two sequential acquisitions of STED images at different colors by correlating the Centrin location. To define the reference coordinate in the axial direction, the distal edge of Centrin was located by pinpointing the position of the FWHM of the fluorescent intensity along the primary axis of Centrin (Figure 4-7, A-F).

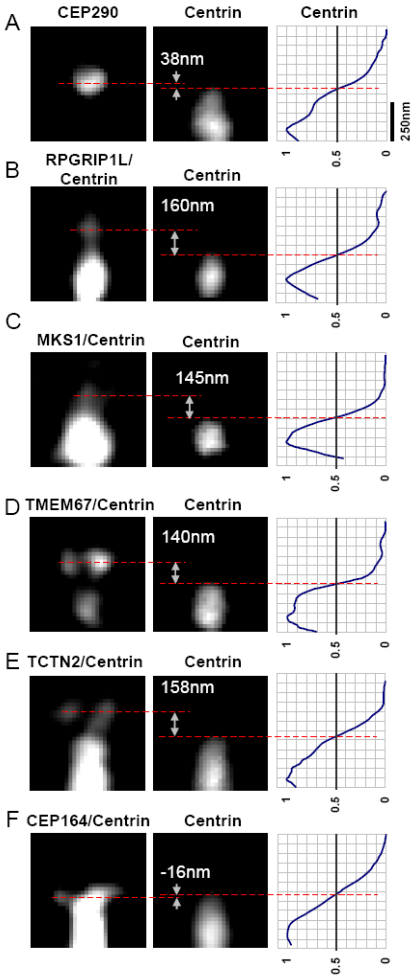

Figure 4-7 The distal edge of centrin is defined as the position where the intensity coincides with the value of the FWHM. (A-F) The distal edge of centrin was first

determined by pinpointing the position of the FWHM of signals in each case (right panels). Axial positions of CEP290, RPGRIP1L, MKS1, TMEM67, TCTN2, and CEP164 (left panels) were determined by measuring the distances from the peak intensities of TZ/TF proteins to the locations of the distal edge of centrin (middle panels).

Axial positions of the peak intensities of CEP290, RPGRIP1L, MKS1, TMEM67, TCTN2, and CEP164 were then determined relative to the distal edge of Centrin (Figure 4-8, A to F). Although signals of some TZ proteins such as RPGRIP1L, MKS1, and TCTN2 were dimmer than the signal of Centrin leaking into the channel (Figure 4-8, B, D, and E), one could assume that only the isolated signals at the distal side were from the corresponding TZ proteins and ignore the signals at the location of Centrin. In order to see the target proteins more clearly, the intensity for part of the images within the gray box was increased by 30-150% in Figure 4-8B, C, E, and F without affecting the distance measurement. Note that the visual artifact of the size difference of RPGRIP1L in Figure 4-8B and Figure 4-4B was primarily caused by the intensity threshold to show more of the bright object, where the measured FWHMs of these two figures were very similar and the axial distance was not affected by its visual size. Aligning the distal edge of Centrin, a set of side-by-side dual-color STED images were shown in Figure 4-8G to L, in which Centrin was displayed in yellow and each of the target proteins was shown in green. As a whole, RPGRIP1L, MKS1, TMEM67, and TCTN2 were axially localized at the farthest distance from Centrin. Surprisingly, CEP290 was axially localized between Centrin and other TZ proteins. The intensity peak of the TF protein CEP164 was localized at the proximal side of the Centrin's distal edge.

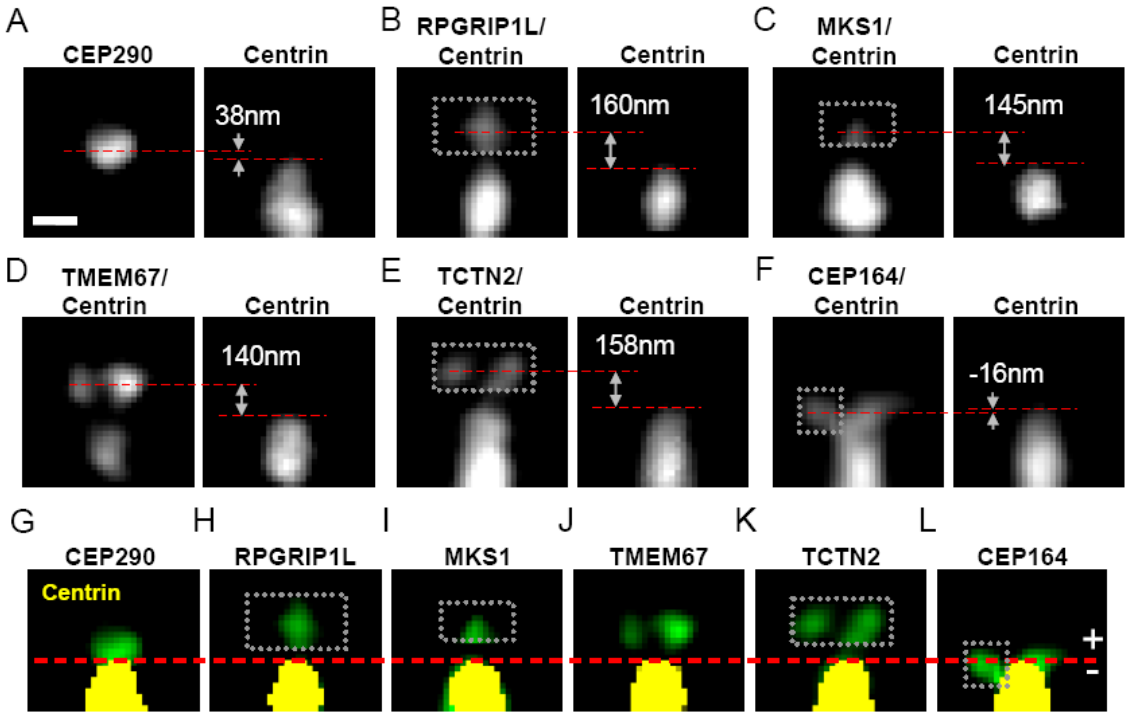

Figure 4-8 Dual-color STED images revealing distinct axial localization levels of different TZ and TF proteins. (A-F) Sample dual-color STED images showing different axial positions relative to the distal edge of centrin for different TZ/TF proteins. The axial distance of each BD V500-labeled TZ/TF protein to the FWHM-defined boundary of centrin-eGFP was measured. (G-L) Comparison of the axial positions of TZ/TF proteins (green) relative to centrin (yellow) revealing that RPGRIP1L, MKS1, TMEM67, and TCTN2 were at a similar distance from centrin (red dashed line), while CEP290 was at another axial level close to centrin, distinct from other TZ proteins. CEP164 was slightly proximal to the distal edge of centrin. Scale bar for (A-L): 200 nm.

4.3.2 IFT88 is colocalized with the transition fibers and distributed across the TZ/TF

With the structural framework of the ciliary base, we further examined the localization of functional proteins, i.e. IFT proteins, in this framework. As we previously reported in other cell lines [106], we found two distinct distribution patterns, i.e. three-puncta

(Figure 4-9A) and Y-shaped (Figure 4-9B) patterns, of IFT88 at the ciliary base in RPE cells as well. We also found two separate intensity peaks at the distal punctum in some cases, suggesting IFT88 could potentially form a ring in this region (Figure 4-9C). With dual-color STED imaging, we were able to determine where these patterns were located relative to the TZ by co-labeling IFT88 and TCTN2 and optimizing the balance of fluorescence intensities. Figure 4-9D shows that the proximal and distal puncta of a three-puncta pattern of IFT88 sandwiched TCTN2 in the axial direction.

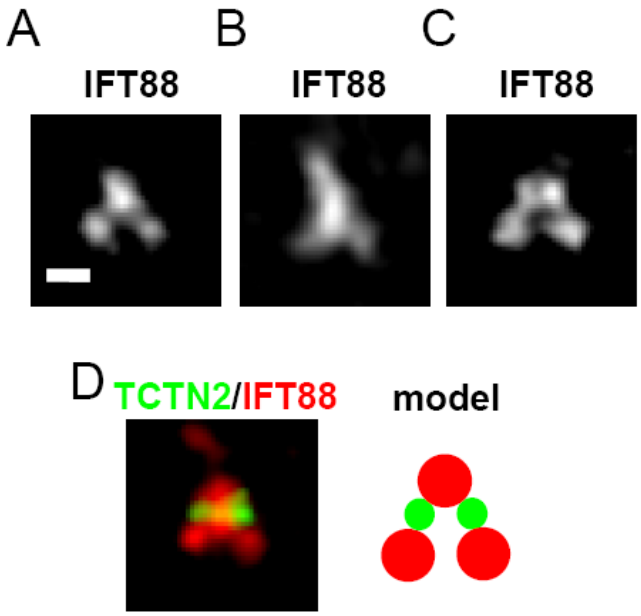

Figure 4-9 Dual-color STED imaging showed IFT88 location relative to TZ protein. (A, B) Two distinct patterns (three puncta and Y-shaped) of IFT88 in RPE-1 cells. (C) An example image showing separate intensity peaks of IFT88 for the distal punctum, suggesting a possible ring-shaped distribution at this location. (D) A dual-color STED image and a proposed model of TCTN2 and IFT88 showing that TCTN2 was axially localized between the distal and proximal puncta. Scale bar for (A-D): 250nm.

The average axial distance from the proximal puncta to TCTN2 was 188±25 nm, and the distance from the distal punctum to TCTN2 was 126±30 nm as reported in Table 4-1.

The Y-shaped pattern had the distal punctum at a location similar to the distal punctum of the three-puncta pattern, while the two branches were localized in the proximal side of the TZ. Distributions of IFT88 were then mapped to the Centrin-base coordinate. The axial positions of IFT88 and other TZ/TF proteins are shown in Figure 4-10, where the distribution of distal puncta of IFT88 was spread over a long range from the TZ toward the ciliary compartment, while the IFT88 distribution at the proximal end was aligned with the axial position of the TF protein CEP164.

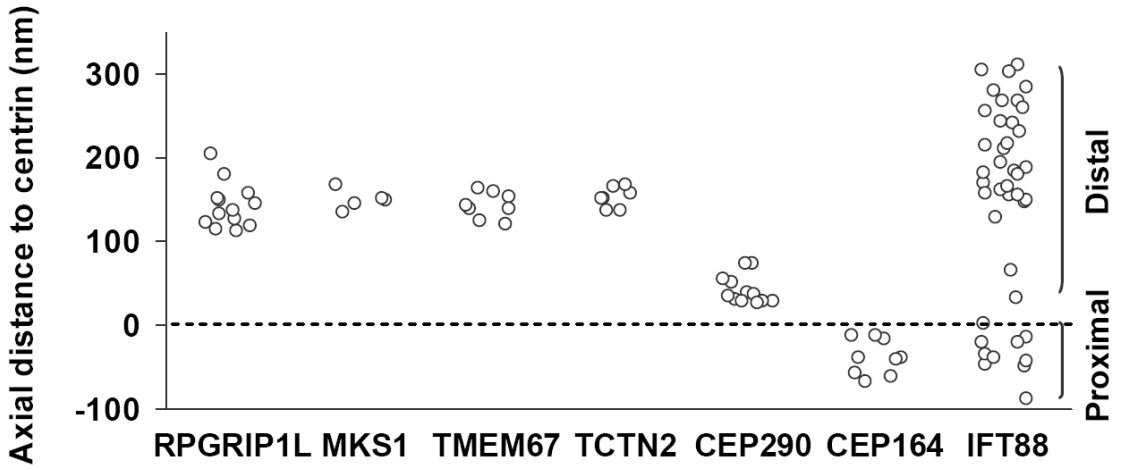

Figure 4-10 Comparison of the axial distances to centrin. RPGRIP1L, MKS1, TMEM67, and TCTN2 were ~150 nm from the centrin tip, while CEP290 was ~40 nm from the centrin tip. IFT88 was localized at two levels, one at the TF and the other distributed 150-300 nm from the centrin tip, covering the TZ and its distal side toward the ciliary compartment.

Peak-to-peak distances in the lateral direction were analyzed for the proximal and distal distributions of IFT88 as well as other TZ/TF proteins, potentially representing diameters for rings of different proteins (Figure 4-11). IFT88 at the proximal end (the group with larger values) had an average diameter of 356±24 nm, similar to the average

diameter of CEP164 at 373±35 nm. Combining the coincidence in both axial and lateral directions, we found the distal puncta of IFT88 and the TF protein CEP164 colocalized with each other up to our resolution limit. Some samples of IFT88 where two separate intensity peaks could be observed at the distal end (Figure 4-9C) showed smaller values in Figure 4-11, with an average diameter of 162±11 nm, similar to the average diameter of RPGRIP1L at 165±8 nm. The average diameter of TMEM67 was 205±20 nm, ~40 nm larger than that of RPGRIP1L, and the average diameter of TCTN2 was 227±18 nm, ~20 nm larger than that of TMEM67. MKS1 was resided between RPGRIP1L and TMEM67 with an average diameter of 186±21 nm (see Table 4-1).

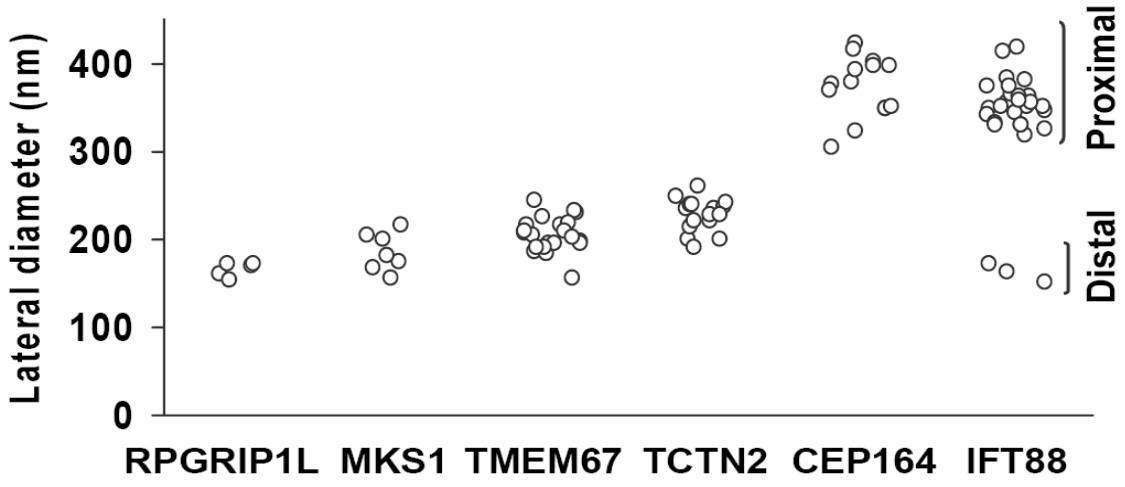

Figure 4-11 Comparison of lateral diameters. RPGRIP1L and the distal punctum of IFT88 were ~160 nm in diameter, indicating they were localized closely to the axoneme. The diameter of MKS1 was ~180 nm, slightly larger than that of RPGRIP1L. TCTN2 and TMEM67 were found mostly in the diameter region of 200 to 250 nm, close to the ciliary membrane. The similar diameters of CEP164 and proximal puncta of IFT88 suggested that IFT88 was localized to TFs.

4.4 A molecular architecture at the ciliary base obtained by overlapping STED results of TZ/TF/IFT88 proteins and an EM image

4.4.1 Architecture of the TZ and TF

Knowing the mean positions of TZ/TF proteins relative to the distal edge of centrin, we overlapped subdiffraction images of individual proteins from single-color STED microscopy (single-color images were used to avoid crosstalks) positioned at their own mean positions and created a multicolor superresolution image illustrating the molecular architecture at the ciliary base (Figure 4-12A; Figure 4-13A and D). This 7-color superresolution image in Figure 4-12A includes components from the TZ (CEP290-magenta, RPGRIP1L-red, MKS1-green, TMEM67-orange, TCTN2-yellow), the TF (CEP164-cyan), and the BB (Centrin-blue). To know the corresponding locations of these proteins on the structure of a primary cilium, we obtained EM images of the side view of primary cilia in RPE cells, as the one shown in Figure 4-12B and Figure 4-13B and E. Although the EM images did not come from the same cells as those of the STED images, the dimensions of the ciliary structure were similar among different EM images, allowing us to use one as a structural reference. Because it was known that CEP164 is localized to the TF, we were able to align the EM image with the multicolor STED image by placing the intensity peaks of CEP164 of the superresolution image at the positions of the two TFs of the EM image (Figure 4-12C; Figure 4-13C and F), marking the overlapping points with "●". Microtubule doublets of the axoneme were marked as "△" and the ciliary membranes were marked as "○".

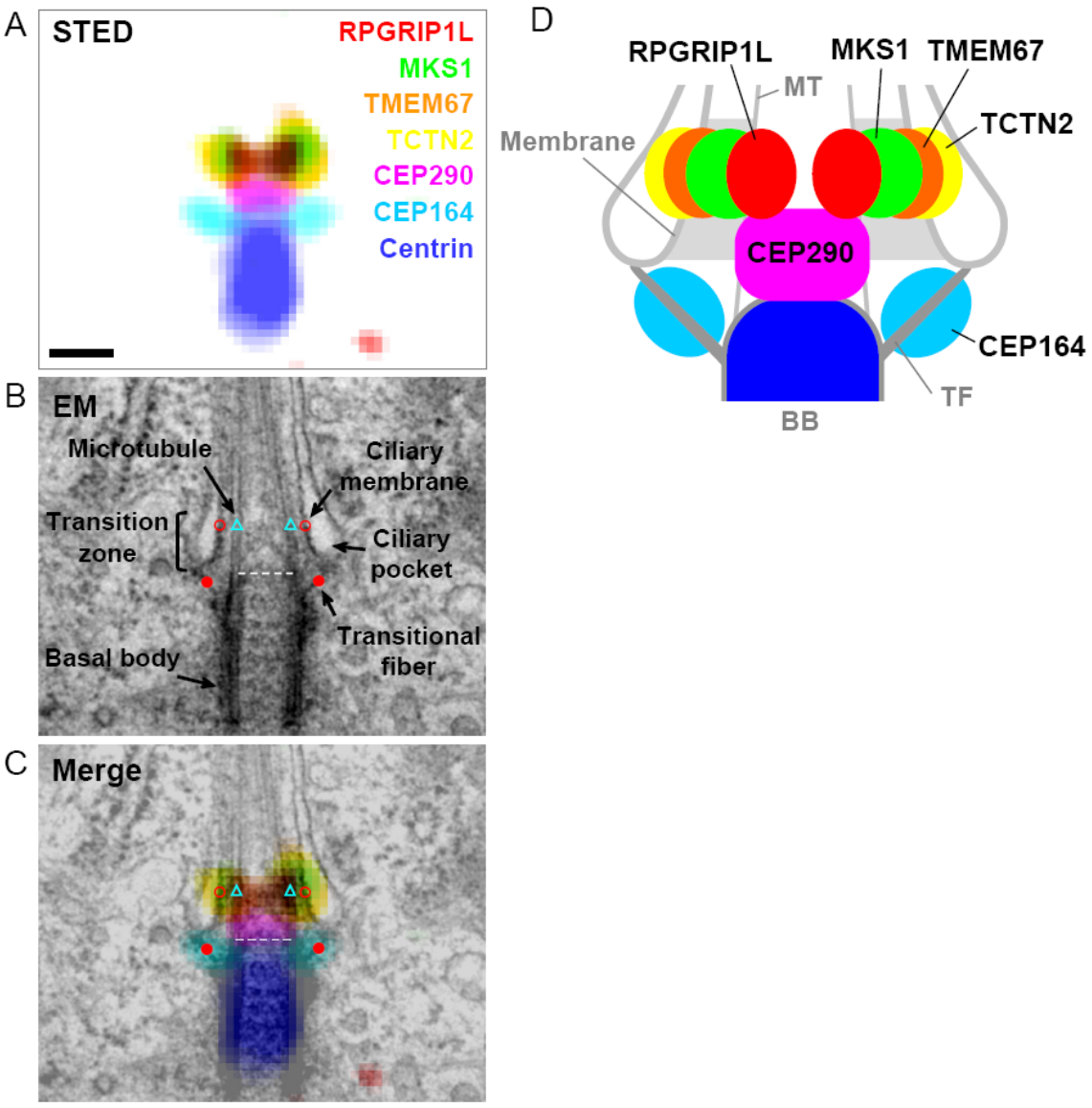

Figure 4-12 A molecular architecture at the base of the primary cilium obtained by overlapping coordinate-defined superresolution images of TZ/TF proteins and an EM image. (A) A 7-color STED image illustrating the relative locations of important TZ/TF proteins. (B) A typical equally-magnified EM image of a primary cilium in an RPE-1 cell, where TFs are marked as red dots ("●"), doublet microtubules as blue triangles "△", and TZ membrane as red circles "○". (C) A merged image of (A) and (B) obtained by aligning the TFs in EM and CEP164 in STED. RPGRIP1L was close to the doublet microtubules; TMEM67 and TCTN2 were localized mostly toward the TZ membrane, while MKS1 was localized midway between the membrane and microtubules. CEP290, right above the basal

body, was localized at a different axial level from the other TZ proteins. Scale bar, 200 nm. (D) A localization model of TZ/TF proteins at the ciliary base pinpointing the positions of these proteins relative to each other and to known structural elements.

From the merged EM-STED image (Figure 4-12C; Figure 4-13C and F), it is clear that RPGRIP1L, MKS1, TMEM67, and TCTN2 were at the same axial level, with RPGRIP1L localized to the axoneme while TMEM67 and TCTN2 localized to the ciliary membrane. MKS1 localized between the ciliary and the axoneme. TCTN2 was slightly more outside than TMEM67 (Figure 4-12D). Potentially these three proteins were at the level of Y-links, serving as structural or functional components of Y-links in both the axoneme and membrane ends. CEP290, although widely considered as an element of the TZ, was localized in a rarely explored space in EM between the BB and other TZ proteins, with a width similar to that of the axoneme.

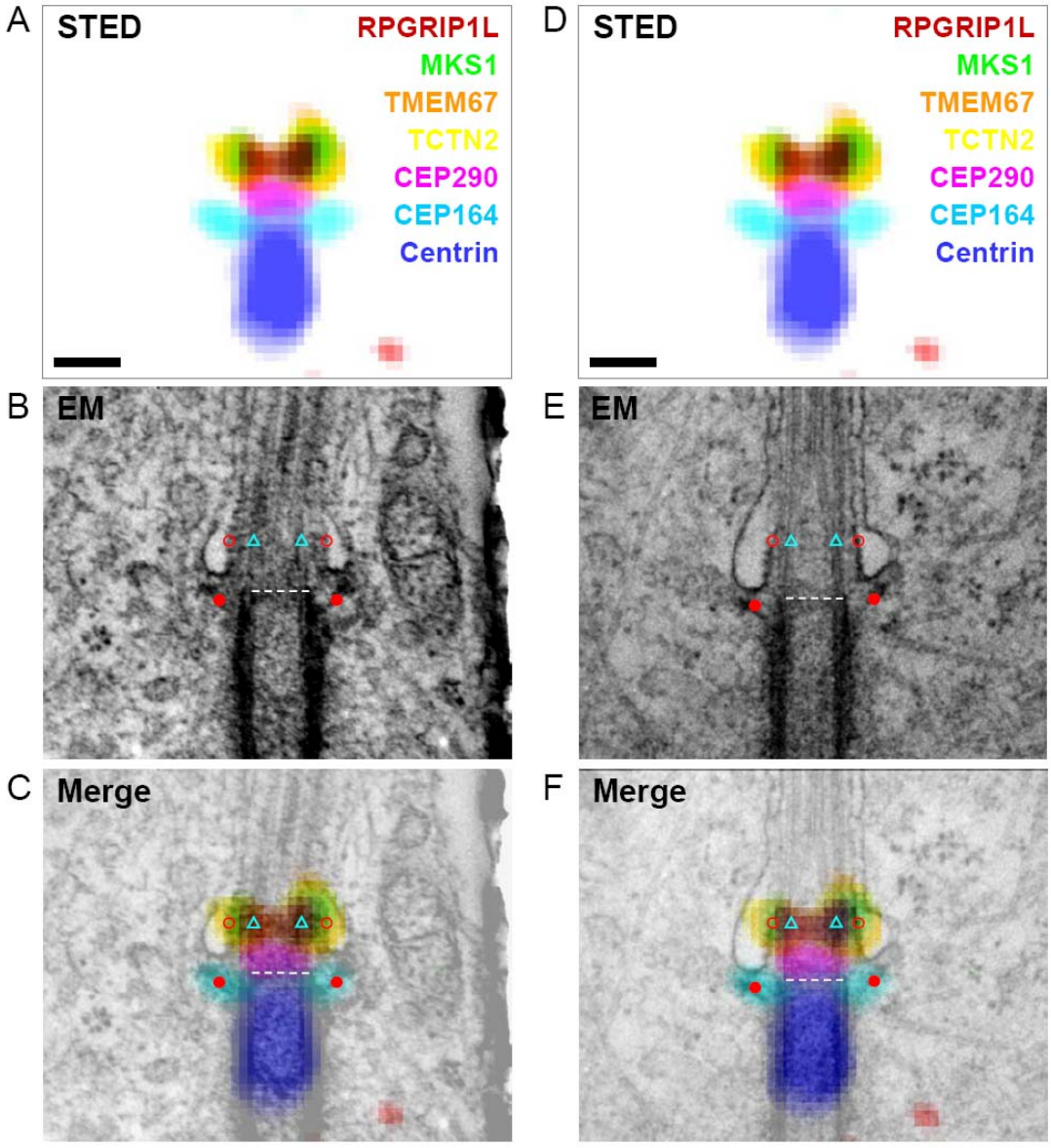

Figure 4-13 Overlapping of multicolor superresolution images of TZ/TF/BB proteins and different EM images revealing their consistent relative localization. (A and D) A 7-color STED image (repeated) demonstrating the relative localization of TZ/TF/BB proteins. (B and E) Two typical EM images of primary cilia in RPE-1 cells in addition to the one shown in Fig. 3 where TFs are marked as red dots ("●"), TZ microtubules as blue triangles "△", TZ membrane as red circles "○", and the distal end of the basal body as a white dashed line. (C and F) Merged images from (A) and (B) or (D) and (E) revealing

consistent localization of TZ/TF/BB proteins with respect to the EM ultrastructure. Scale bars: 200 nm.

4.4.2 IFT88 is localized across TZ and TF

To explore this idea, we used dual-color STED imaging of IFT88 and TCTN2 to pinpoint the location of IFT88 on the architecture map of the ciliary base (Figure 4-9D). For the three-puncta pattern of IFT88, the proximal and distal puncta were located immediately proximal and distal to the TZ proteins in the axial direction, with the proximal puncta colocalized with TF component CEP164 and the distal punctum situated on or at the distal edge of the TZ (Figure 4-14A to C). For the Y-shaped pattern, the distal branch of the Y spread toward the ciliary compartment, while the two proximal branches were localized at the proximal edge of the TZ, extending toward CEP164 (Figure 4-14A). The lateral diameter and the axial position relative to centrin confirmed that the proximal puncta of IFT88 and the TF protein CEP164 colocalized with each other up to our resolution limit (Figure 4-14, B and C).

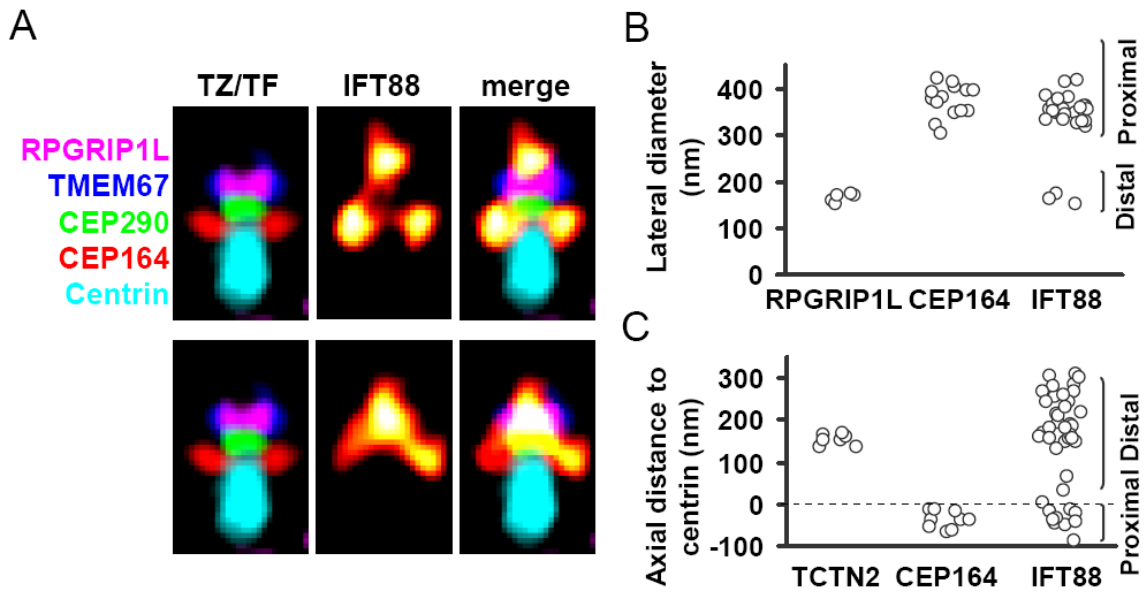

Figure 4-14 IFT88 distribution at the ciliary base (A) Three-puncta (upper panels) and Y-shaped (lower panels) patterns of IFT88 superimposed on the TZ/TF framework. IFT88 was localized at two levels, one at the TF and the other close to the distal edge of the TZ. (B, C) Similar lateral and axial positions of CEP164 and proximal puncta of IFT88 suggesting that IFT88 was localized to TFs.

4.5 Discussion

Here, we have shown that these proteins extending from TZ to TF/BB in RPE cells were examined with a home-built dual-color superresolution STED microscopy through the optimization of imaging and sample preparation. To our knowledge, the laterally and axially diverse dimension and localization among them are previously unreported and have significant implications for our understanding of their patterns and potential functions of the proteins in TZ/TF/BB. It is also notable that our data suggest the distribution of IFT system, for example IFT88, at the ciliary base is correlated with the architecture of

TZ/TF/BB, offering a possibly mechanistic link between TZ and IFT proteins. Our finding that at least two distinct fashions of IFT88 present at the TZ/TF may imply a possible gating mechanism regulating the IFT88 pattern. Taken together, our STED data incorporated with the EM result allows us to propose a potential localization model of those TZ/TF/BB/IFT proteins.

The advent of superresolution techniques opens up access to the understanding of the morphometric information in subdiffraction scale, which is particularly suitable for the studies of primary cilia. Most of optically superresolution microscopy is implemented on the basis of a narrow-tailored effective point spread function to probe the fluorescence signal, such as STED microscopy. This thus largely takes advantage of an immunofluorescence/ fluorescent protein-based approach which offers a promising ability of specific staining to select the primary information as well as a better representative of molecular copies, compared to immuno-EM. For STED, one could retain a similar protocol of sample preparation used for confocal imaging, but some optimization works are needed to enhance the signal level that diminishes as a result of depletion mechanism. To study TZ proteins, a rigorous focusing condition should be taken into consideration due to the focusing sensitivity to their results.

Our data has shown that RPGRIP1L, MKS1, and TMEM67/TCTN2 may localize to the distinct part of Y-links where RPGRIP1L may play an anchoring role at the axoneme end of the Y-links while TMEM67 and/or TCTN2 may play an anchoring role at the membrane end of the Y-links. A previous study [18] had indicated that RPGRIP1L is essential for ciliogenesis and formation of ciliary gate, which may relate to its intrinsic anchoring site where it could scaffold others Y-links-associated proteins. Moreover, RPGRIP1L may

be able to regulate the IFT-driven components near the axoneme, responsible for gating function. Our observation that TCTN2/TMEM67 is localized to membrane/transmembrane domain supports those previous reports [17-18,107] in which they may control ciliary trans-/membrane composition. Based on our finding, CEP290 is located in the proximal TZ, potentially serving as a foundation for TZ formation. However, the recent study [16] showed CEP290 is a Y-link component which bridges microtubule and membrane in TZ. This divergence may be caused by the different recognition of residues in CEP290 protein through immuno-technique. To address this issue, the CEP290 pattern was confirmed using two distinct antibodies (C-terminal and N-terminal) to CEP290 (Figure 4-15). The results suggest that RPGRIP1L, TMEM67 and TCTN2, MKS1, and CEP290 all occupy different spatial domains within the TZ. Together, the locations of these proteins provide a basic architecture map of the ciliary base.

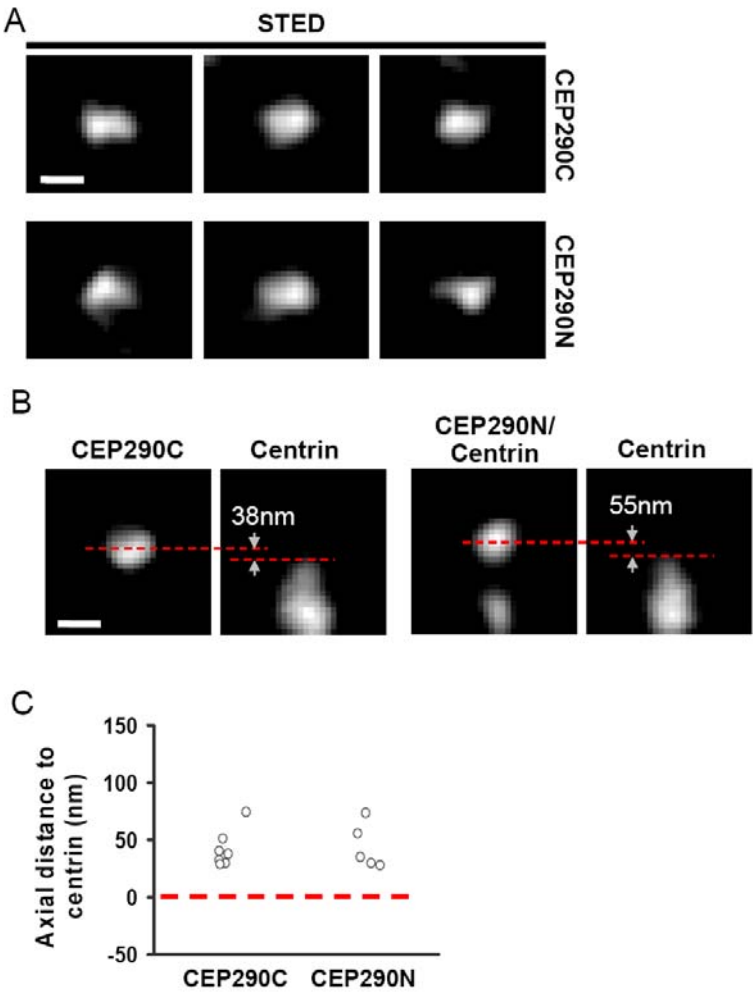

Figure 4-15 Comparison of superresolution images of CEP290 using C-terminal and N-terminal antibodies revealing indistinguishable localization patterns. (A) STED imaging of CEP290 immunostained with C-terminal or N-terminal CEP290 antibodies, named CEP290C and CEP290N, showed similar lateral and axial localizations. (B) The axial positions of CEP290C and CEP290N were determined using the distal edge of centrin as a reference coordinate. Scale bars: 200 nm. (C) Distributions of axial positions of CEP290C and CEP290N were similar. The average distance to centrin is 42±16 nm for CEP290C and 44±20 nm for CEP290N.

4.6 Materials and Methods

4.6.1 Cell Culture

Human RPE-1 cells (in some cases with stably expressed centrin-eGFP)[108] were grown on #1.5 cover glasses coated with poly-l-lysine, in DMEM/F12 supplemented with 10% FBS, 12mM HEPES, 2.5mM L-glutamine, 2.4g/L sodium bicarbonate, and 1% penicillin/streptomycin at 37°C and 5% CO_2 up to 60%~90% confluence depending on the experimental conditions, and then incubated in serum-deprived media for 48 hours.

4.6.2 Antibodies

Ac-tub antibody (anti-acetylated α-tubulin mouse IgG, ab24610, Abcam) was used at a dilution of 1/1000 for epifluorescence imaging and 1/2000 for single-color STED imaging as a ciliary marker. IFT88 (anti-IFT88 rabbit IgG, 13967-1-AP, Proteintech) was prepared at 1/200. RPGRIP1L (anti-RPGRIP1L rabbit, HPA039405, Sigma-Aldrich, at 1/300), TCTN2 (anti-TCTN2 mouse IgG2a, ab119091, Abcam, at 1/500), MKS1 (anti-BBS13 rabbit IgG, 16206-1-AP, Proteintech, at 1/50) and TMEM67 antibodies (anti-TEME67 rabbit IgG, 13975-1-AP, Proteintech, at 1/200) were used for labeling the TZ. For CEP290, two antibodies were used: one for the N-terminal and one for the C-terminal (see comparison in fig. S8). For the N-terminal CEP290 antibody, a synthetic peptide consisting of residues 11-24 of mouse Cep290 with a C-terminal cysteine added for conjugation to KLH (IKVDPDDLPRQEEL-C) was used to generate rabbit polyclonal antibodies (Genscript). The resulting antiserum was affinity purified on an agarose support (Thermo Fisher Scientific) according to the manufacturer's instructions. This N-terminal CEP290 antibody was used at 1/100. The C-terminal CEP290 (anti-CEP290 rabbit IgG,

ab84870, Abcam) against residues 2429-2479 was used at 1/500. CEP164 (anti-CEP164 rabbit, 45330002, Novus Biologicals) antibody was used at 1/2500 for the staining of TFs. For secondary antibodies, Oregon Green 488 antibodies (goat anti-rabbit or goat anti-mouse, Invitrogen) were used at 1/200 for TCTN2, MKS1, and RPGRIP1L and 1/1000 for TMEM67, CEP290, CEP164, and IFT88. Biotin antibodies (anti-mouse IgG, B6649 or anti-rabbit IgG, B8895, Sigma-Aldrich) were diluted at 1/200 and V500 streptavidin (561419, BD Horizon) was used at 1/100 for labeling the TZ/TF/IFT proteins for two-color STED imaging or at 1/500 for ac-tub and IFT88 for single-color STED imaging.

4.6.3 Immunofluorescence

The cells were fixed 5 min at room temperature with 4% paraformaldehyde (PFA) and then immediately fixed in -20°C methanol for 10 min. Following fixation, cells were washed 2-3 times in PBS, permeabilized with 0.1% PBST (PBS + Triton X-100), and then blocked with 1% normal goat serum and 2.5% BSA in 0.1% PBST for 30 min at room temperature. Samples were incubated with primary antibodies in block solution for 1 hour at room temperature, and rinsed at least 3 times in PBST. Cover glasses were then incubated with secondary antibodies or biotin antibodies for 45 min at room temperature, and washed again 3 times in PBST. For biotin antibodies, the cells were stained with streptavidin conjugated to V500 dye (BD Horizon) for 20~30 min, followed by at least 5 times in PBST. Finally, the samples were mounted with 86% glycerol in PBS.

4.6.4 STED Microscopy

The home-built continuous-wave STED setup (491-nm for excitation and 592-nm for

depletion) was set up and calibrated as described in the previous sections, with the addition of a 447-nm excitation laser for dual-color STED imaging. For single-color STED imaging of TZ/TF proteins (except TCTN2), ac-tub imaged in the confocal mode (447-nm laser) was used to find cilia only and one TZ/TF protein at a time was later imaged in STED mode (491-nm laser). Ac-tub was stained with V500 at a low concentration to avoid crosstalk to the channel of TZ/TF proteins labeled with Oregon Green 488 and illuminated at 491 nm for STED imaging. For TCTN2 (mouse), IFT88 (rabbit) labeled with a low concentration of V500 was used as a ciliary marker. For dual-color STED imaging, centrin-eGFP excited at 491 nm was used to identify the ciliary base, while CEP290, RPGRIP1L, MKS1, TMEM67, TCTN2, or CEP164 was labeled with V500 at the 447-nm channel. Since GFP was partially excitable at 447 nm, centrin could be detected in both channels and two sequential acquisitions of STED images can be easily aligned by correlating the centrin location. To determine the relative position of IFT88 to TCTN2, IFT88 (447-nm laser channel) was first used to find cilia in the confocal mode and then STED images were acquired for both proteins. For all STED imaging, the excitation power was operated at 0.3-1.5μW depending on the signal level of TZ/TF/BB/IFT proteins. For CEP290, TMEM67, CEP164, centrin, or IFT88 where the signals were strong, the excitation laser was set to a power close to the lower bound of the working power. For MKS1 where the signals were substantially weak (fig. S1A), the excitation power was generally operated at the upper bound. A medium excitation power close to 1 μW was used for imaging TCTN2 and RPGRIP1L. The power of the depletion laser was set differently for different proteins based on photon counts. The power was generally set to ~100mW for centrin, 90~100mW for CEP290, TMEM67, CEP164, or IFT88, 70~90mW for TCTN2 and RPGRIP1L, and

~60mW for MKS1. When signals were weakened after a few acquisition scans, the depletion power could be reduced by ~10mW to maintain a sufficient signal level. To find an optimal focus, STED images were acquired at different planes every 100 nm around an initial position until the sample was photobleached substantially usually after 3-5 times of scanning. For all STED scans, a step size of 25 μm and a dwell time of 20 μs were used to gain the maximal signal-to-noise ratio as well as to satisfy the Nyquist criteria for spatial sampling. The registered photon count per 20 μs was generally above 100 and about 50% reduction with STED acquisition.

4.6.5 Data Analysis

The shown confocal and STED images were smoothed and contrast-enhanced with generalized Tikhonov regularization [109]. Thresholding was applied to illustrate the FWHM of objects in Figure 4-3C to J using ImageJ. For quantitative width measurement of the TZ/TF proteins, the STED images were first cleaned by a mean filter of 1 pixel and background subtracted. For CEP290 and RPGRIP1L, images were fitted with a two-dimensional Gaussian function $A\exp[-(x-x_0)^2/(\sqrt{2}c_1)^2-(y-y_0)^2/(\sqrt{2}c_2)]+C,\theta$ (Figure 4-5, M and N) to identify the principal axes and to find the FWHMs (Figure 4-5, A, B, G, and H), where c1 and c2 were used to determine the FWHM by multiplying the factor of $2\sqrt{2\ln 2}$. The fitting curves agreed well with the data, except that some RPGRIP1L images had a slight intensity dip in the middle. For MKS1, TMEM67, TCTN2, and CEP164, STED images clearly displayed two distinct peaks in the lateral direction, so the lateral FWHMs were determined by measuring the distances of two intensity peaks (Figure 4-5, C to F and I to L). To define the reference coordinate in the axial direction, the distal

edge of centrin was located by pinpointing the position of the FWHM of the fluorescent intensity along the primary axis of centrin (Figure 4-7). To obtain the 7-color superresolution image, six single-color STED images including centrin, CEP164, CEP290, RPGRIP1L, MKS1, and TCTN2 were first merged using ImageJ (three additive primary colors RGB and three subtractive primary colors CMY). This merged image was then overlapped with the image of TMEM67 (azure color) using ImageJ. To obtain a white-background 7-color superresolution image, a negative process was applied to the whole merged image using ImageJ (Figure 4-16). To obtain the multicolor superresolution images of IFT88 with TZ/TF/BB proteins, centrin, CEP164, CEP290, RPGRIP1L, TMEM67, and IFT88 were merged using ImageJ with red-hot color assigned for IFT88 images.

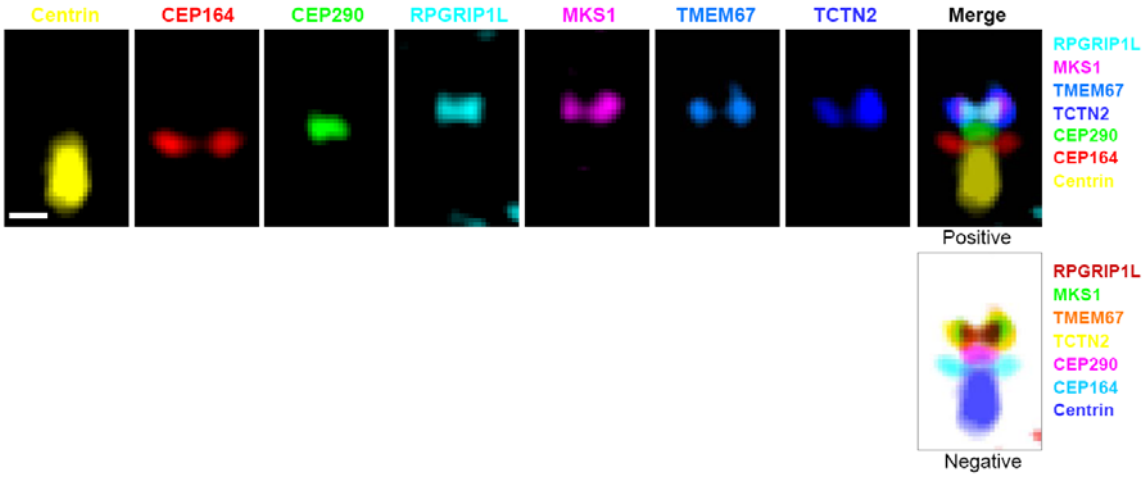

Figure 4-16 The process of obtaining a multicolor superresolution image using multiple single-color STED images of different TZ/TF/BB proteins. A series of single-color STED images of TZ/TF proteins were axially positioned based on the average relative distances to the distal edge of centrin from dual-color STED images (first row). The threshold of each single-color image was adjusted based on the FWHM to represent their shape and size. These axially-positioned images were overlapped to create a 7-color superresolution image

of proteins at the ciliary base. To obtain a white-background image to be merged with an EM image, colors of the merged multi-color image (top) were inverted with a corresponding negative mapping (bottom). Scale bar: 200 nm.

5 Determination of the mechanism of IFT and localization of SMO protein through transition zone using superresolution imaging

5.1 Introduction

In the previous chapter, I have studied the architecture of TZ/TF in primary cilia and performed statistical analysis to gain their dimension and distribution based on the dual-color STED system. Here, different cell culture conditions or signaling perturbation will be undertaken to examine our working hypothesis for their interaction with TZ proteins. Next, we will further study the functional and dynamical IFT proteins and determine how they localize to this region through live-cell STED imaging. Additionally, Smo, a Shh signaling protein, will be studied to characterize its distribution at the cilia base and to differentiate the transport mechanism from IFT proteins.

5.2 Ciliary growth conditions affecting the distribution patterns of IFT88 at the ciliary base

5.2.1 STED imaging reveals distinct IFT88 distribution at different cell confluence

Using the architecture map as a guide shown in previous chapter, we next sought to understand how IFT particles travel through the ciliary base. In our previous STED image analyses of the IFT-particle protein IFT88 in human fibroblasts, we observed two distinct distributions at the ciliary base, namely the Y-shaped and three-puncta patterns. Similar patterns of IFT-particle distribution were also seen in RPE1 cells, and intriguingly, they correlated with the specific growth conditions of cilia. Examining a series of culture

conditions to test their effects on IFT protein distribution, we found that the confluency of cells would affect the distribution patterns of IFT88. In a subconfluent condition (~700 cells/mm^2) where cilia were short or IFT88 only aggregated as a dot (Figure 5-1A, left), a large population of cilia possessed a Y-shaped pattern of immunostained IFT88 (Figure 5-2A). In some cases where only a dot was observed in confocal microscopy, the subdiffraction images showed a full-ring pattern of IFT88 (panel vi of Figure 5-2A), potentially representing a state before ciliogenesis with the BB orienting orthogonal to the imaging plane. In confluent conditions (~1000 cells/mm^2) where cilia were long and present in most cells (Figure 5-1A, middle), a large population of cilia possessed a three-puncta pattern of IFT88 (Figure 5-2B). Therefore, a cell completing its ciliary growth tended to form a three-puncta pattern of IFT88, while a cell during the process of ciliogenesis tended to form a Y-shaped pattern.

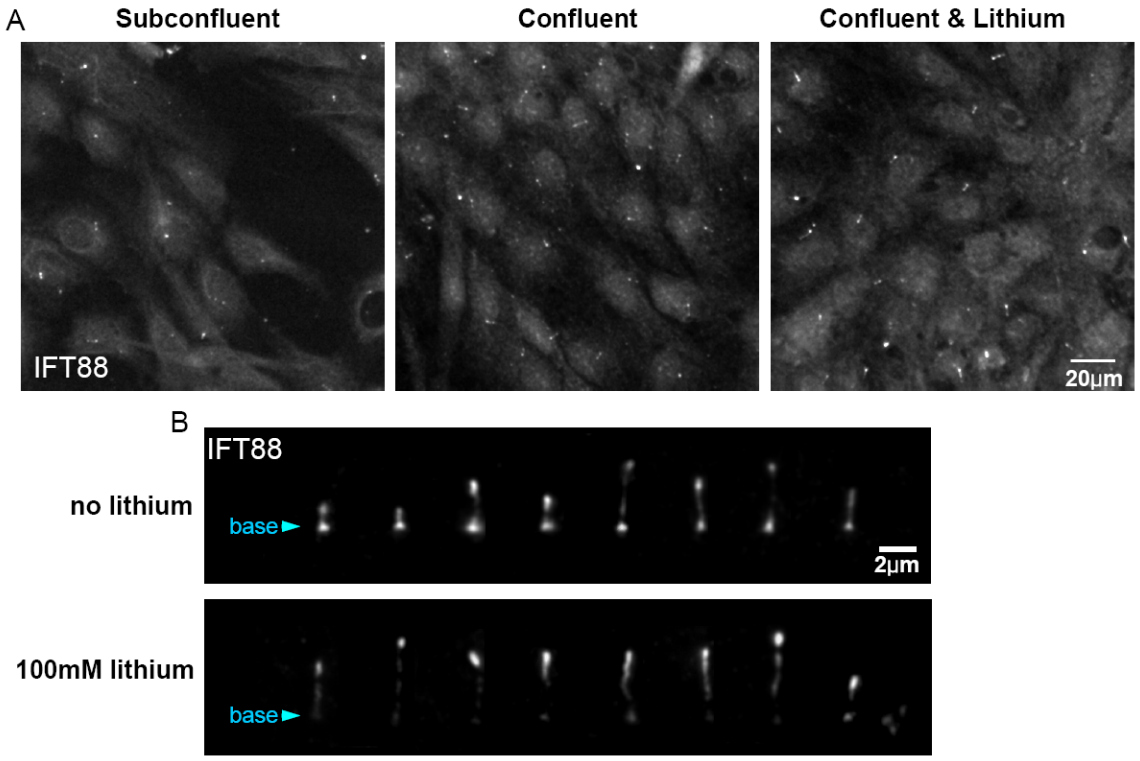

Figure 5-1 Distributions of IFT88 in primary cilia of RPE-1 cells under different growth conditions. (A) Epi-fluorescent images of IFT88 in different conditions. (left) Subconfluent cells (~700 cells/mm^2) had short cilia or had aggregated IFT88 that appeared as dots. (middle) Under confluent conditions (~1000 cells/mm^2), cilia were long and present in most cells. (right) Confluent cells (~1000 cells/mm^2) treated with 100 mM lithium ion (LiCl) for 1 hour before fixation possessed elongated cilia. (B) Lithium effects on IFT88 distribution observed in epi-fluorescent images. Primary cilia with Li^+ treatment were longer (lower panel) than those without treatment (upper). IFT88 was evenly localized to the tip and base in untreated cells (upper) while a large proportion of IFT88 moved to the ciliary tip after Li^+ stimulation (lower). Arrows show the location of the ciliary base.

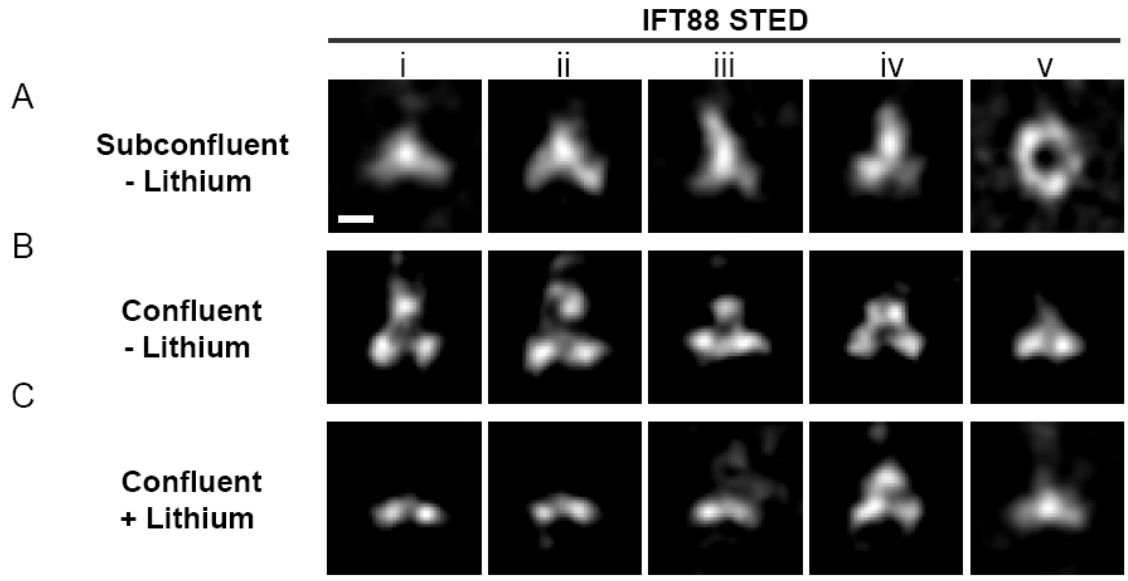

Figure 5-2 Effects of ciliary growth conditions on the distribution patterns of IFT88 at the ciliary base. (A) Sample STED images of IFT88 at the ciliary base of subconfluent RPE-1 cells (~700 cells/mm^2) exhibiting a dominant population of the Y-shaped pattern. Sometimes an IFT88 aggregate was found to possess a full-ring pattern (v). (B) A dominant population of the three-puncta distribution pattern of IFT88 for confluent cells (~1000 cells/mm^2). (C) A novel two-puncta pattern of IFT88 prevailed at the base of cilia stimulated to elongate by 100 mM of Li^+; Li^+ treatment depleted the IFT88 population at the distal punctum within an hour.

5.2.2 Perturbation of ciliary growth transforms the patterns of IFT88 distribution

To test the effects of perturbing ciliary growth, lithium ion (LiCl), known to stimulate ciliary elongation [59], was added cells in a confluent condition (~1000 cells/mm^2) for 1 hour before fixing the cells. We observed that cilia grew longer than those without Li+ treatment (4.3±0.81 μm with Li+ vs 3.6±0.80 μm without Li+), and IFT88 also accumulated at the ciliary tip (Figure 5-1B). STED microscopy showed yet another dominant pattern of IFT88 at the ciliary base, i.e. a pattern of two puncta at the proximal end (Figure 5-2C). The relative intensities between the proximal and distal regions are shown in Figure 5-3 to

illustrate the relative distributions in terms of locations. Populations of different patterns under different conditions are shown in Figure 5-4, demonstrating that each ciliary growth condition had a different dominant distribution pattern of IFT88.

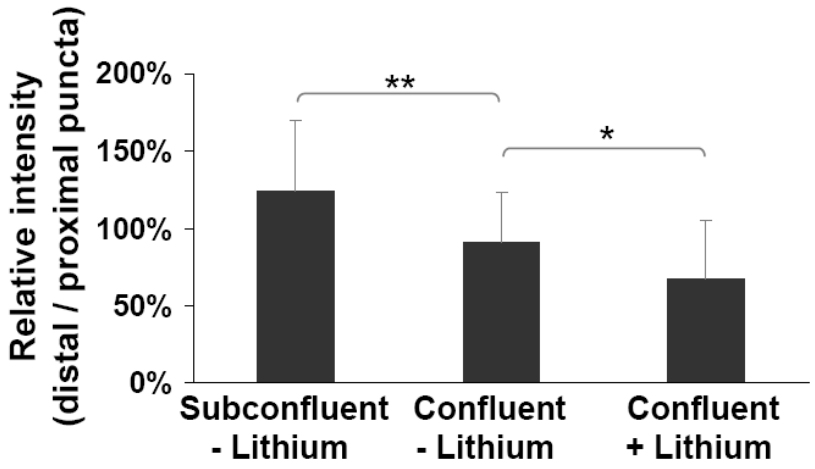

Figure 5-3 Superresolution imaging revealed that the relative intensity of the distal punctum to the proximal puncta was affected by ciliary growth conditions. The ratio is close to one in the confluent cells. In subconfluent cells, IFT proteins had a higher population within TZ toward the distal end. With Li^+, the intensity of the distal punctum was significantly reduced, leaving a two-puncta pattern.

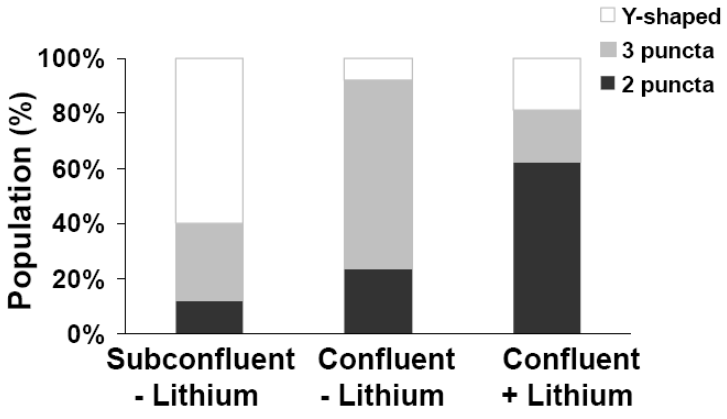

Figure 5-4 Different population distributions of Y-shaped, three-puncta, and two-puncta patterns in different ciliary growth conditions.

5.2.3 Possible gating mechanism of the TZ

Our observations of the exclusive localization of IFT88 to the base of primary cilia allow us to propose a configuration of IFT88 under the changing cellular status. Three different scenarios of localization including (i) Y-shaped, (ii) three puncta, and (iii) two puncta are thought to result from a corresponding gating mechanism within TZ. In the early-middle stage of ciliary growth, more IFT88 may be required to maintain a lengthening cilium, therefore, the status of transferring IFTs (Y-shaped) can be seen. An on-gate mechanism is probably actively involved to guide IFT particles to enter TZ. But in the steady stage, three puncta of IFT88 whose proximal and distal ends are mostly located at the entrances of TZ, i.e. TFs and Y-links, may be regulated under an off-gate circumstance. In this case, IFT activity across TZ is possibly not significant. When treating a steady-state assembly cilium with lithium, IFT88 at the distal side is depopulated dramatically, yielding a two-puncta pattern. This rapid change at the distal part implies that gating function may be still inactive such that Y-shaped distribution is not recruited yet.

The distribution patterns of IFT88 (Figure 4-14, Figure 5-2) clearly showed two levels of IFT-particle reservoirs at the ciliary base, one at the TFs and the other immediately distal to the TZ. When cells were in a subconfluent condition, IFT particles likely undergo continuous entry into the ciliary compartment to form influx streams through the TZ, which are imaged as the two branches of the Y-shaped pattern (Figure 5-5A). When cilia reach their full length under confluent conditions, equilibrium occurs with IFT particles accumulated in two reservoirs, corresponding to the proximal puncta of the three-puncta pattern at the TFs and the distal punctum on or at the distal side of the TZ

(Figure 5-5B). Stimulation of further ciliary growth following addition of Li^+ quickly depletes IFT particles in the distal reservoir, leaving a two-puncta pattern at the TFs (Figure 5-5C). The sites of IFT particle accumulation, which change depending on the phase of flagellar growth, likely represent important zones for cargo loading, processing, or sorting of the IFT machinery. Future structural and functional studies of the TZ guided by this architectural map will enhance our understanding of the biogenesis and function of cilia.

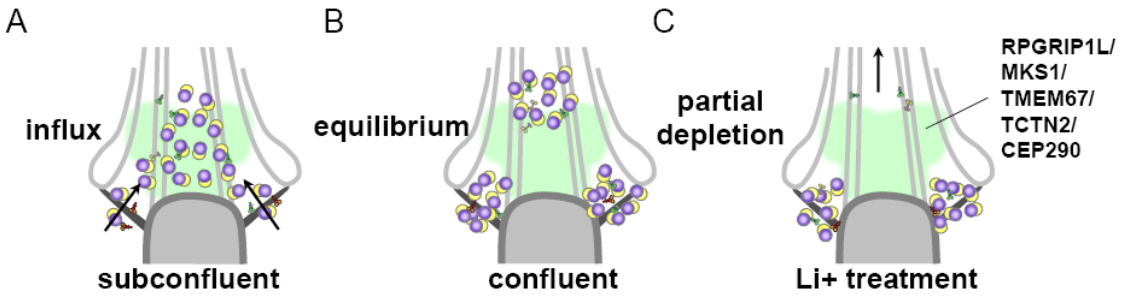

Figure 5-5 Models depicting postulated movements of IFT88 consistent with the protein's three different distribution patterns.

5.3 Live-cell STED imaging reveals IFT proteins trafficking across TZ at a reduced speed

5.3.1 IFT88, IFT57, and IFT20 trafficking along primary cilia in MEF and IMCD cells

To understand the motor-driven motion of IFT complex in the primary cilium, we first conducted live cell epifluorescent imaging to track various IFT proteins and analyzed the dynamics. To enable the direct observation of IFT movement in live cells, MEF cells

were transiently transfected with plasmids construct, the DNA of which was introduced into the nucleus of the cell. For the best results and the most efficient transfection, optimization trials were performed, such as an optimal ratio of DNA to transfection reagent, amount of transfection reagent, working medium, confluency, and etc. Figure 5-6(A) shows most of the MEFs were successfully transfected with IFT88-eGFP plasmid, while a comparison result in Figure 5-6B indicates that the cells did not uptake a sufficient amount of plamids. The transfected cells were further serum-starved up to 48 hours to promote the ciliary growth. Figure 5-7A to C displays the different IFT constructs consistently presented in the primary cilia. Note that IFT20 protein was not only concentrated to a primary cilium, but also largely presented around the cilium (Figure 5-7C). IFT88 and IFT57 were similarly localized to primary cilia only. This may imply different transport mechanisms among these three proteins while recruitment occurs outside a primary cilium.

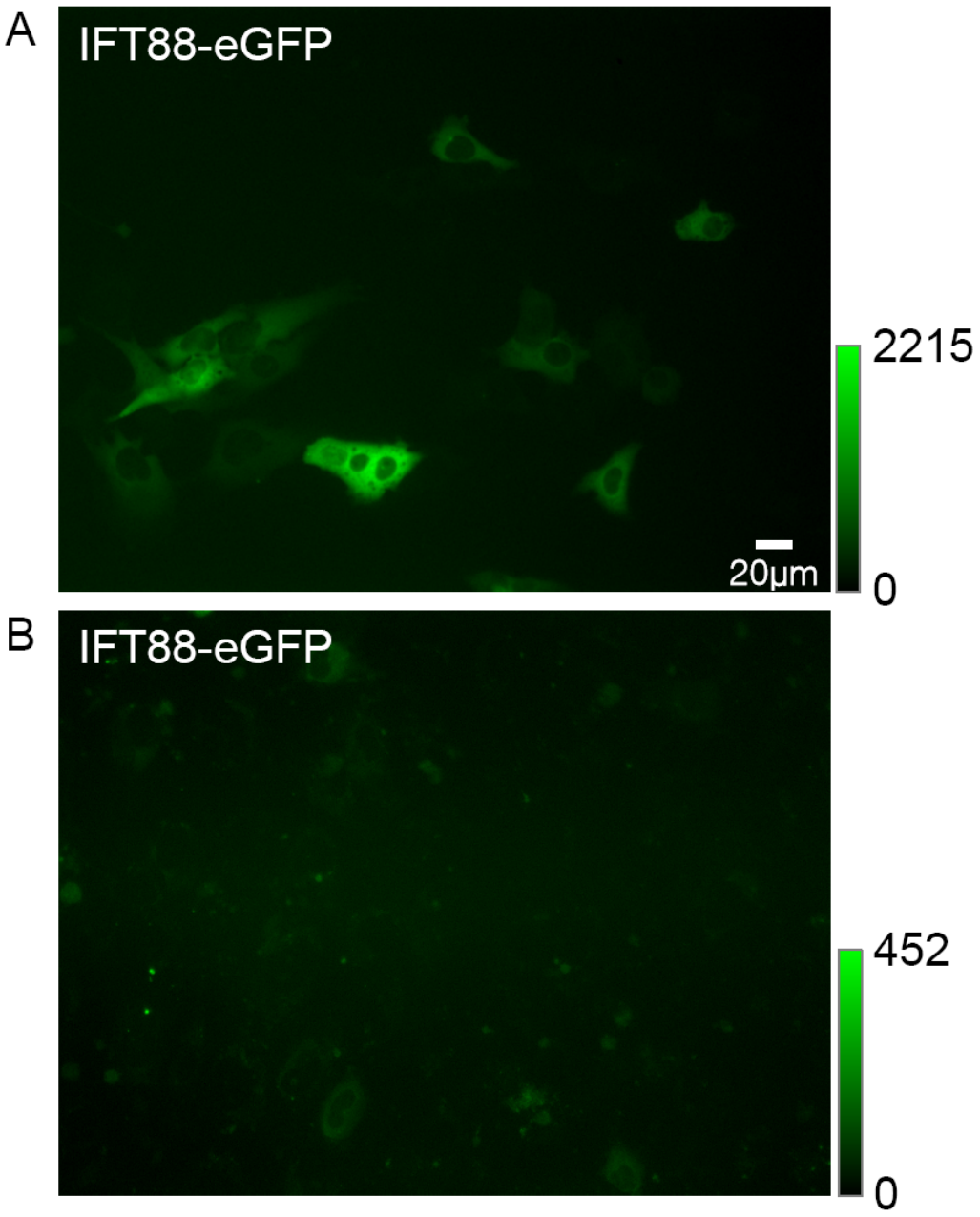

Figure 5-6 Optimization of DNA plasmid transfection. (A) An image of successfully transfected MEF displaying IFT88-eGFP signal from most of cells. (B) A comparison result caused by an un-optimized protocol showing the weak GFP intensity from cells.

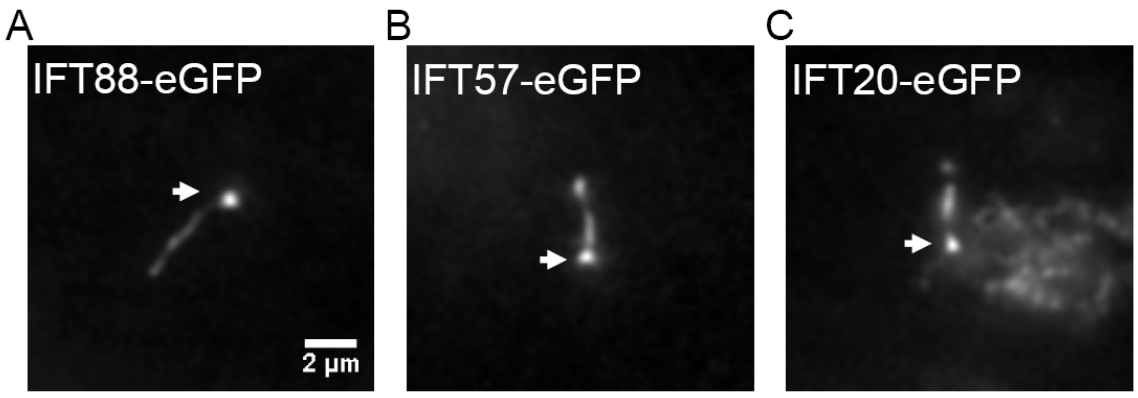

Figure 5-7 IFT proteins were found in the primary cilia of MEF cells. (A-C) is a snapshot of a primary cilium where IFT88-eGFP, IFT57-eGFP, or IFT20-eGFP was detected. A triangular shape at the base of ciliary marked as arrow was found in these three IFT proteins.

In addition, we used a stably IFT88-EYFP expressing cell line[100] to study the dynamics of IFT particles. One of the advantages using this cell line was the ease of sample preparation without a DNA transfection step to label IFT particles. Next, we conducted time-lapse imaging of these MEF and IMCD cell lines to gain the trafficking information of IFT complexes. A kymograph analysis was used to graphically represent the spatial position of IFT particles over time so as to characterize the speed of movement. For example, in the Figure 5-8A, four time-lapse snapshots of an IMCD cell primary cilium are shown. The IFT88 particle, highlighted by an arrow, moved in the retrograde direction (from tip to base) over the time. A kymograph analysis (Figure 5-8B) displayed multiple IFT88 anterograde, depicted by lines, and retrograde, depicted by dash lines, activities along the cilium. We also observed other types of IFT proteins in plasmid-transfected MEF with IFT20-, IFT57-, and IFT88-GFP constructs. For instance, IFT20 (Figure 5-8C and D) and IFT57 (Figure 5-8E and F) trafficking in MEF were

observed bi-directionally.

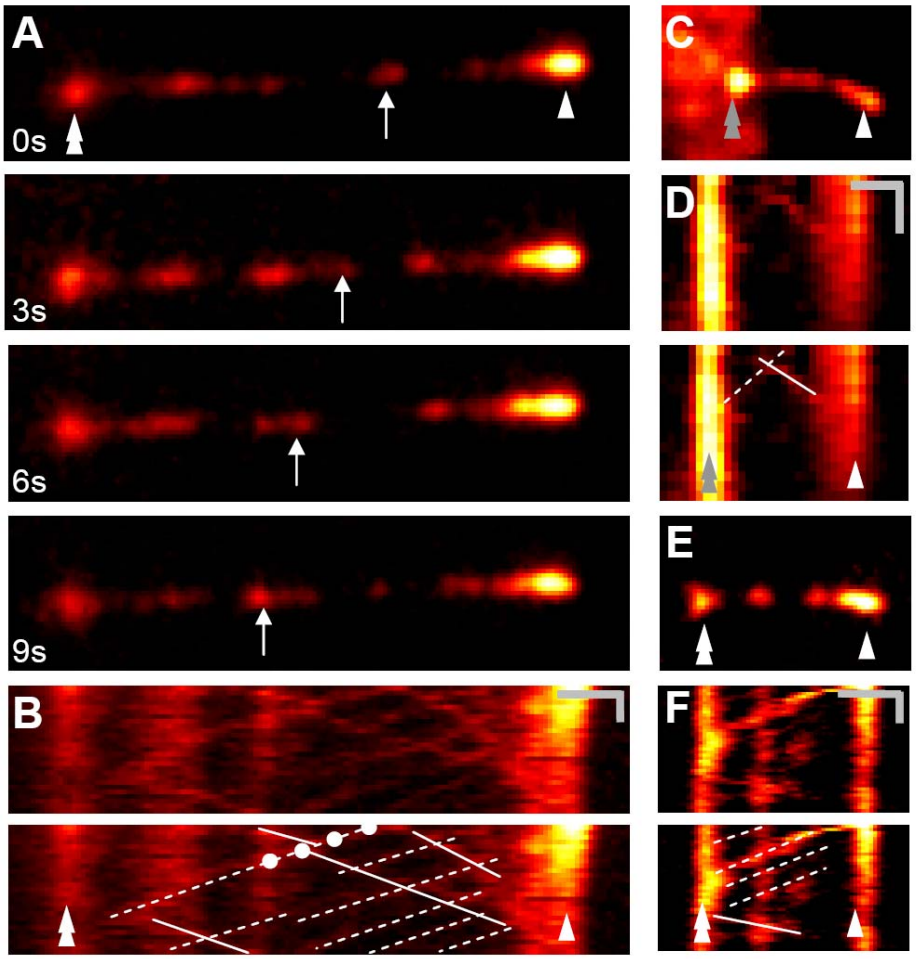

Figure 5-8 Live-cell epifluorescent imaging illustrating anterograde and retrograde IFT activities along the cilia. (A–B) Time-lapse images and the kymograph of IFT88-EYFP stably expressed in mouse IMCD cells. The arrows indicate the locations of an IFT complex at different time points. The locations of these arrows were determined by tracking the positions of one kymograph line in (B), Length scale bar: 1μm; time scale bar: 10s. (C–D) A snapshot and the kymograph of transfected GFP-tagged IFT20 in MEFs. Length scale bar: 1 μm; time scale bar: 5s; (E–F) A snapshot and the kymograph of transfected GFP-tagged IFT57 in MEFs. Length scale bar: 1 μm; time scale bar: 10s. Double triangle markers label the ciliary base, while single-triangle markers label the ciliary tip.

We have also statistically characterized the anterograde and retrograde speeds of IFT20, IFT57, and IFT88 particles in MEF, revealing that averaged anterograde speed was greater than retrograde speed (Figure 5-9A). However, the various speeds among those IFT particles were not significantly different. This can be verified by immunostaining of IFT88 protein in the above three cell lines. First, the immunostained IFT88 in primary cilia shows an identical pattern of GFP-tag IFT88 (Figure 5-10A) as the control data. A similar distribution of IFT88 was also found among IFT20 and IFT57 proteins (Figure 5-10, B and C). Based on IFT distributions, IFT proteins, at least these three proteins, are colocalized to the cilia in complexes and move along the microtubules in groups. This result is compatible with the previous finding which proposed a model of the protein interactions between IFT20, IFT52, IFT57, and IFT88 shown in Figure 5-11[110].

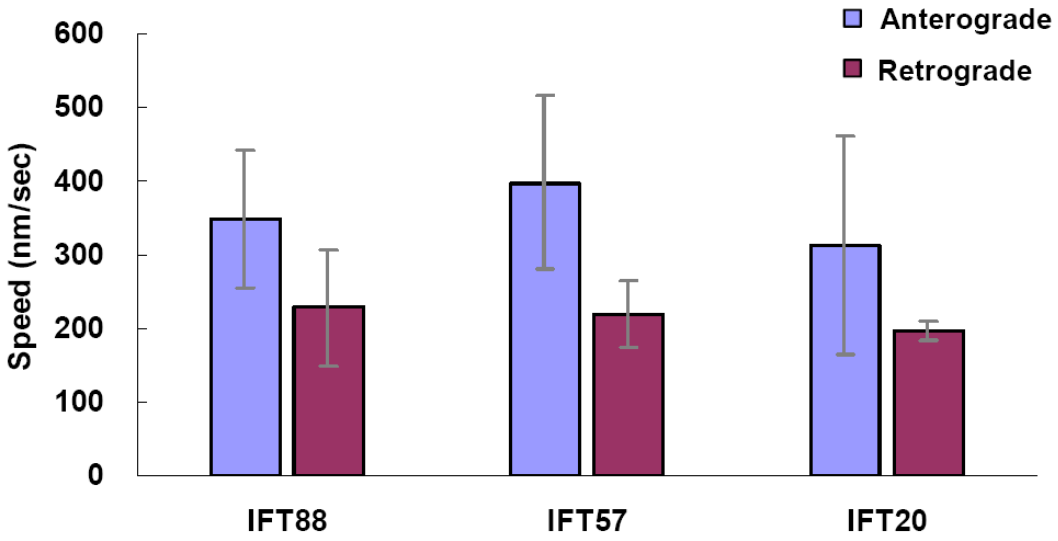

Figure 5-9 Averaging anterograde and retrograde speeds measured from GFP-tagged IFT20, IFT57, and IFT88 in MEF. The speed in anterograde direction was greater that in retrograde. The average anterograde measured from these three proteins are similarly between 300 and 400 nm/s; their retrograde speed were consistently between 200 and 300

nm/s.

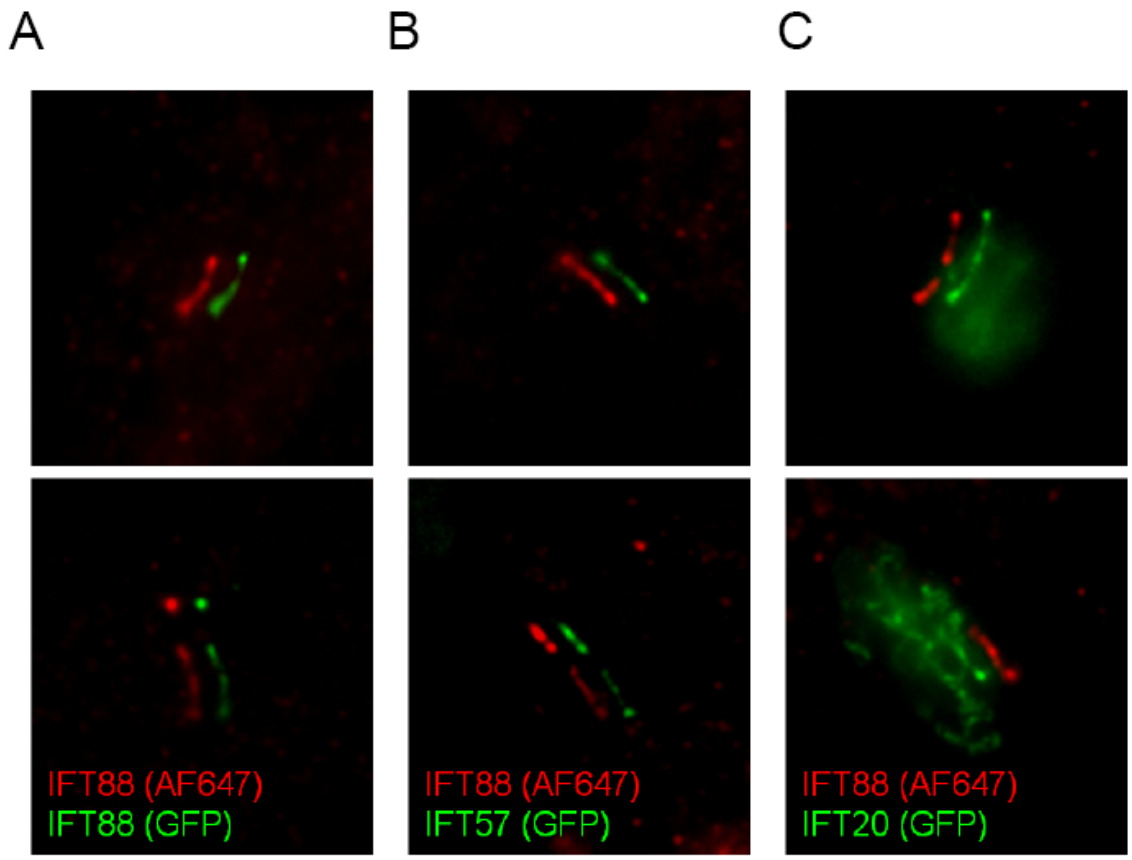

Figure 5-10 IFT20, IFT57, and IFT88 were colocalized in primary cilia. (A) Two primary cilia were immunostained with the antibody against IFT88, showing the same distribution as transfected GFP-IFT88 protein. (B and C) Colocalization of Immunostained IFT88 and GFP-tagged IFT20 and IFT57 were found in the primary cilia. The side-by-side shifted two primary cilia which actually refered to the same primary cilium were presented in each image for the better comparison of IFT distribution pattern.

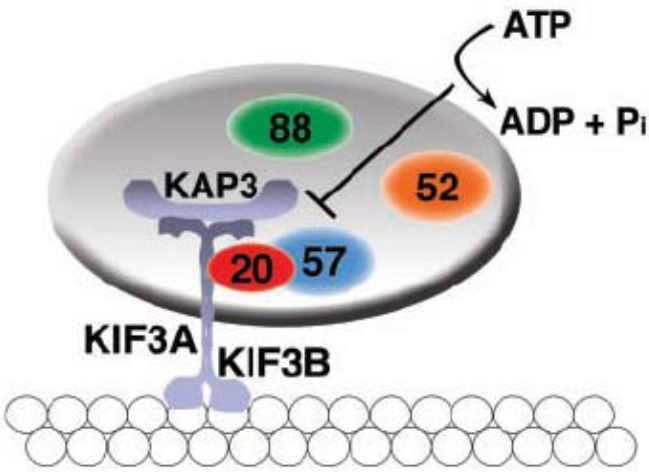

Figure 5-11[110] A proposed model of IFT complex containing IFT20, IFT52, IFT57, and IFT88 which interact with each other to be transported along doublet microtubules to the tip of the axoneme.

5.3.2 Live-cell STED imaging revealed IFT88 trafficking across TZ at a reduced speed

The study of IFT speed at the ciliary compartment has been demonstrated with a conventional microscope by tracking a set of IFT particles moving either from base to tip or vise versa. Although the intersected spots may remain unresolved, the IFT trafficking along a distant pathway, usually several micrometers, can be recorded without difficulty. However, it is very challenging to track IFT events at the base of cilia, particularly within TZ, if the same technique is used. IFT dynamics will be happening at a tiny and short region, mostly within the diffraction limit. To overcome this, we first used epifluorescence microscopy to collect the information of IFT speed along ciliary compartment. Based on this data, we estimated the acquisition rate required to track IFT particles in TZ. The acquisition speed can be improved by choose a proper scanning area and step size. The

chosen scanning field was just enough to cover TZ or slightly wider because the event in ciliary compartment can be obtained separately. To discern how fast IFT proteins pass through TZ, we performed a kymograph analysis to determine the speed. In the experiment, significant photobleaching from GFP occurred during STED imaging. Therefore, deconvolution processing was used to enhance signal and reduce noise. Intensity normalization may be also undertaken to compensate for the decrease in fluorescence. Moreover, the change in IFT88 pattern will be observed and then the mechanism with which IFT88 move into or out of TZ will be determined.

5.3.2.1 Optimization of subdiffraction-resolution imaging of primary cilia in live cells

Although STED microscopy is one of the most promising techniques for the study of live-cell dynamics, capturing IFT events at the base of primary cilia remains a challenge because of the need of sufficient temporal and spatial resolution as well as signal level. Here, we attempted to first address those imaging complications and to optimize the proposed system as described in the previous sections. To enable and facilitate superresolution live-cell imaging of primary cilia, we optimized sample preparation protocols. Thus, the IMCD cell line tagged with IFT88-eYFP was used due to the high percentage of IFT88 found in primary cilia, as compared to the transient transfection in MEFs with plasmids. However, we found the IMCD cells tended to form primary cilia in the up-pointing orientation when cells were overcrowded or even stacked. This may hinder the better observation of primary cilia and characterization of IFT motion. To address this, cells were incubated in DMEM/F12 with 0.1% FBS for 24-48 hours when they reached ~50% confluence. Therefore, final confluence was about 90-100% at which

cells were just contacted or about to be contacted so a monolayer condition and the optimal ciliogenesis were reached. We found monolayer cells tend to grow more horizontal primary cilia than stacked cells do. However, this condition may contradict the maximal ciliogenesis. Thus, samples should be always prepared well to fulfill at least 24 hours starvation and 90% confluence for live-cell imaging. A snapshot of the optimized sample is shown in Figure 5-12, in which many of horizontal primary cilia were found in the field of view, facilitating the search of primary cilia while conducting live-cell imaging.

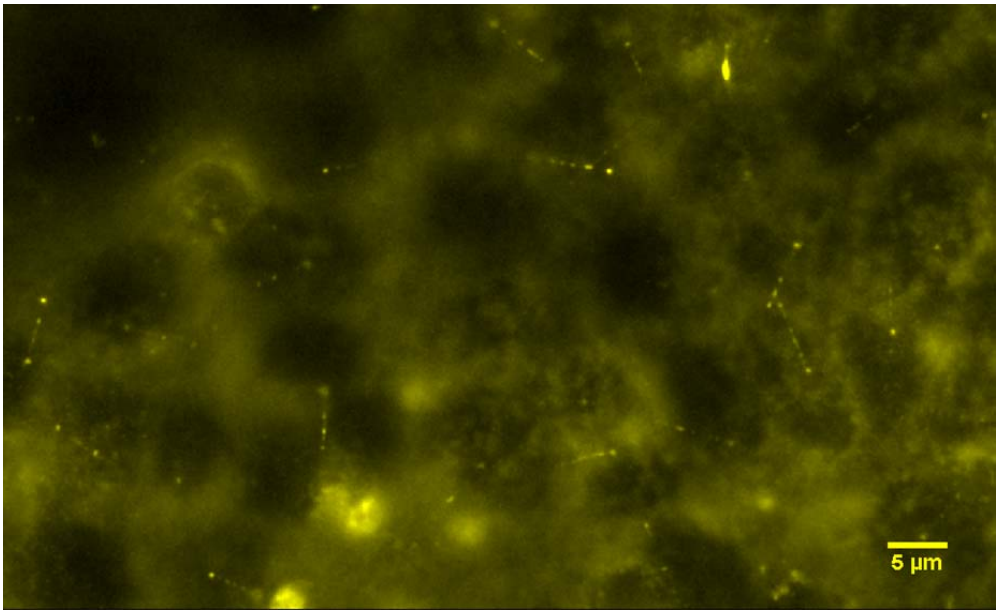

Figure 5-12 Monolayer and 90%-100% confluent IMCD cells grew nearly horizontal primary cilia 48 hours after serum starvation at 0.1% FBS media.

In terms of imaging, we developed a scanning program for time-lapse acquisition, which is different from a single-frame recording. This updated scanning method will allow us to run a continuous scanning path from frame to frame by flipping the scanning route at every even frame (Figure 5-13) without the need of moving back to the original, which

may cause a time delay due to large-step and rapid motion. Furthermore, we optimized the scanning settings such as dwell time, step size, sampling rate, laser power, and so forth. Specifically, the glass-bottom dishes with #1.5 glass thickness were used to gain the best performance while conducting superresolution imaging using the 100X objective. One of the most challenging issues for live cell imaging was the deficiency of signal level since rapid scanning is required to minimize cytotoxicity. To address this, we tried a larger step size of 40-50 nm to improve the signal-to-noise ratio by up to 4-fold and thus the frame rate was increased accordingly. To capture a fast IFT event, usually less than one second, we also optimized the scanning field and frame rate to reach this temporal scale. In the next section, I will seek to characterize IFT88 trafficking at the TZ using our STED microscope.

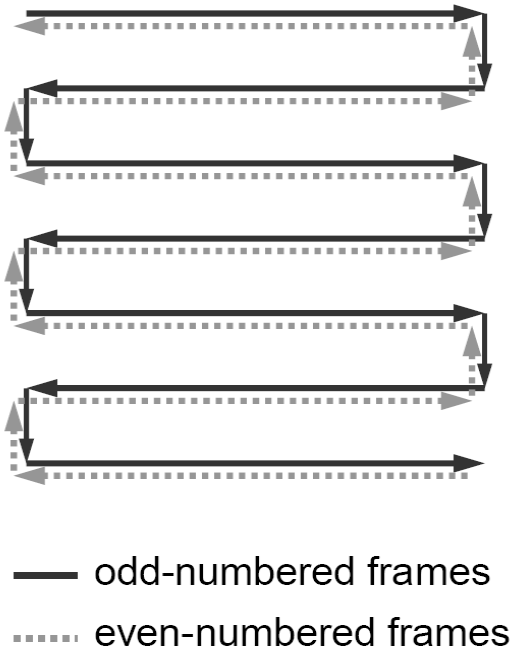

Figure 5-13 A continuous scanning path achieved by flipping the scanning route at every even-numbered frames. This smooth scanning path can avoid an abrupt change of large step and time delay while driving stage back to the same origin.

5.3.2.2 Characterization of IFT protein movement at the TZ

To further understand the dynamics of IFT complexes at the base of primary cilia and how IFT pass through the TZ, we conducted superresolution STED imaging of the stable expressing IFT88-eYFP mouse IMCD cells; conventional microscopy cannot effectively resolve the IFT88 configuration in such a compact compartment as the TZ/TF. A set of time-lapse images at rate of 0.6 second per frame was demonstrated in Figure 5-14. The change in IFT88 pattern showed that IFT88 trafficking occurred dynamically within one second.

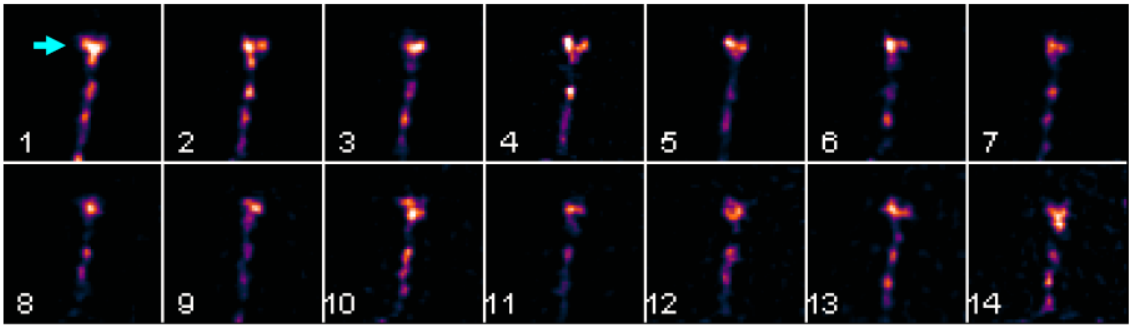

Figure 5-14 14 snapshots of IFT88-eYFP at primary cilia of mouse IMCD live cells. The change of IFT88 pattern was observed at 0.6 second per frame. The IFT88 distribution pattern changed over the time. Two typical configurations, Y-shaped and three-puncta can be found. Arrow labels the ciliary base.

In Figure 5-15A, eight snapshots of IFT88 at 0.4 sec/frame showed an IFT88 particle, highlighted by arrows, which moved from proximal TZ or TFs to the ciliary compartment via TZ. Two dash lines indicate the location of proximal and distal puncta of IFT88, and the region between these lines is the TZ. By tracking this IFT complex along the pass line drawn in Figure 5-15B (left panels), the corresponding kymograph analyses were reported in the right panel. Notably, the slope of the line within TZ was different from that of the

line at the cilium. The kymograph result revealed that IFT complex move slower at the TZ than in the ciliary compartment. The velocity of IFT88 transport at the TZ was determined based on the slope of the line within TZ, yielding a speed of ~200 nm/s. However, the speed in the cilium was ~400 nm/s, which is almost twice as that in the TZ. Figure 5-15C displays the other time-lapse images showing a similar result in that the speed at the TZ was reduced. Therefore, the first five images in Figure 5-15A shows how the IFT88 particles at the left proximal punctum passed through the TZ from the base to the distal side. Then these particles left the TZ and moved along the cilium at a faster speed as seen in the 6th to 8th snapshot. This unreported finding may imply a functional gating mechanism or a size-selected structure in TZ that regulates IFT88 speed.

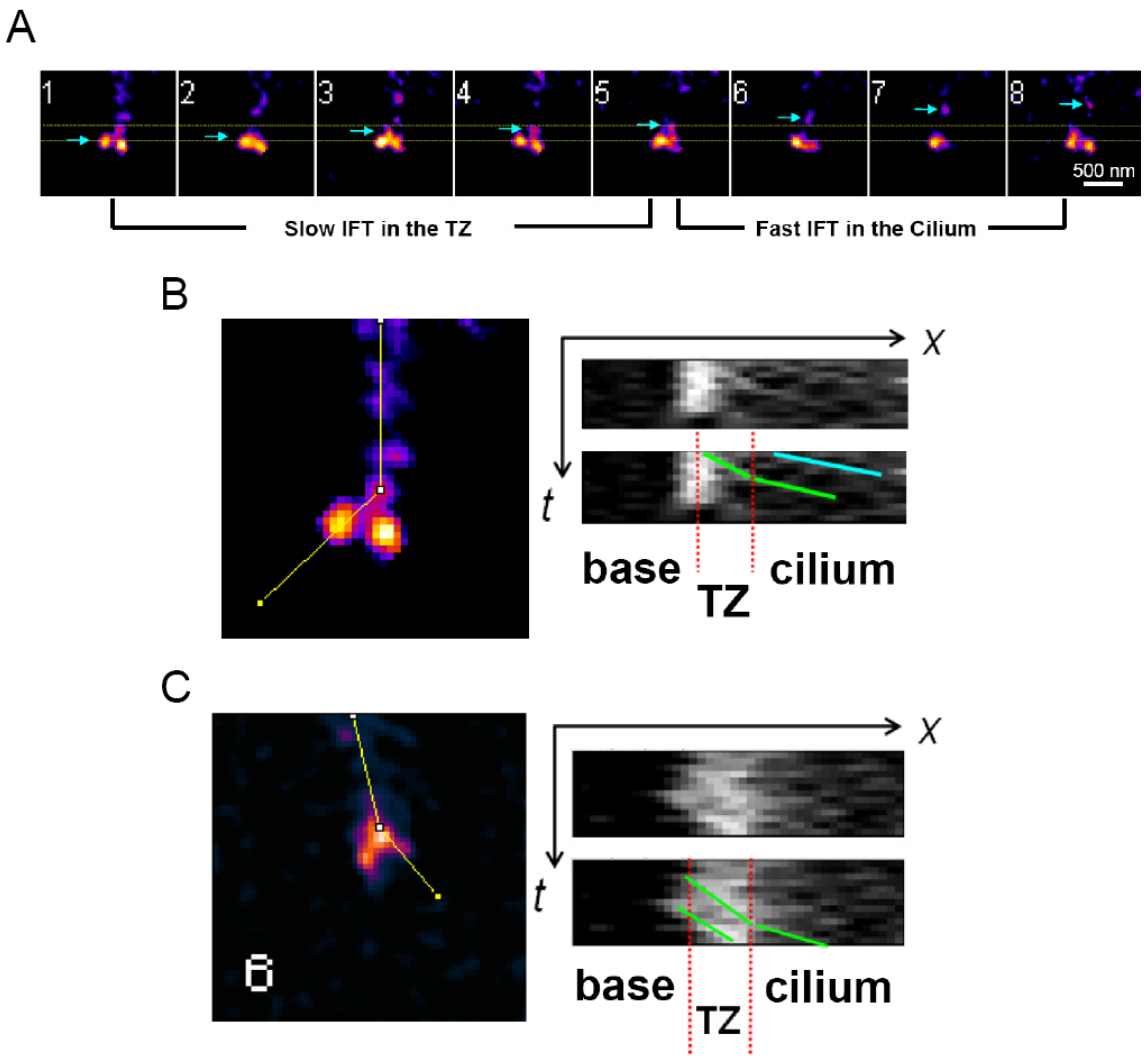

Figure 5-15 Live-cell STED imaging revealed IFT88 trafficking across TZ at a reduced speed (A) One IFT88 particle (arrows) tracked by eight acquisition frames moved from TFs to the cilium through TZ (between two dotted lines). (B and C) Left panels indicate a defined route for kymograph analysis which exhibited distinct trafficking speeds at TZ and cilium (right panel). Acquisition speed, 0.4 sec/frame.

5.4 STED imaging indicates the different localization of SMO and IFT88 at ciliary base

As highlighted in the chapter 1, the SMO is one of most important proteins involved in Shh signaling pathway. We have shown the special localization pattern and mechanism of IFT particles at the base of cilia as well as the architecture of TZ through the imaging of fixed and live cells in the previous sections. Here, we further explore SMO signaling protein to gain insight into its transport mechanism or how it interacts with IFT or TZ proteins at the ciliary base. Thus, STED microscopy is still required to obtain this information with better spatial discrimination.

5.4.1 SMO translocates to primary cilia under SAG stimulation

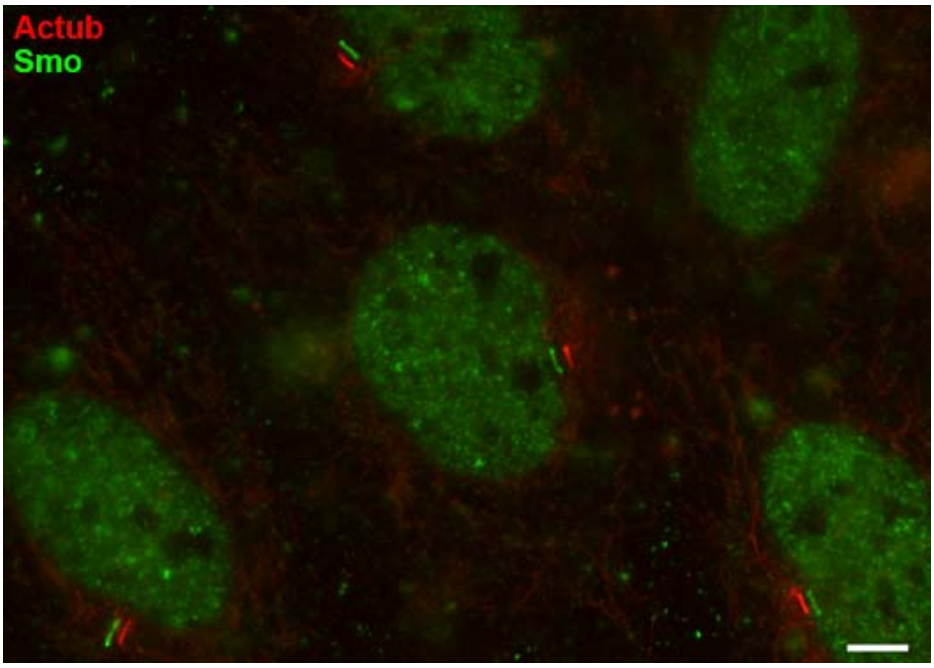

Figure 5-16 An epifluorescent image showing immunostained SMO and actub colocalize at primary cilia of MEFs that was treated with 2 μM SAG for 17 hours. The shift between two color images over cilia is done for better comparison of their patterns. Scale bar, 5 μm.

To enable the presentence of SMO at primary cilia, MEFs are incubated with the use of SAG (SMO agonist) to induce activation of Shh signaling [111]. Among a series of different cell lines such as RPE-1 or human fibroblast, SMO is relatively enriched in MEFs in response to SAG. Thus, the 24-hour serum-deprived cells are treated with SAG for 17 hours and are then immunostained with antibodies against SMO and actub to recognize cilia. Figure 5-16 shows SMO protein presents at the primary cilia as multiple ciliated cells are labeled with actub. For better observation, SMO and actub images around primary cilia are displayed side-by-side. Although SMO is not specifically labeled for primary cilia as opposed to actub, SMO signal at the cilia is still high enough. Experimentally, we found the percentage of SMO present at primary cilia is not uniform over culture plates. For example, the field of view in Figure 5-16 has higher value, ~80 %. Also, to maintain cells at a good condition, we serum starve MEFs no longer than 48 hours, and thus ciliated cells are not ubiquitously found.

The response of cells to SAG stimulation depends on the length of time and concentration. Here, we performed treatment at two different lengths. We found SMO signal at primary cilia about 1~2 hours after the treatment (Figure 5-17A) where actub was co-labeled to identify the location of cilia. In general, the SMO intensity is not remarkably high at this time. SMO is mostly accumulated at the base (arrows) of some primary cilia as shown in the first three panels of Figure 5-17A. A small population of cilia have clearly high SMO signal as displayed in the last two panels. As the length of treatment increased up to 17 hours, SMO is mostly translocated along entire primary cilia and is accumulated relative more at the base and tip in some cases (Figure 5-17B). In addition, the fluorescence intensity of SMO substantially boosts at cilia; therefore, the

background is relatively suppressed. The maximal intensity of SMO at primary cilia for 2- and 17- hours SAG are shown in Figure 5-17C where the longer treatment causes nearly 6-fold increase in SMO intensity and the SMO tends to fill up a cilium.

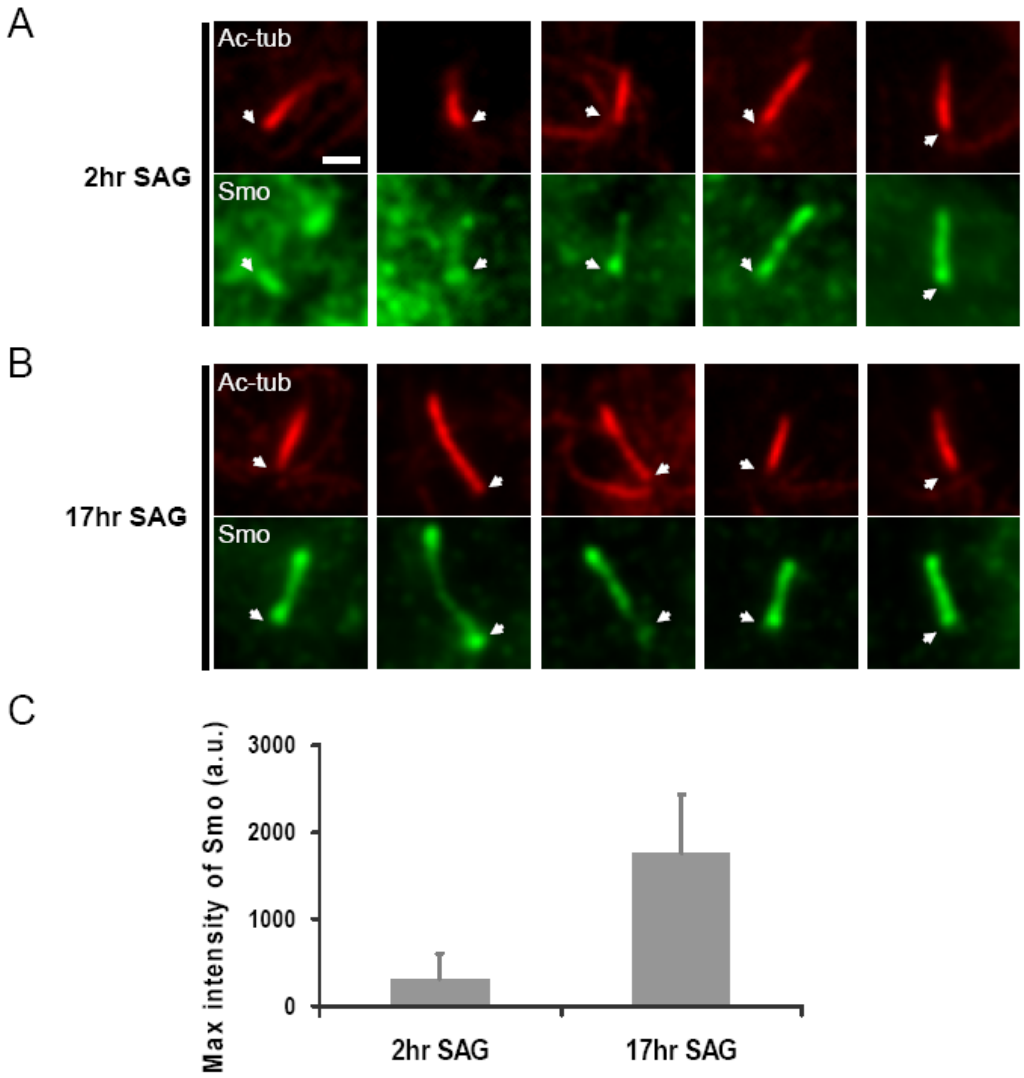

Figure 5-17 SMO intensity versus length of SAG treatment. (A and B) Five typical epifluorescent images show SMO translocates to primary cilia 2 or 17 hours after 2 μM SAG incubation. Arrows label base of cilia. During the early stage of treatment, SMO tends to present at the base of primary cilia but is less fluorescent. (C) Comparison of maximal intensity of SMO for 2 and 17 hours SAG. Scale bar, 1 μm.

5.4.2 STED imaging shows SMO distribution at the ciliary base

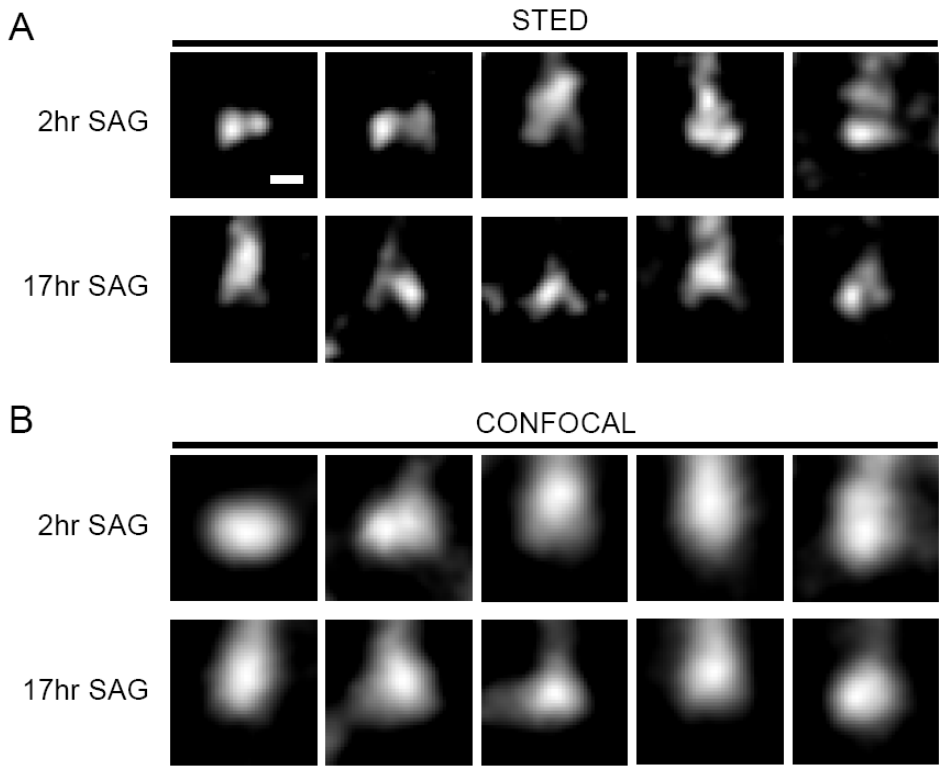

Figure 5-18 STED microscopy reveals two-dot or two-branch distribution of SMO at the base of cilia for 2 and 17 hours SAG stimulation. (A) STED; (B) confocal results. Scale bar, 200 nm.

The detailed studies of SMO localization through primary cilia, especially TZ, are hindered due to diffraction-limited resolution with conventional microscopy as reported in Figure 5-16, Figure 5-17, and Figure 5-18B. Hence, we conducted STED microscopy for investigation of SMO distribution. Figure 5-18A demonstrates five typical subdiffraction images of SMO pattern for two SAG conditions. The results show several different types of distribution. When SMO only accumulates at the base of cilia, most STED images reveal two separate dots over this region; when SMO extends from the base into cilium, the "Λ" or "人"distribution can be found with STED imaging. But the

difference of SMO pattern at the base between 2-hour and 17-hour SAG stimulation are not significant. Some of images showing two-dot pattern in the early stage of treatment imply that SMO may first dock at the ciliary base. The docking site may be at transitional fibers as we have seen the pattern of IFT88, or at transition zone, or at cilium compartment.

5.4.3 SMO transport via the membrane site of TZ with dual-color STED imaging

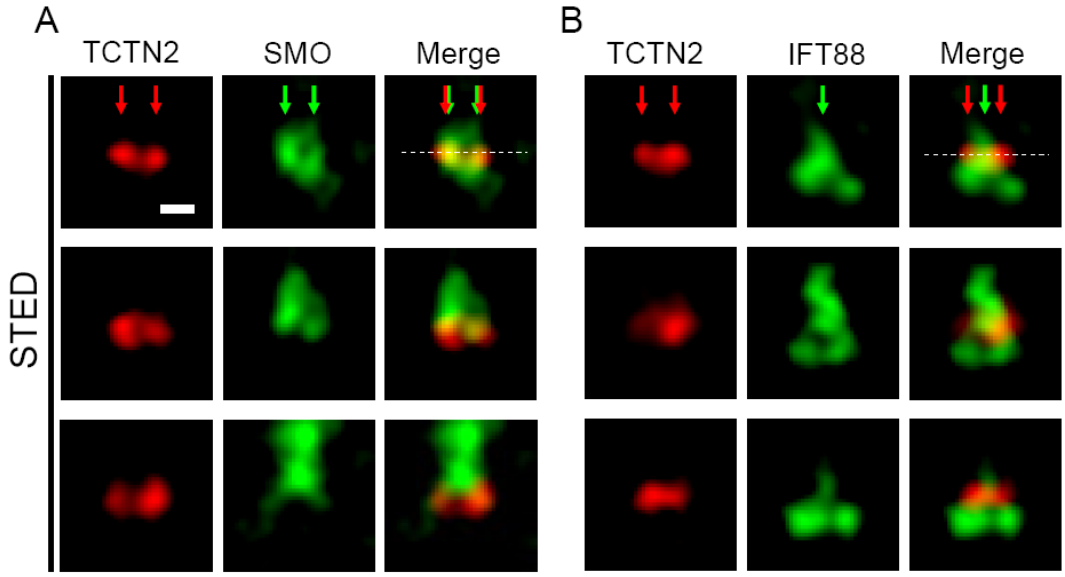

Figure 5-19 Two-color STED imaging of TCTN2 and SMO or IFT88 in MEF. (A) Three examples of TCTN2/SMO image reveal that they are co-localized at the TZ. (B) STED images indicate the different location of distal punctum of IFT88 and TCTN2. Arrows label the peak intensity of features. Scale bar, 200 nm.

As the discussed above, SMO forms a particular pattern near the base of cilia but its relative position to the TZ remains to be determined. Thus, we here use TCTN2 protein as a transition zone marker to study the localization of SMO. Figure 5-19A includes three sets of two-color STED images demonstrating the relative position of TCTN2 and SMO

for MEFs. As we have seen in the previous chapter, TCTN2 comes as two separate dots shown in the first column of Figure 5-19A. The corresponding SMO images are shown side-by-side to display the difference of localization between the two proteins. We found that SMO is localized to the TZ as it is mostly overlapped with TCTN2. To further investigate SMO localization, the lateral diameter and axial position for TCTN2 and SMO are analyzed and statistically reported in Figure 5-20. We found their average lateral diameters are nearly identical (Figure 5-20A) and the axial location (Figure 5-20B) of SMO spreads over the TZ but mostly in or above the TZ. This reveals SMO is transported via the membrane side of TZ segment since TCTN2 has been shown to localize close to ciliary membrane in Chapter 3. Therefore, the two branches or two dots of SMO pattern is the portion co-localized with TCTN2. To differentiate the transport mechanism of SMO and IFT proteins, IFT88 and TCTN2 are immunostained in MEFs to depict the situation relative to TCTN2 (Figure 5-19B). It turns out to be that the distal punctum of IFT88 near TCTN2, however, is situated between the two dots of TCTN2, i.e. bound in the center (see the arrows in Figure 5-19).

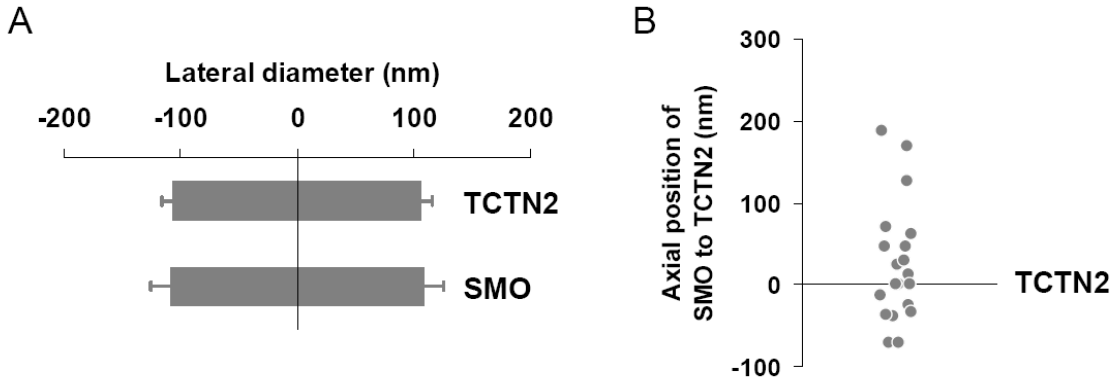

Figure 5-20 Statistical analyses of lateral diameter and axial position of SMO proteins with respect to TCTN2. (A) Two proteins are similarly in diameter. (B) Vertical position of SMO ranges through the TZ.

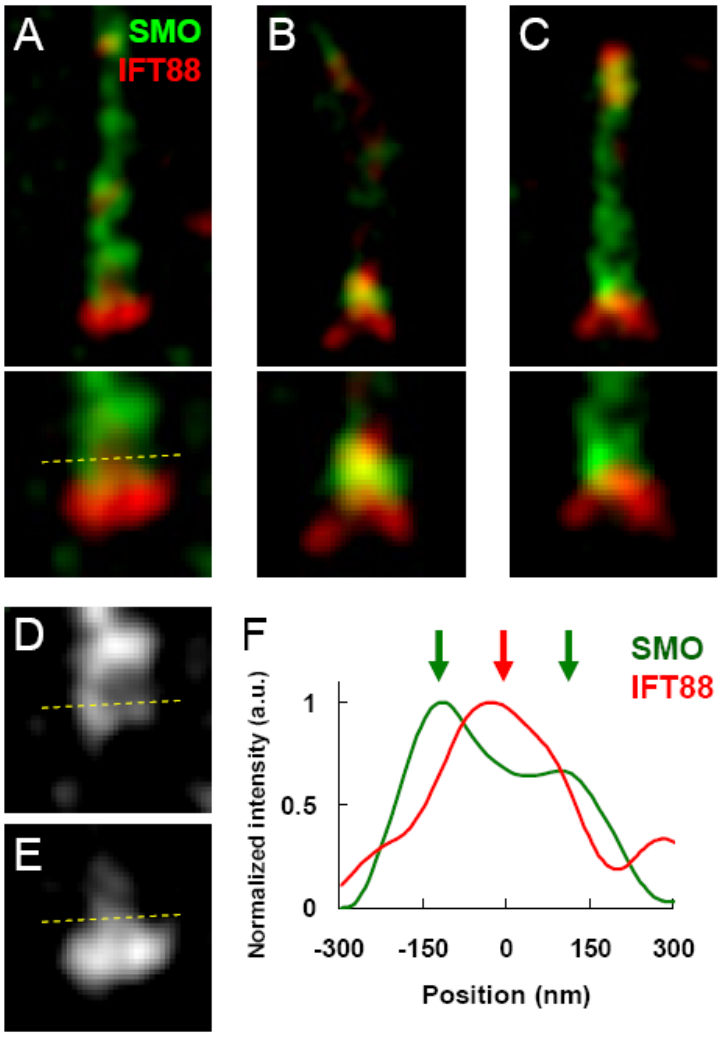

Figure 5-21 Two-color imaging of SMO and IFT88 at primary cilia of MEFs shown in upper panels of (A-C). Lower panels highlight the corresponding ciliary base. (D and E) The single-color images of A. (F) Intensity profiles along the dash line for SMO and IFT88. Two resolvable intensity peaks are marked with green arrows but IFT88 only forms a single peak (red arrow) under our STED resolution, implying that SMO transport is along the outer part of the TZ while IFT88 is toward the axoneme.

To validate the distinct localization of SMO and IFT88 near the TZ, we stained primary cilia with the antibodies against those two proteins in MEFs. The results are shown in Figure 5-21 which includes three examples of IFT88/SMO merged images.

Different from the images in Figure 5-19A where SMO is mostly localized near TCTN2 at the TZ, SMO here is higher than the proximal puncta of IFT88 but is at the same level of the distal punctum. Moreover, SMO is laterally situated wider than IFT88 at the TZ. Figure 5-21F shows intensity profiles extracted from single-color images in Figure 5-21D and E along the dash lines. The difference of localization is readily recognized with the arrows indicating the intensity peaks.

Based on our dual-color STED results of SMO, IFT88, and one TZ component, TCTN2, we propose a localization model for SMO and IFT proteins. Figure 5-22A depicts the possible localization of them; the IFT88 as reported in Chapter 4 is localized to the TFs through the TZ up to the distal site. TCTN2 showing as two dots is found on the skirt of the TZ with our subdiffraction imaging. Figure 5-19B has displayed the unlike organization of TCTN2 and IFT88 where IFT88 transport may occurs along the axoneme while TCTN2 is bound at the membrane. Our finding here further supports this proposed localization pattern where SMO is distributed as wide as TCTN2. SMO can be found from the lower to upper part of the TZ gradually shrinking in lateral width. Therefore, we further propose the potential transport mechanism of SMO. As shown in Figure 5-22B, SMO is translocated to primary cilia via the ciliary membrane and most of them accumulate at the TZ; however, IFT88 trafficking occurs from the docking site at the TFs into the TZ along the axoneme up to cilium compartment. Assembly of IFT88, SMO, and motors may take place in or above the TZ where accumulation of SMO and IFT88 is found and thus the motor-driven transport is activated. Therefore, before this action, SMO and IFT88 are likely to move in different pathways as proposed in Figure 5-22B, evidenced based on the STED results. The assembly of IFT88 and the associated motors

may also happen prior to the interaction with SMO above the TZ.

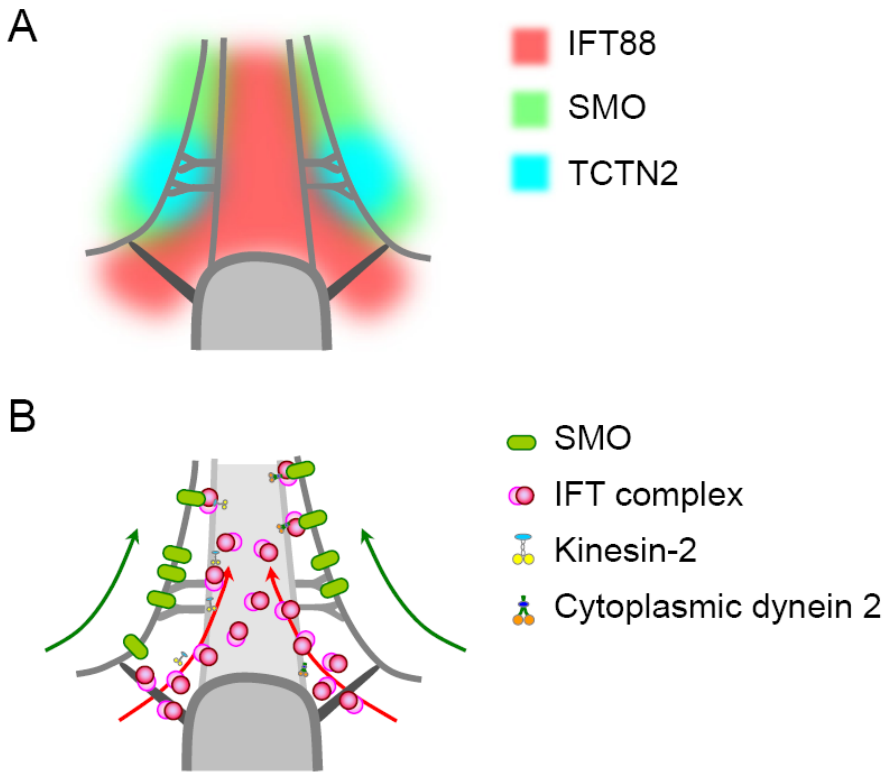

Figure 5-22 Possible transport mechanism of SMO and IFT88. (A) The localization model of the described proteins. SMO lies to the membrane as wide as TCTN2 while IFT88 is toward the microtubules. (B Transport model of SMO and IFT88 implies the different pathways to guide them into the cilium through the TZ. They may be assembled at the distal part of the TZ or right above the region.

5.5 Materials and methods

5.5.1 Cell culture and transfection

Human RPE-1 cells were grown on #1.5 cover glasses coated with poly-l-lysine, in DMEM/F12 supplemented with 10% FBS, 12mM HEPES, 2.5mM L-glutamine, 2.4g/L

sodium bicarbonate, and 1% penicillin/streptomycin at 37°C and 5% CO_2 up to 60%~90% confluence depending on the experimental conditions, and then incubated in serum-deprived media for 48 hours. For lithium stimulation experiment, cells were treated with 100mM lithium chloride (L121-100, Fisherbrand) for one hour before fixation.

For live-cell imaging, the mouse inner medullary collecting duct (IMCD, IFT88-eYFP) cell line[100] and MEF cell line were used to image the IFT movement. Mouse IMCD cells were infected by vesicular stomatitis virus-G–pseudotyped murine Moloney leukemia retrovirus constructed from a modified pBABE vector44 with a blasticidin resistance cassette and harboring a C-terminal–tagged IFT88-EYFP fusion cDNA. After infection, colonies were isolated after selection in 2 mg/ml of blasticidin and expanded to create monoclonal cell lines.

IMCD cells were cultured on a glass-bottom dish in DMEM with 10% FBS, 15mM HEPES, 1 mM Pen-strep at 37°C and 5% CO2 up to ~50%-60% confluence, and then incubated with 0.1% FBS for 24-48 hours. Fibronectin (10 μg/ml, Sigma-Aldrich) was used to coat the surface so cells can adhere better to the substrate. MEFs were cultured on a glass-bottom dish in DMEM with 10% FBS, 1.5% HEPES, 1.2% Pen-strep at 37°C and 5% CO2 up to ~60%-80% confluence, and then transfected with Lipofectamine 2000 (Invitrogen). The ratio of plasmid (μg) to liposome (μl) was used at 1/3 ~ 1/5 for best results. During the transfection, Cells were incubated in OptiMEM without the antibiotics for 6-18 hours, followed by a serum-deprived culture for 24 to 48 hours.

For SMO imaging, MEFs are cultured as IMCD cells in DMEM. To induce translocation of SMO to primary cilia, cells are first serum-deprived at 0.1% FBS for 24

hours and then incubated in the same media with 2 μM SAG (Smoothened ligand, ALX-270-426, Enzo) for 2 to 24 hours.

5.5.2 Immunofluorescence

For indirect immunofluorescence, cells were fixed in methanol at -20°C for at least 10 minutes. Following fixation, cells were washed 2-3 times in 0.1% PBST (PBS + Triton X-100), and then blocked with 1% normal goat serum and 2.5% BSA in 0.1% PBST for 30 min at room temperature. Primary antibodies used for section 5.2 and 5.3 are rabbit anti-IFT88 antibody (13967-1-AP, Proteintech at 1/200). For section 5.4, mouse anti-IFT88 antibody (60227-1-Ig, Proteintech at 1/100) was used to allow two-color labeling with SMO which is stained with the rabbit antibody (anti-Smoothened antibody, ab38686, Abcam). Cells were stained with primary antibodies in block solution for 1 hour at room temperature, and rinsed at least 3 times in PBST. Cover glasses were then incubated with secondary antibodies (Oregon Green 488 goat anti rabbit or mouse, Alexa Flour 647 goat anti rabbit) or biotin antibodies for 45-60 min at room temperature, and rinsed again 3-5 times in PBST. For two-color samples, the cells were stained with streptavidin conjugated to V500 dye (BD Horizon) for 20~30 min, and then the samples were mounted with 86% glycerol in PBS.

5.5.3 Live-cell imaging

For live-cell epifluorescent imaging, time-lapse images were acquired using a 100X oil objective (UPLSAPO100x-1.4 NA, Olympus) in an Olympus IX81 microscope, and images were captured using Metaphor software by a charge-coupled device camera (C8484 camera, Hamamatsu). Before being placed on the microscope, cells on

glass-bottom dishes were washed in warm PBS, and then immersed in DMEM/F12 (phenol red free; 0.1% FBS, 15mM HEPES, 1 mM penicillin and streptomycin). Images were taken at 1 to 1.5s intervals with exposure time of 200-250 ms. To enhance the signal-to-noise level, some images were captured with 2 by 2 binning process.

For subdiffraction-resolution imaging with our STED system, the same 100X objective was used to capture time-lapse images. In order to reach a sufficient acquisition speed and a tolerant signal-to-noise ratio, we compromised to a scanning area of 10 μm by 2.5-3.5 μm to image only the base of primary cilia. A wider horizontal dimension of 10μm was chosen to avoid the imaging distortion at the edge of frame caused by the accelerated scanning method. Images were recorded by scanning the sample stage with a pixel size of 40-50 nm and dwell time of 20 μs.

5.5.4 Data Analysis

To determine the velocities of IFT88-EYFP particles, image sequences were analyzed and assembled into kymographs using the ImageJ software package. The principle of kymograph analysis is illustrated in Figure 5-23[112]. To characterize the speed in the cilium, a path line was drawn along the axis of a primary cilium; for the IFT speed in the TZ, we defined a path line for kymograph according to the IFT88 pattern in which this line passed through one of proximal punctum and a distal punctum, and then was aligned with the cilium. Individual STED images were deconvoluted and normalized to compensate for the intensity decrease by photobleaching.

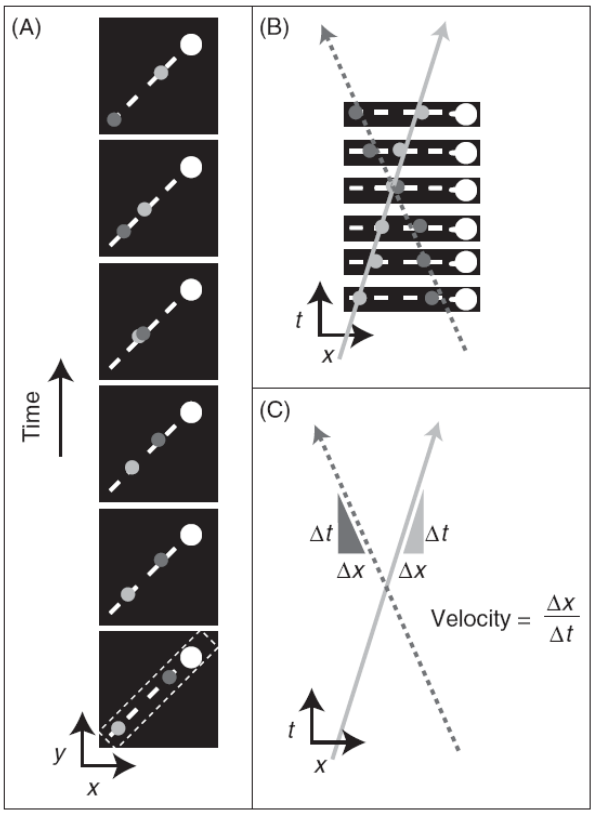

Figure 5-23 Schematic illustration of kymograph based analysis of IFT velocities. (A) The sequential frames of particles moving along the cilium were converted into a time series. (B) The kymograph, a time-space image, is generated from gray values along the line of each frame. (C) The slopes of these lines correspond to velocities of moving particles[112].

6 Summary

We have studied the ciliary structure and the transport mechanism of IFT proteins and important signaling receptors near the transition zone. This project benefited greatly from development of a superresolution STED microscopy system, especially with dual-color imaging capability, thus enabling the exploration of molecular localization/co-localization for primary cilia. To achieve these aims towards the understanding of ciliary framework and function, we have implemented a home-built dual-color STED system designed for a broad spectrum of fluorescent dyes with flexibly imaging configuration compatible to the various courses of ciliary studies. Throughout this project, all biological protocols of each individual step before the imaging have also been established and optimized for the purpose of superresolution imaging.

Chapter 2 shows the details of implementation of the dual-color common-depletion STED microscopy system extended from a single-color CW STED setup, enabling spectrum-separable excitation of the fluorophore pair of Oregon Green 488 and V500 dye. We have optimized the optical alignment to allow three laser beams to spatially coincide with each others and hence maximal depletion efficiency and signal-to-noise ratio are achieved. With these fluorophores, we have shown the system PSFs of diffraction-unlimited spot is 50-60 nm in FWHM which yields a ~16-fold improvement of sensing area as compared with the confocal resolution of 200-230 nm. We have also examined imaging performance while resolving the individual actin bundles. Furthermore, color separation of this system is validated for biologically featured-defined samples with the use of appropriate detection windows. Therefore, we have successfully developed this dual-color superresolution system for both physical and biological samples.

In chapter 3, we have reported the distinct localization of two important ciliary proteins, IFT88 and ACIII using the CW STED microscope. Our finding shows that ACIII localizes along primary cilia as a punctate fashion with nearly equal spacing, which comes as a continuous pattern in conventional microscopes. This may benefit the morphological understanding of cAMP signaling site over primary cilia. The quantitative analyses of molecular distribution of ACIII shows an average spacing of about 200-300 nm in axial length, revealing a natural distance of distribution as ACIII is present at cilia for signaling function. Intriguingly, we have found the important and previously unreported localization of IFT88 protein at the base of cilia. Two differentiable patterns of three puncta and Y shape are demonstrated here from many cell types including human fibroblasts, mouse IMCD, and MEFs. Statistical analyses of geometrical configuration for the two patterns show the conservation of structure at the ciliary base.

In Chapter 4, we have mainly focused on the study of molecular architecture at the transition zone using the dual-color STED imaging approach. To facilitate this project, we have optimized all required experimental parameters, including sample preparations and imaging protocols, such as laser power, optical alignment, and staining protocol. Thus, we have analyzed the structural arrangement at the TZ by means of a series of two-color superresolution images to reconstruct their relative orientation among the TZ/TF proteins and the basal body component. Subdiffraction imaging of these components defines unreported geometric distributions of CEP290, RPGRIP1L, MKS1, TMEM67, TCTN2, CEP164, and Centrin. To gain insight into the full story of their functionality, we have mapped these seven-color superresolution images to electron microscopy images. We found that RPGRIP1L, MKS1, TMEM67, and TCTN2 are

situated at the similar level of the TZ; however, CEP290 alone is below other TZ proteins by ~100 nm. In terms of lateral distribution, the first four proteins present at different distances from the axoneme of cilia, indicating the order of RPGRIP1L, MKS1, TMEM67, and TCTN2 from the inmost to the farthest on the membrane. CEP290 is confined at the ciliary axoneme.

Chapter 5 exhibits three different angles toward the exploration of trafficking mechanism of IFT particles and signaling receptors at the ciliary base. We have first studied the influence of ciliary growth on IFT mechanism by changing degree of cell contact or by promoting ciliary elongation with lithium treatment. We then proposed a transport model based on our finding that transformation of IFT88 patterns among three puncta, Y shape, and two puncta relies on a given growth condition. A growing cilium requires higher level of IFT occurrence, so the Y-shaped configuration is dominant. Upon the architecture mapping of TZ described in Chapter 4, we have been able to correlate the observed localization of IFT protein with the framework of TZ. This underlines that IFT88 mostly accumulates at TFs as the lower docking site and piles up at the distal end of TZ as the upper docking site. These two spots are structurally the entrances of TZ where the IFT particle is probably directed through a gating path. Second, we directly investigated this mechanism by means of the superresolution live-cell imaging of IFT88. The optimized imaging protocols have allowed us to observe how IFT particles pass through the TZ. Surprisingly, IFT protein slows down at the TZ at about half of the speed at the cilium. This supports the gating mechanism of TZ as a diffusion barrier to hinder crossing this region. Last, we have shown the transport pathway of SMO translocation to cilia which is different from the IFT pathway. Our superresolution results have displayed

that SMO moves via the skirt of the TZ but IFT88 travels near ciliary axoneme. Different from IFT88, SMO accumulates at the TZ and is colocalized with TCTN2 toward the membrane, but no significant level of SMO is found at the TFs.

Bibliography

1 Besharse, J. C. & Horst, C. J. in *Ciliary and flagellar membranes* 389-417 (Springer, 1990).

2 Ezratty, E. J. *et al.* A role for the primary cilium in Notch signaling and epidermal differentiation during skin development. *Cell* **145**, 1129-1141 (2011).

3 Huangfu, D. & Anderson, K. V. Cilia and Hedgehog responsiveness in the mouse. *Proceedings of the National Academy of Sciences of the United States of America* **102**, 11325-11330 (2005).

4 Malone, A. M. *et al.* Primary cilia mediate mechanosensing in bone cells by a calcium-independent mechanism. *Proceedings of the National Academy of Sciences* **104**, 13325-13330 (2007).

5 Nakamura, T. & Gold, G. H. A cyclic nucleotide-gated conductance in olfactory receptor cilia. (1987).

6 Schneider, L. *et al.* PDGFRαα signaling is regulated through the primary cilium in fibroblasts. *Current Biology* **15**, 1861-1866 (2005).

7 Simons, M. *et al.* Inversin, the gene product mutated in nephronophthisis type II, functions as a molecular switch between Wnt signaling pathways. *Nature Genetics* **37**, 537-543 (2005).

8 WHEATLEY, D. N., WANG, A. M. & STRUGNELL, G. E. Expression of primary cilia in mammalian cells. *Cell Biology International* **20**, 73-81 (1996).

9 Feistel, K. & Blum, M. Three types of cilia including a novel 9+ 4 axoneme on the notochordal plate of the rabbit embryo. *Developmental Dynamics* **235**, 3348-3358 (2006).

10 Singla, V. & Reiter, J. F. The primary cilium as the cell's antenna: signaling at a sensory organelle. *Science Signaling* **313**, 629 (2006).

11 Afzelius, B. Cilia-related diseases. *The Journal of pathology* **204**, 470-477 (2004).

12 Ishikawa, H. & Marshall, W. F. Ciliogenesis: building the cell's antenna. *Nature Reviews Molecular Cell Biology* **12**, 222-234 (2011).

13 Kramer-Zucker, A. G. *et al.* Cilia-driven fluid flow in the zebrafish pronephros, brain and Kupffer's vesicle is required for normal organogenesis. *Development* **132**, 1907-1921 (2005).

14 Anderson, R. G. The three-dimensional structure of the basal body from the rhesus monkey oviduct. *The Journal of cell biology* **54**, 246-265 (1972).

15 Reiter, J. F., Blacque, O. E. & Leroux, M. R. The base of the cilium: roles for transition fibres and the transition zone in ciliary formation, maintenance and

compartmentalization. *EMBO reports* **13**, 608-618 (2012).

16 Craige, B. *et al.* CEP290 tethers flagellar transition zone microtubules to the membrane and regulates flagellar protein content. *The Journal of cell biology* **190**, 927-940 (2010).

17 Garcia-Gonzalo, F. R. *et al.* A transition zone complex regulates mammalian ciliogenesis and ciliary membrane composition. *Nature Genetics* **43**, 776-784 (2011).

18 Williams, C. L. *et al.* MKS and NPHP modules cooperate to establish basal body/transition zone membrane associations and ciliary gate function during ciliogenesis. *The Journal of cell biology* **192**, 1023-1041 (2011).

19 Chih, B. *et al.* A ciliopathy complex at the transition zone protects the cilia as a privileged membrane domain. *Nature cell biology* **14**, 61-72 (2011).

20 Hu, Q. *et al.* A septin diffusion barrier at the base of the primary cilium maintains ciliary membrane protein distribution. *Science Signaling* **329**, 436 (2010).

21 Sang, L. *et al.* Mapping the NPHP-JBTS-MKS protein network reveals ciliopathy disease genes and pathways. *Cell* **145**, 513-528 (2011).

22 Garcia-Gonzalo, F. R. & Reiter, J. F. Scoring a backstage pass: mechanisms of ciliogenesis and ciliary access. *The Journal of cell biology* **197**, 697-709 (2012).

23 Otto, E. A. *et al.* Mutations in INVS encoding inversin cause nephronophthisis type 2, linking renal cystic disease to the function of primary cilia and left-right axis determination. *Nature Genetics* **34**, 413-420 (2003).

24 Sayer, J. A. *et al.* The centrosomal protein nephrocystin-6 is mutated in Joubert syndrome and activates transcription factor ATF4. *Nature Genetics* **38**, 674-681 (2006).

25 Kyttälä, M. *et al.* MKS1, encoding a component of the flagellar apparatus basal body proteome, is mutated in Meckel syndrome. *Nature Genetics* **38**, 155-157 (2006).

26 Szymanska, K. & Johnson, C. A. The transition zone: an essential functional compartment of cilia. *Cilia* **1**, 1-9 (2012).

27 Huang, L. *et al.* < i> TMEM237</i> Is Mutated in Individuals with a Joubert Syndrome Related Disorder and Expands the Role of the TMEM Family at the Ciliary Transition Zone. *The American Journal of Human Genetics* **89**, 713-730 (2011).

28 Kozminski, K. G., Johnson, K. A., Forscher, P. & Rosenbaum, J. L. A motility in the eukaryotic flagellum unrelated to flagellar beating. *Proceedings of the National Academy of Sciences* **90**, 5519-5523 (1993).

29 Rosenbaum, J. L. & Witman, G. B. Intraflagellar transport. *Nature Reviews*

Molecular Cell Biology **3**, 813-825 (2002).

30 Deane, J. A., Cole, D. G., Seeley, E. S., Diener, D. R. & Rosenbaum, J. L. Localization of intraflagellar transport protein IFT52 identifies basal body transitional fibers as the docking site for IFT particles. *Current Biology* **11**, 1586-1590 (2001).

31 Cole, D. G. *et al.* Chlamydomonas kinesin-II–dependent intraflagellar transport (IFT): IFT particles contain proteins required for ciliary assembly in Caenorhabditis elegans sensory neurons. *The Journal of Cell Biology* **141**, 993-1008 (1998).

32 Pedersen, L. B. & Rosenbaum, J. L. Chapter two intraflagellar transport (IFT): role in ciliary assembly, resorption and signalling. *Current Topics in Developmental Biology* **85**, 23-61 (2008).

33 Piperno, G. & Mead, K. Transport of a novel complex in the cytoplasmic matrix of Chlamydomonas flagella. *Proceedings of the National Academy of Sciences* **94**, 4457-4462 (1997).

34 Absalon, S. *et al.* Intraflagellar transport and functional analysis of genes required for flagellum formation in trypanosomes. *Molecular Biology of the Cell* **19**, 929-944 (2008).

35 Brown, J. M., Fine, N. A., Pandiyan, G., Thazhath, R. & Gaertig, J. Hypoxia regulates assembly of cilia in suppressors of Tetrahymena lacking an intraflagellar transport subunit gene. *Molecular Biology of the Cell* **14**, 3192-3207 (2003).

36 Follit, J. A., Tuft, R. A., Fogarty, K. E. & Pazour, G. J. The intraflagellar transport protein IFT20 is associated with the Golgi complex and is required for cilia assembly. *Molecular Biology of the Cell* **17**, 3781-3792 (2006).

37 Pazour, G. J. *et al.* Chlamydomonas IFT88 and its mouse homologue, polycystic kidney disease gene tg737, are required for assembly of cilia and flagella. *The Journal of Cell Biology* **151**, 709-718 (2000).

38 Haycraft, C. J., Swoboda, P., Taulman, P. D., Thomas, J. H. & Yoder, B. K. The C. elegans homolog of the murine cystic kidney disease gene Tg737 functions in a ciliogenic pathway and is disrupted in osm-5 mutant worms. *Development* **128**, 1493-1505 (2001).

39 Yoder, B. K. *et al.* Polaris, a protein disrupted in orpk mutant mice, is required for assembly of renal cilium. *American Journal of Physiology-Renal Physiology* **282**, F541-F552 (2002).

40 Pazour, G. J. *et al.* The intraflagellar transport protein, IFT88, is essential for vertebrate photoreceptor assembly and maintenance. *The Journal of Cell Biology* **157**, 103-114 (2002).

41 Robert, A. *et al.* The intraflagellar transport component IFT88/polaris is a

centrosomal protein regulating G1-S transition in non-ciliated cells. *Journal of Cell Science* **120**, 628-637 (2007).

42 Nauli, S. M. *et al.* Polycystins 1 and 2 mediate mechanosensation in the primary cilium of kidney cells. *Nature Genetics* **33**, 129-137 (2003).

43 Bisgrove, B. W. & Yost, H. J. The roles of cilia in developmental disorders and disease. *Development* **133**, 4131-4143 (2006).

44 Boletta, A. & Germino, G. G. Role of polycystins in renal tubulogenesis. *Trends in Cell Biology* **13**, 484-492 (2003).

45 Praetorius, H. & Spring, K. R. Bending the MDCK cell primary cilium increases intracellular calcium. *The Journal of membrane biology* **184**, 71-79 (2001).

46 Huangfu, D. & Anderson, K. V. Signaling from Smo to Ci/Gli: conservation and divergence of Hedgehog pathways from Drosophila to vertebrates. *Development* **133**, 3-14 (2006).

47 Haycraft, C. J. *et al.* Gli2 and Gli3 localize to cilia and require the intraflagellar transport protein polaris for processing and function. *PLoS genetics* **1**, e53 (2005).

48 Huangfu, D. *et al.* Hedgehog signalling in the mouse requires intraflagellar transport proteins. *Nature* **426**, 83-87 (2003).

49 Liu, A., Wang, B. & Niswander, L. A. Mouse intraflagellar transport proteins regulate both the activator and repressor functions of Gli transcription factors. *Development* **132**, 3103-3111 (2005).

50 May, S. R. *et al.* Loss of the retrograde motor for IFT disrupts localization of Smo to cilia and prevents the expression of both activator and repressor functions of Gli. *Developmental Biology* **287**, 378-389 (2005).

51 Corbit, K. C. *et al.* Vertebrate Smoothened functions at the primary cilium. *Nature* **437**, 1018-1021 (2005).

52 Alberts, B. *et al. Essential cell biology*. 2nd edn, (New York: Garland Science, 2004).

53 Bishop, G. A., Berbari, N. F., Lewis, J. & Mykytyn, K. Type III adenylyl cyclase localizes to primary cilia throughout the adult mouse brain. *The Journal of Comparative Neurology* **505**, 562-571 (2007).

54 Berbari, N. F., Bishop, G. A., Askwith, C. C., Lewis, J. S. & Mykytyn, K. Hippocampal neurons possess primary cilia in culture. *Journal of Neuroscience Research* **85**, 1095-1100 (2007).

55 Defer, N., Best-Belpomme, M. & Hanoune, J. Tissue specificity and physiological relevance of various isoforms of adenylyl cyclase. *American Journal of Physiology-Renal Physiology* **279**, F400-F416 (2000).

56 Bakalyar, H. A. & Reed, R. R. Identification of a specialized adenylyl cyclase that may mediate odorant detection. *Science* **250**, 1403-1406 (1990).

57 Wong, S. T. *et al.* Disruption of the type III adenylyl cyclase gene leads to peripheral and behavioral anosmia in transgenic mice. *Neuron* **27**, 487-497 (2000).

58 Wang, Z., Phan, T. & Storm, D. R. The type 3 adenylyl cyclase is required for novel object learning and extinction of contextual memory: role of cAMP signaling in primary cilia. *The Journal of Neuroscience* **31**, 5557-5561 (2011).

59 Ou, Y. *et al.* Adenylate cyclase regulates elongation of mammalian primary cilia. *Experimental Cell Research* **315**, 2802-2817 (2009).

60 Miyoshi, K., Kasahara, K., Miyazaki, I. & Asanuma, M. Factors that influence primary cilium length. *Acta Medica Okayama* **65**, 279-285 (2011).

61 Miyoshi, K., Kasahara, K., Miyazaki, I. & Asanuma, M. Lithium treatment elongates primary cilia in the mouse brain and in cultured cells. *Biochemical and Biophysical Research Communications* **388**, 757-762 (2009).

62 Abbe, E. Beiträge zur Theorie des Mikroskops und der mikroskopischen Wahrnehmung. *Archiv für mikroskopische Anatomie* **9**, 413-418 (1873).

63 Sedmak, T. & Wolfrum, U. Intraflagellar transport molecules in ciliary and nonciliary cells of the retina. *The Journal of cell biology* **189**, 171-186 (2010).

64 Abrahams, J. P., Leslie, A. G., Lutter, R. & WalkerT, J. E. Structure at 2.8 A resolution of F1-ATPase. *Nature* **370**, 25 (1994).

65 Lemmer, P. *et al.* SPDM: light microscopy with single-molecule resolution at the nanoscale. *Applied Physics B* **93**, 1-12 (2008).

66 Huang, B., Wang, W., Bates, M. & Zhuang, X. Three-dimensional super-resolution imaging by stochastic optical reconstruction microscopy. *Science* **319**, 810-813 (2008).

67 Gustafsson, M. G. Nonlinear structured-illumination microscopy: wide-field fluorescence imaging with theoretically unlimited resolution. *Proceedings of the National Academy of Sciences of the United States of America* **102**, 13081-13086 (2005).

68 Hell, S. W. & Wichmann, J. Breaking the diffraction resolution limit by stimulated emission: stimulated-emission-depletion fluorescence microscopy. *Optics letters* **19**, 780-782 (1994).

69 Klar, T. A., Jakobs, S., Dyba, M., Egner, A. & Hell, S. W. Fluorescence microscopy with diffraction resolution barrier broken by stimulated emission. *Proceedings of the National Academy of Sciences* **97**, 8206-8210 (2000).

70 Rust, M. J., Bates, M. & Zhuang, X. Sub-diffraction-limit imaging by stochastic

optical reconstruction microscopy (STORM). *Nature Methods* **3**, 793-796 (2006).

71 Betzig, E. *et al.* Imaging intracellular fluorescent proteins at nanometer resolution. *Science* **313**, 1642-1645 (2006).

72 Manley, S. *et al.* High-density mapping of single-molecule trajectories with photoactivated localization microscopy. *Nature Methods* **5**, 155-157 (2008).

73 Willig, K. I., Harke, B., Medda, R. & Hell, S. W. STED microscopy with continuous wave beams. *Nature Methods* **4**, 915-918 (2007).

74 Hell, S. W. & Kroug, M. Ground-state-depletion fluorscence microscopy: A concept for breaking the diffraction resolution limit. *Applied Physics B* **60**, 495-497 (1995).

75 Hofmann, M., Eggeling, C., Jakobs, S. & Hell, S. W. Breaking the diffraction barrier in fluorescence microscopy at low light intensities by using reversibly photoswitchable proteins. *Proceedings of the National Academy of Sciences of the United States of America* **102**, 17565-17569 (2005).

76 Hess, S. T., Girirajan, T. P. & Mason, M. D. Ultra-high resolution imaging by fluorescence photoactivation localization microscopy. *Biophysical Journal* **91**, 4258-4272 (2006).

77 van de Linde, S. *et al.* Direct stochastic optical reconstruction microscopy with standard fluorescent probes. *Nature protocols* **6**, 991-1009 (2011).

78 Bornfleth, H., Saetzler, K., Eils, R. & Cremer, C. High-precision distance measurements and volume-conserving segmentation of objects near and below the resolution limit in three-dimensional confocal fluorescence microscopy. *Journal of Microscopy* **189**, 118-136 (1998).

79 Gunkel, M. *et al.* Dual color localization microscopy of cellular nanostructures. *Biotechnology journal* **4**, 927-938 (2009).

80 Sharonov, A. & Hochstrasser, R. M. Wide-field subdiffraction imaging by accumulated binding of diffusing probes. *Proceedings of the National Academy of Sciences* **103**, 18911-18916 (2006).

81 Hein, B., Willig, K. I. & Hell, S. W. Stimulated emission depletion (STED) nanoscopy of a fluorescent protein-labeled organelle inside a living cell. *Proceedings of the National Academy of Sciences* **105**, 14271-14276 (2008).

82 Urban, N. T., Willig, K. I., Hell, S. W. & Nägerl, U. V. STED nanoscopy of actin dynamics in synapses deep inside living brain slices. *Biophysical Journal* **101**, 1277-1284 (2011).

83 Westphal, V. *et al.* Video-rate far-field optical nanoscopy dissects synaptic vesicle movement. *Science* **320**, 246-249 (2008).

84 Lauterbach, M. A., Ullal, C. K., Westphal, V. & Hell, S. W. Dynamic imaging of

colloidal-crystal nanostructures at 200 frames per second. *Langmuir* **26**, 14400–14404 (2010).

85 Nathwani, B. B., Yang, T. T. & Liao, J.-C. Towards a Subdiffraction View of Motor-Mediated Transport in Primary Cilia. *Cellular and Molecular Bioengineering*, 1-16 (2013).

86 Klar, T. A. & Hell, S. W. Subdiffraction resolution in far-field fluorescence microscopy. *Optics letters* **24**, 954-956 (1999).

87 McCumber, D. Einstein relations connecting broadband emission and absorption spectra. *Physical Review* **136**, A954 (1964).

88 Farahani, J. N., Schibler, M. J. & Bentolila, L. A. Stimulated emission depletion (STED) microscopy: from theory to practice. *Microscopy: Science, Technology, Applications and Education* **2**, 1539 (2010).

89 Jaboski, A. Efficiency of anti-Stokes fluorescence in dyes. *Nature* **131**, 839-840 (1933).

90 Lauterbach, M. *Fast STED microscopy*, Göttingen, Univ., Diss., 2009, (2009).

91 Hell, S. W. Toward fluorescence nanoscopy. *Nature Biotechnology* **21**, 1347-1355 (2003).

92 Saleh, B. E. & Teich, M. C. *Fundamentals of photonics*. (Wiley-Interscience, 2007).

93 Westphal, V. & Hell, S. W. Nanoscale resolution in the focal plane of an optical microscope. *Physical review letters* **94**, 143903 (2005).

94 Rohatgi, R. & Scott, M. P. Patching the gaps in Hedgehog signalling. *Nature Cell Biology* **9**, 1005-1009 (2007).

95 Igarashi, P. & Somlo, S. Genetics and pathogenesis of polycystic kidney disease. *Journal of the American Society of Nephrology* **13**, 2384-2398 (2002).

96 Geng, L. *et al.* Polycystin-2 traffics to cilia independently of polycystin-1 by using an N-terminal RVxP motif. *Journal of Cell Science* **119**, 1383-1395 (2006).

97 Bautista-Harris, G., Klotz, C., Bordes, N. & Sandoz, D. An helicoidal structure surrounding the cilium axoneme: Visualization by the monoclonal antibody CC-248. *Biology of the Cell* **71**, 191-200 (1991).

98 Klotz, C., Bordes, N., Laine, M. C., Sandoz, D. & Bornens, M. A protein of 175,000 daltons associated with striated rootlets in ciliated epithelia, as revealed by a monoclonal antibody. *Cell motility and the cytoskeleton* **6**, 56-67 (1986).

99 Clement, C. A. *et al.* The primary cilium coordinates early cardiogenesis and hedgehog signaling in cardiomyocyte differentiation. *Journal of Cell Science* **122**, 3070-3082 (2009).

100 Tran, P. V. *et al.* THM1 negatively modulates mouse sonic hedgehog signal transduction and affects retrograde intraflagellar transport in cilia. *Nature Genetics* **40**, 403-410 (2008).

101 Besschetnova, T. Y. *et al.* Identification of signaling pathways regulating primary cilium length and flow-mediated adaptation. *Current Biology* **20**, 182-187 (2010).

102 Sillibourne, J. E. *et al.* Assessing the localization of centrosomal proteins by PALM/STORM nanoscopy. *Cytoskeleton* **68**, 619-627 (2011).

103 Tikhonov, A. N. & Arsenin, V. Y. Solutions of Ill-Posed Problems. (1977).

104 Lau, L., Lee, Y. L., Sahl, S. J., Stearns, T. & Moerner, W. STED microscopy with optimized labeling density reveals 9-fold arrangement of a centriole protein. *Biophysical Journal* **102**, 2926-2935 (2012).

105 Wang, W.-J., Soni, R. K., Uryu, K. & Tsou, M.-F. B. The conversion of centrioles to centrosomes: essential coupling of duplication with segregation. *The Journal of cell biology* **193**, 727-739 (2011).

106 Yang, T. T. *et al.* Superresolution STED microscopy reveals differential localization in primary cilia. *Cytoskeleton* **70**, 54-65 (2013).

107 Smith, U. M. *et al.* The transmembrane protein meckelin (MKS3) is mutated in Meckel-Gruber syndrome and the wpk rat. *Nature Genetics* **38**, 191-196 (2006).

108 Wang, W.-J. *et al.* CEP162 is an axoneme-recognition protein promoting ciliary transition zone assembly at the cilia base. *Nature cell biology* **15**, 591-601 (2013).

109 Tikhonov, A. & Arsenin, V. *Solutions of ill-posed problems*. (Winston & Sons, 1977).

110 Baker, S. A., Freeman, K., Luby-Phelps, K., Pazour, G. J. & Besharse, J. C. IFT20 links kinesin II with a mammalian intraflagellar transport complex that is conserved in motile flagella and sensory cilia. *Journal of Biological Chemistry* **278**, 34211-34218 (2003).

111 Chen, J. K., Taipale, J., Young, K. E., Maiti, T. & Beachy, P. A. Small molecule modulation of Smoothened activity. *Proceedings of the National Academy of Sciences* **99**, 14071-14076 (2002).

112 Besschetnova, T. Y., Roy, B. & Shah, J. V. Imaging intraflagellar transport in mammalian primary cilia. *Methods in Cell Biology* **93**, 331-346 (2009).